SAPIENZA
UNIVERSITÀ DI ROMA

An improved scattering routine for collimation tracking studies at LHC

Facoltà di Scienze Matematiche, Fisiche e Naturali

Corso di Laurea Magistrale in Fisica

Candidate

Claudia Tambasco
ID number 1218021

Thesis Advisor

Dr. Gianluca Cavoto

Co-Advisors

Dr. Stefano Redaelli
Dr. Maria Belen Salvachua Ferrando

Academic Year 2012/2013

An improved scattering routine for collimation tracking studies at LHC
Master thesis. Sapienza – University of Rome

This thesis has been typeset by LaTeX and the Sapthesis class.

Author's email: claudia.tambasco@gmail.com

Dedicato a tutta la mia famiglia, per l'amore che mi ha sempre dimostrato.

Acknowledgments

The first person that I want to express my gratitude is my supervisor at CERN Belen Salvachua, with patience and devotion she guided me through this difficult path. Never losing the smile, she has always helped me during the work, encouraged me and reassured me when difficult moments came. This work was possible also because I learned a lot from her. Furthermore, I warmly thank Belen, not only for her concrete contribution to this thesis work, but also for always having believe in me and in my capabilities.

A Special thanks to the leader of LHC Collimation project Stefano Redaelli that gave me the possibility to work on this thesis project. He opened me new perspectives and gave me the chance to be part of an important work group. His precious experience was crucial to carry out this work. Working side by side with him enriched strongly both my professional and human experience.

Thanks also to my home university supervisor Gianluca Cavoto, who accepted to follow me in this experience. He has been a constant and reliable reference point on which I could always count.

I wish to address a great thanks to the whole Collimation group and in particular to my colleagues that always helped me to solve any kind of problems: Daniele that was the first to explain to me the scattering routine code and he always helped me by answering my many questions, Luisella that was always a precious and friendly adviser, Roderik that concretely helped me in the last part of the work, Aurelien that helped me with his precious tricks on python scripts.
And now I want to remember my family and Italian friends.

Ringrazio tutta la mia famiglia: é grazie ai loro sacrifici che ho raggiunto questo importante obiettivo. Con infinito amore hanno sempre desiderato il meglio per me e lavorato sodo affinché potessi ottenerlo; per questo dedico a loro il mio lavoro di tesi, sperando di ripagarli, almeno in parte, per tutto quello che hanno sempre fatto per me. Vi voglio tantissimo bene.

Un ringraziamento speciale va a Vincenzo per essere stato accanto a me in ogni momento. Per avermi sostenuto nei momenti di difficoltá, e per avermi sempre spronata a dare il meglio. Per aver avuto sempre pronto un buon consiglio, per avermi regalato tanti momenti di felicitá cancellando le mie paure, e per aver sempre creduto in me e nel mio lavoro.

Ringrazio Romina perché lei c'é sempre e perché durante tutti questi anni ha sempre accettato e sopportato da buona amica le mie assenze a causa dello studio. Per tutti i bei momenti passati insieme fin dal liceo e per essere sempre pronta ad aiutarmi nel momento del bisogno. Ringrazio Maurilia e Manlio, buoni amici da tanto tempo.

Ringrazio Elena, preziosa compagna di avventure qui a Ginevra nonché fedele amica e consigliera.

Ringrazio tutti i miei amici d'infanzia con i quali ho condiviso e continuo a condividere bei momenti di spensieratezza.

Un caloroso ringraziamento va a tutti i mie colleghi dell'universitá con i quali ho affrontato difficili esami, periodi di studio intenso, interminabili tesine di laboratorio e chi piú ne ha piú ne metta. In ogni caso, la loro compagnia ha sempre reso tutto meno faticoso. Un caloroso grazie a Federica, Francesca, Elena, Ambra, Arianna, Maddalena, Matteo, Maddalena, Daniele, Andrea e Valentina.

Un sentito grazie a tutti gli amici che ho conosciuto a Ginevra, a Davidone e a Robertone che spero d' incontrare di nuovo al piú presto ed a Valentina.

Infine voglio dire grazie, perché no, anche a me stessa. Per tutta la volontá che ho avuto in questi anni di studio, per tutti gli sforzi che ho fatto per arrivare fin qui e per non essermi arresa mai.

Contents

List of Figures

List of Tables

Chapter 1

Introduction

The first particle accelerator was built in the 1920s to investigate the structure of the atomic nucleus. Since then, more and more energetic particle accelerators have been designed to investigate many other aspects of particle physics.
The Large Hadron Collider is the world's largest and highest energy particle accelerator ever built. It was commissioned by the European Organization for Nuclear Research (CERN) in collaboration with more than 10000 scientists and engineers from over 100 countries and hundreds of universities and laboratories. The construction of the LHC started in 1999. The LHC accelerates proton and ion beams up to 7 TeV and 574 TeV respectively. The protons circulated for the first time the entire ring of the LHC on 10th September 2008, with an energy less than 1 TeV. The two counterrotating beams collide in the experiment detectors installed in four points on the accelerator ring. The two beams are accelerated by the electric field of the Radiofrequency (RF) cavities shaped to resonate at specific frequencies, allowing radio waves to interact with the passing particles. To bend and focus the circulating beams superconducting magnets (SC) are located around the beam pipes. They work at very low temperature, between 1.8 K and 4.5 K, if for some reasons the temperature of the magnets increases the SC magnets can lose their superconducting state and quench. The heating of the SC magnets can be caused by the energy deposition induced by local beam losses. Beam losses of $4{\cdot}10^7$ protons at 7 TeV correspond to an energy deposition of 30 mJ cm^3. To prevent beam losses, which are dangerous for the machine components, an efficient collimation system is of crucial importance. The LHC is equipped with a multi-stage collimation system that provides beam cleaning and passive machine protection. The beam core particles perform a stable motion around the ring while the particles that populate the so-called "beam halo", at the tails of the beam, will be uncontrollably lost in the machine. A collimator consist of two fully movable parallel jaws installed along the beam pipe. The two jaws are positioned at a specific distance creating a gap within which the particles of the beam core can pass unperturbed. The halo particles are intercepted and cleaned by the collimator jaws material, reducing considerably the risk of uncontrolled beam losses.
At the LHC different types of beam cleaning are provided by the collimation system: in the insertion IR3, is installed the collimation system that provides the cleaning of the off-momentum particles, while in the insertion IR7 particles with too large trans-

verse oscillation amplitudes are intercepted by the collimators providing betatron cleaning. In addition to protect the machine by radiation damage, the beam cleaning minimize the background for the LHC experiments. The cleaning performance of the collimation system is expressed by the *cleaning efficiency*. This parameter expresses the fraction of particles that hit a primary collimator and are stopped in the cleaning insertion. A cleaning efficiency above 99.99% must be reached to optimize the LHC performance.
The present work aims to increase the prediction power of the collimation performance at 7 TeV energy. Collimation studies for the LHC are performed with SixTrack, a dedicated simulation tool that tracks a large numbers of particles for many turns around the ring. The SixTrack code includes a scattering routine to model proton interactions with the collimators jaws. During the thesis work the scattering routine has been updated taking into account recent experimental data. The implemented updates allow an improved modeling capability for the 7 TeV proton beam interactions and to extract a better estimation of the cleaning performance of the collimation system. The results will be provided as input for collimation studies at higher energy.
The first part of the thesis introduces some useful fundamental concepts to analyze the present work. In particular in Chapter 2 the basic principles of linear beam dynamics, focusing on transversal and longitudinal motion, are covered together with some collimation theory concepts. The third chapter provides a brief introduction to the LHC detailing its collimation system. The main parameter for SixTrack code setup and the reference plots for collimation studies are presented in Chapter 4. The physics model of the scattering routine is described in detail in Chapter 5, each cross section characterizing the interaction between the proton and the material nuclei of the collimator jaw is taken into account. For each process the basic theory is introduced, followed by the description of the updates implemented according to recent available data. In order to asses the improvement with respect to the previous scattering routine version a comparison with the data is carried out. The last chapter is dedicated to the 7 TeV cleaning performance study with the new SixTrack version. In particular beam losses in the most critical machine region, the dispersion suppressor region are presented with the complete loss distribution around the ring. A parametric study of the effects on the collimation cleaning caused by the uncertainty of the proton-proton single diffractive cross section is also reported. This study can be a useful reference for future collimation studies at higher energy.

Chapter 2

Collimation theory for circular accelerators

The beams of a circular accelerator can be represented as bunches of particles for which the distribution inside each bunch can be considered as a Gaussian. The centre of the Gaussian distribution represents the particles that are the core of the bunch and perform stable oscillations along the designed orbit. Several processes can kick these particles and deviate them from the nominal orbit of the accelerator, populating thus the *primary halo* represented by the tails of the Gaussian. The halo particles perform unstable motion and can be lost at the aperture of the machine with the consequent release of energy that can damage the superconducting magnets. In order to avoid large energy depositions in the cold magnets an efficient collimation system in needed. The collimators intercept the particles that populate the tails of the particle distribution providing halo cleaning and protecting the machine.

2.1 Basic concepts of linear beam dynamics

The motion of particles inside the ring is driven by electric and magnetic fields. The electric field accelerates the particles and compensates the energy lost by synchrotron radiation. This field is generated by the *Radiofrequency cavities* (RF) that are resonant cavities with an applied sinusoidal potential difference synchronized with the particles of nominal momentum. The RF provide the energy for accelerating the particles and defines a spatial region called RF *bucket* that contains the particles synchronous with the RF. The particles outside the bucket will be loosing energy turn by turn until they are lost ideally at the collimators. The beam particles move inside the buckets grouped in bunches. The magnetic fields of several orders, dipole, quadrupoles, sextuples, octupoles and so on, define the motion of the particles through the machine. In particular, the dipole magnets determine a close orbit by bending the charged particles. Ideally, a particle with nominal energy can move infinitely along the closed orbit of the machine. However, in a non-ideal world, the particle is diverging from the nominal orbit and needs a focus strength to keep the nominal orbit. The quadrupoles focus the beam acting as an optical lens. The effect of the electric and the magnetic field on a charged particle is described by the

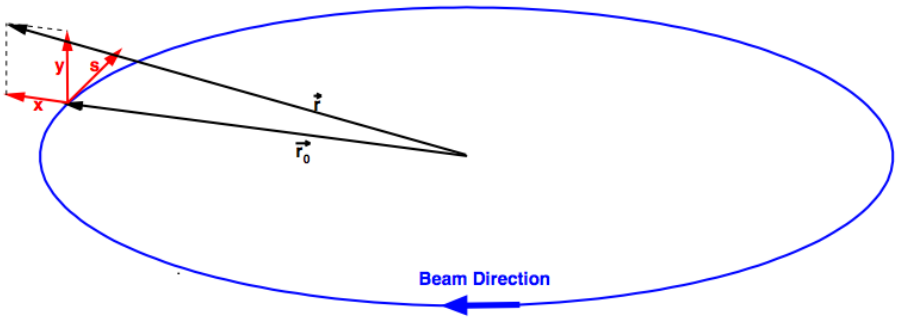

Figure 2.1. Coordinate system respect to the beam direction [1].

Lorentz force:

$$\frac{d\vec{p}}{dt} = q(\vec{E} + \vec{v} \wedge \vec{B}), \tag{2.1}$$

where $\vec{p}$ is the relativistic momentum of the particle, $\vec{v}$ is the velocity, q the charge and $\vec{E}$ and $\vec{B}$ the electric and the magnetic fields respectively. On the one hand this formula illustrates how a magnetic field will generate a change of momentum perpendicular to the velocity of the particle, thus being able to act in the trajectory of the particle and bend it. On the other hand an electric field will provide a change of momentum in the same direction of the field which could be used to accelerate or decelerate particles. In the following sections the longitudinal and the transverse motion of the particles along the ring will be described in more details.

2.1.1 Transverse motion and betatron oscillations

In this section we describe the transverse motion of a particle in an accelerator ring considering the steady state of the machine, that is not during the phase of injection, acceleration or extraction of the beams [1, 2, 3]. The reference system is represented in Fig.2.1, it is a right-handed orthogonal and moving system (x, y, s) and it takes the name of Frenet-Serret. The charged particle moves on the circular blue line, that represents the ideal closed orbit where $\vec{r_0}$ is the orbital radius. The vectors $\vec{s}$, $\vec{x}$ and $\vec{y}$ are respectively the tangential, horizontal and vertical position of the particle relative to the orbit.
A charged particle of momentum p is guided by dipoles that force the particle to curve and to follow circular orbit. By equating the centrifugal force and the Lorentz force:

$$F = qvB = \frac{\gamma m v^2}{\rho}, \tag{2.2}$$

where B is a constant field perpendicular to the particle velocity, the local radius (ρ) is given by:

$$\rho = \frac{p}{qB} \tag{2.3}$$

The *magnetic rigidity* R is defined as:

$$R = B\rho = \frac{p}{q}. \tag{2.4}$$

and it directly relates the effect of the magnetic field on the motion of charged particles.
The equation of motion can be derived using a linear approximation by considering that there is no longitudinal homogeneous component of the magnetic field, i.e $\vec{B} = (B_x, B_y, 0)$. The transverse components may be expanded in Taylor series to the first order [1] for small deviation from the designed orbit:

$$B_x(x, y, s) = B_{x0} + \frac{\partial B_x}{\partial x}x + \frac{\partial B_x}{\partial y}y \tag{2.5}$$

$$B_y(x, y, s) = B_{y0} + \frac{\partial B_y}{\partial x}x + \frac{\partial B_y}{\partial y}y. \tag{2.6}$$

From the Maxwell's equations we know the following relations:

$$\begin{aligned} \frac{\partial B_x}{\partial x} &= -\frac{\partial B_y}{\partial y}, \\ \frac{\partial B_y}{\partial x} &= \frac{\partial B_x}{\partial y}. \end{aligned} \tag{2.7}$$

We assume that the magnetic field is constant just on the vertical plane and zero in the horizontal plane, so the particle is bent on the horizontal plane. This means: $B_{x0} = 0$ and $\frac{\partial B_y}{\partial y} = 0$. By assuming no skew quadrupolar fields ($\frac{\partial B_x}{\partial x} = 0$) the Eq. 2.5 and Eq. 2.6 can be written:

$$B_x = \frac{\partial B_y}{\partial x}y = B_1 y, \tag{2.8}$$

$$B_y = -B_0 + \frac{\partial B_y}{\partial x}x = -B_0 + B_1 x, \tag{2.9}$$

where B_0 and B_1 are the coefficients of dipole and quadrupole respectively. Considering only particles of designed momentum and keeping only the linear terms, the so-called *Hill's equations* that describe the transverse motion are given [1]:

$$x'' + K_x(s)x = 0, \quad K_x(s) = \frac{1}{\rho(s)^2} - \frac{B_1(s)}{B\rho(s)} \tag{2.10}$$

$$y'' - K_y(s)y = 0, \quad K_y(s) = -\frac{B_1(s)}{B\rho(s)} \tag{2.11}$$

with $x' = dx/ds$ and $x'' = d^2x/ds^2$. Assuming the magnetic terms $\rho(s)$ and $K_y(s)$ are constant in s inside a magnetic element, the Eq. 2.10 and Eq. 2.11 give respectively the solutions of an harmonic oscillator or an exponential function, depending on the sign K_y. The solution of the *Hill's equations*, in the x direction is [2]:

$$x(s) = A\sqrt{\beta_x(s)}\sin(\varphi_x(s) + \varphi_0) \tag{2.12}$$

where $\beta_x(s)$ is the betatron function that is a periodic function and modulates the amplitude A of the *betatron oscillations* in the transversal plane, φ_0 is an constant phase. The solution for the y coordinate get the same form of Eq.2.12. The phase advance is $\varphi_x(s)$ and is given by:

$$\varphi(s) = \int_0^s \frac{ds'}{\beta(s')}. \tag{2.13}$$

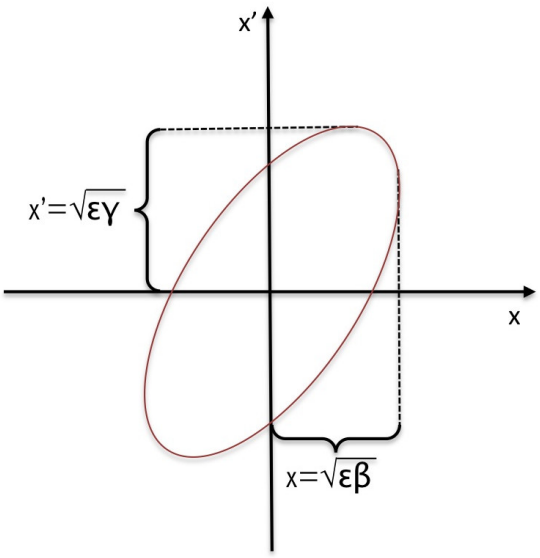

Figure 2.2. Particle trajectory in the phase space.

Each particle is characterized by different values of the constant A and its square root is known as single-particle emittance ϵ_x. The Eq. 2.12 can be rewritten as:

$$x(s) = \sqrt{\epsilon_x \beta_x(s)}\sin(\varphi_x(s) + \varphi_0). \tag{2.14}$$

Therefore, the motion in the transversal plane of the travelling particles around the accelerator ring is a sine-like trajectory with a varying amplitude $\epsilon_x\sqrt{\beta_x(s)}$ modulated by the betatron function and with a phase $\varphi_x(s) + \varphi_0$ that advances with s at vayring rate proportional to $1/\beta$. In the phase space (x, x'), the particle moves on an elliptical trajectory (Fig.2.2). The particle trajectory is described by the following equation [3]:

$$\epsilon_x = \gamma_x(s)x^2(s) + 2\alpha_x(s)x(s)x'(s) + \beta_x(s)x'^2(s) \tag{2.15}$$

where:

$$\alpha_x(s) = \frac{-\beta'_x(s)}{2} \tag{2.16}$$

$$\gamma_x(s) = \frac{1 + \alpha_x^2(s)}{\beta_x(s)} \tag{2.17}$$

$\alpha(s)$, $\beta(s)$ and $\gamma(s)$ are called *Twiss parameters* [3] and completely define the machine optics.
The shape of the ellipse depends on the s position in the machine, while the area does not change if the particles have a constant energy and stochastic effects are neglected during the motion. In the transversal phase space, all the particles of the beam can be represented by a Gaussian distribution of points with a σ_x called *betatronic beam size* and divergence $\sigma'_x(s)$:

$$\sigma_x = \sqrt{\epsilon_x^{\mathrm{rms}}\beta_x(s)} \tag{2.18}$$

$$\sigma'_x = \sqrt{\epsilon_x^{\text{rms}} \gamma_x(s)} \tag{2.19}$$

where ϵ_x^{rms} is the root mean square *emittance* and is defined as:

$$\epsilon_x^{\text{rms}} = \sqrt{< x^2 >< x'^2 > - < xx' >^2}. \tag{2.20}$$

The beam core is defined as the group of particles within 3σ(s) from the centre of the beam, while the tail or beam halo are all the particles outside that range. It is possible to define a normalized ϵ_x emittance, that does not vary with the particle energy, as following:

$$\epsilon_x^{\text{norm}} = \gamma \beta_{rel} \epsilon_x^{\text{rms}} \tag{2.21}$$

with $\beta_{rel} = \frac{v}{c}$, v is the particle velocity, c is the speed of light in the vacuum and $\gamma = \frac{1}{\sqrt{1-\beta_{rel}^2}}$.
An important parameter for describing the transversal motion, is the *tune* that is the number of betratron oscillations, i.e. the number of turns in the phase space, in one machine revolution. It is defined as:

$$T = \frac{1}{2\pi}\varphi(C) = \frac{1}{2\pi}\int_{s0}^{s0+C} \frac{ds}{\beta(s)}. \tag{2.22}$$

The tune is chosen to be an irrational number and it guarantees that the orbit in the phase space is dense. It means that the particle will pass through all the accelerator located at the sigma of its orbit. This irrationality also avoids resonances that can yield the machine to be unstable leading the loss of the beam.
If a particle is at a certain point s_1 of the machine, is possible to predict the evolution of the phase space coordinates by using the *transport matrix*. This matrix allows to calculate x and x' from the point s_1 to a downstream location s_2. The Eq. 2.12 can be rewritten in the following way:

$$x(s) = a\sqrt{\beta(s)}\sin(\varphi(s)) + b\sqrt{\beta(s)}\cos(\varphi(s)) \tag{2.23}$$

where a and b are functions of x and x':

$$a = x(s_1)\left[\frac{\sin(\varphi(s_1)) + \alpha(s_1)\cos(\varphi(s_1))}{\sqrt{\beta(s_1)}}\right] + x'(s_1)\sqrt{\beta(s_1)}\cos(\varphi(s_1)) \tag{2.24}$$

$$b = x(s_1)\left[\frac{\cos(\varphi(s_1)) - \alpha(s_1)\sin(\varphi(s_1))}{\sqrt{\beta(s_1)}}\right] - x'(s_1)\sqrt{\beta(s_1)}\sin(\varphi(s_1)) \tag{2.25}$$

By substituting Eq. 2.24 and Eq. 2.25 in the Eq. 2.23 is possible to obtain the solution for $x(s_2)$ and $x'(s_2)$ in a matricial form:

$$\begin{pmatrix} x(s_2) \\ x'(s_2) \end{pmatrix} = M(s_1|s_2) \begin{pmatrix} x(s_1) \\ x'(s_1) \end{pmatrix} \tag{2.26}$$

where:

$$M(s_1|s_2) = \begin{pmatrix} \sqrt{\frac{\beta_1}{\beta_2}}(\cos\varphi_{21} + \alpha_1 \sin\varphi_{21}) & \sqrt{\beta_1\beta_2}\sin\varphi_{21} \\ -\frac{1+\alpha_1\alpha_2}{\sqrt{\beta_1\beta_2}}\sin\varphi_{21} + \frac{\alpha_1-\alpha_2}{\sqrt{\beta_1\beta_2}}\cos\varphi_{21} & \sqrt{\frac{\beta_1}{\beta_2}}(\cos\varphi_{21} - \alpha_2\sin\varphi_{21} \end{pmatrix} \tag{2.27}$$

where φ_{21} is the phase advance and the matrix $M(s_2|s_1)$ is the *transport matrix*. For *on-momentum* particles with reference momentum p_0, is possible to use the transport matrix to calculate the phase space coordinates x and x' in any points of the accelerator. In the normalized space, the previous formula takes the following simplified form:

$$M(s_1|s_2) = \begin{pmatrix} \cos\varphi_{21} & \sin\varphi_{21} \\ -\sin\varphi_{21} & \cos\varphi_{21} \end{pmatrix} \tag{2.28}$$

that is a classical rotation matrix.

2.1.2 Dispersion

In the transverse plane, the effect of a momentum offset causes the distortion of the close orbit around which the particles perform betatron oscillations. The momentum variation is defined as:

$$\delta = \frac{p - p_0}{p_0} \tag{2.29}$$

for small momentum variations the Eq.2.10 becomes:

$$x'' + K(s)x = \frac{\delta}{\rho(s)} \tag{2.30}$$

The solution of the previous equation is:

$$x(s) = x_\beta(s) + x_\delta(s) \tag{2.31}$$

where x_β is the betatron oscillation around the on-momentum orbit and x_δ is the particular solution of the inhomgeneous equation (2.30) and gives the shift due to the energy variation. It can be also expressed as follow:

$$x_\delta = D(s)\delta \tag{2.32}$$

where D(s) is the *dispersion function* that satisfies the equation:

$$D'' + K(s)D = \frac{1}{\rho(s)} \tag{2.33}$$

The shift for $x'(s)$ can be expressed as above:

$$x'_\delta(s) = D'(s)\delta \tag{2.34}$$

and then the total solution for the angle is:

$$x'(s) = x'_\beta(s) + x'_\delta(s) \tag{2.35}$$

a similar argument can be made for the solution in y. The dispersion effect leads to a shift of the ellipse center in the phase space as is shown in Fig.2.3

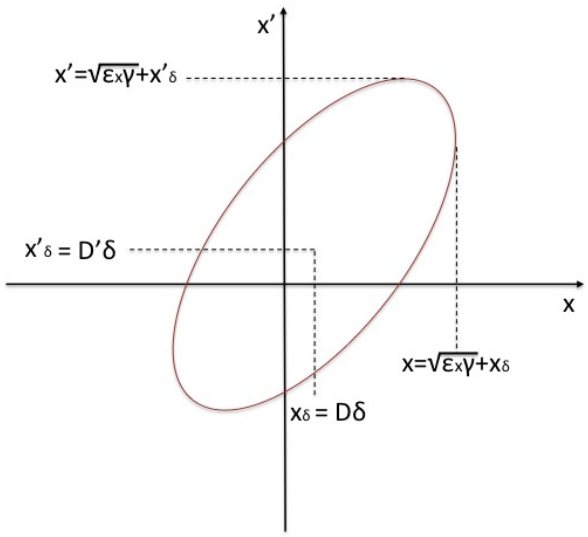

Figure 2.3. Trajectory in the $x - x'$ phase space for a particle with momentum offset δ.

2.1.3 Longitudinal motion: synchrotron oscillations

The longitudinal electric field in the *RF cavities* accelerates the charged particles in the beam. The RF cavities consist of isolate gaps with a sinusoidal voltage applied. When the beam passes through the RF, the particles are accelerated or decelerated depending on the synchronized arrival inside the RF. In order to set the particles inside the accelerating region of the RF period the beam is split in several bunches, the frequency ω_{RF} of the electric field is an integer multiple of the revolution frequency in the ring:

$$\omega_{RF} = h\,\omega_{REV} \tag{2.36}$$

where h is called the harmonic number. The energy gain of the particles at each passage in the cavity is:

$$\Delta E = qV_0 \sin\varphi(t) \tag{2.37}$$

where q is the charge of the particle, V_0 is the amplitude of the potential of the cavity and φ is the phase of the particle with respect to the RF phase. The circulating particles lose energy, in part due to synchrotron radiation, this energy variation changes the length L of the orbit as follows:

$$\frac{\Delta L}{L} = \alpha_c \frac{\Delta p}{p} \tag{2.38}$$

in which α_c is a factor called *momentum compaction factor* [2] and depends only on the bending radius of the particle orbit and the dispersion. Ideally, the reference particle that is synchronous with the RF, arrives always with the same relative phase φ_s. The other particles of the bunch arrive earlier or later and gain different amounts of energy by passing across the RF cavity. Supposing that the particle

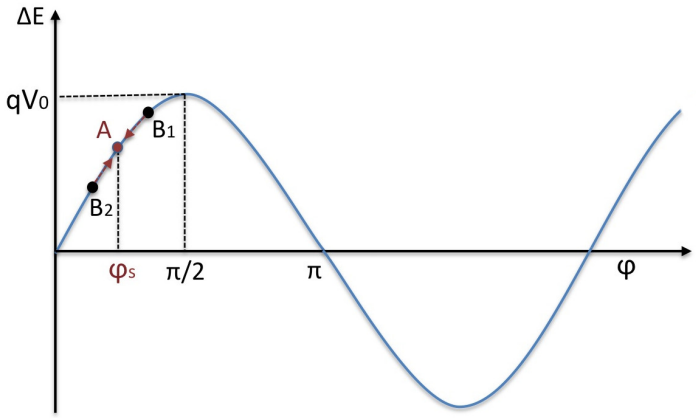

Figure 2.4. Example of energy gain in the RF potential for particles (blue dots) close to the synchronous one (red dots).

velocities are well below the speed of light, a particle B with less energy respect to the synchronous particle, arrives late in the RF and receives an additional amount of energy (see Fig.2.4). In the next turn the energy of the particle B will be greater and it will arrive earlier with respect to A in the RF, receiving a lower energy gain. Therefore the particle B oscillates around the synchronous particle energy position as an harmonic oscillator [3]. The motion in the phase-space diagram is represented by the ellipse showed in Fig.2.5. The phase focusing principle determines the longitudinal stability of the bunch:

$$\frac{\Delta T}{T} = \left(\alpha_c - \frac{1}{\gamma^2}\right)\frac{\Delta p}{p} \tag{2.39}$$

with T being the revolution period in the ring and $\gamma = \frac{E}{mc^2}$ the ralativistic gamma. Two different regimes are defined:

1. $\gamma < \sqrt{\frac{1}{\alpha_c}}$, so-called below transition

2. $\gamma > \sqrt{\frac{1}{\alpha_c}}$, so-called above transition

where the term: $\sqrt{\frac{1}{\alpha_c}}$ is the *transition energy*. In the case 1, the bunch stability is ensured in the angular range $0 < \varphi_s < \pi/2$ corresponding to the rising part of the energy gained showed in Fig.2.4. In this case more energetic protons reach the RF earlier than the synchronous particle ($\varphi(t) < \varphi_s$) so they gain less energy and when they will pass through the RF in the next turn, they will get closer to the synchronous proton. On the contrary, less energetic particles arrive late in the RF ($\varphi(t) > \varphi_s$) gaining more energy and approaching the reference proton in the following turn. Above transition (case 2), due to the relativistic effect of the time dilatation, a particle with higher energy has a longer revolution time and reach the RF later ($\varphi(t) > \varphi_s$). Similay to the case 1, the stability condition is satisfied in the angular range of $\pi/2 < \varphi_s < \pi$. The oscillations performed around the reference

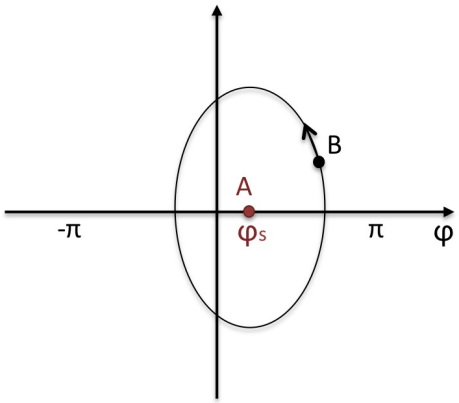

Figure 2.5. Motion in the phase space for a particle (B) that performs oscillations around the synchronous particle (A).

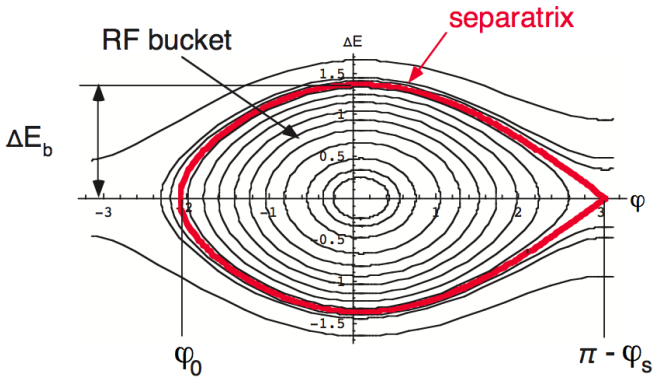

Figure 2.6. Trajectory of the synchrotron oscillations in the phase space.

particle are called *synchrotron oscillations*. For particles with small longitudinal amplitude, the synchrotron oscillations describe a stable motion of equation:

$$\ddot{\varphi} + \frac{\Omega_s^2}{\cos\varphi_s}(\sin\varphi - \cos\varphi_s) = 0 \tag{2.40}$$

where Ω_s is constant. Because the Eq.2.40 is highly non-linear, there is an orbit of stability called *separatrix*. Fig.2.6 represents the motion in the phase space with action-angle variables. The stable particles oscillate on closed orbits within the area delimited by the separatrix. This region of stability is called RF *bucket*. The particles that move on a trajectory beyond of it become unstable and will be lost in the accelerator machine. The limit energy ΔE_b is defined by the following equation:

$$\Delta E_b = k\sqrt{1 - \left(\frac{\pi}{2} - \varphi_s\right)\tan\varphi_s}, \qquad k = constant. \tag{2.41}$$

This gives the *energy acceptance* of the accelerator machine. In the LHC for RF frequency $\omega_{RF} = 400MHz$, the energy acceptance is $\Delta E_b = 3.53 \times 10^{-4}\delta p/p$ at the

nominal energy of 7 TeV.

2.2 Collimation system

During the motion in the accelerator machine, the particles undergo different effects that increase the beam emittance. As a result some particles slowly move towards the walls of the machine populating the beam tails and turn by turn they will be lost. Other effects generate the beam halo that can be dangerous for the accelerator machine. Collimation is needed to avoid background in high energy physics detector, to avoid quenching of the superconducting magnets and to limit the irradiation of equipment in high intensities machine. The collimators are blocks of materials that intercept the particles in the beam tails providing beam cleaning.

2.2.1 Machine aperture and beam acceptance

The vacuum chamber that with different elements installed along the full length (L_m) of the machine (beam screens, collimators, diagnostic equipments, etc.) constitute the physical space where the particle beam moves called geometrical aperture A_{geo}. The aperture is commonly expressed in units of the standard deviation of the beam size in a certain plane $z = (x, y)$, which is defined as follows:

$$\sigma_z(s) = \sqrt{\beta_z(s)\epsilon + (D_z(s)\delta)^2} \tag{2.42}$$

To ensure that at any location, all the particles are contained in the geometric aperture, it must be bigger than the maximum oscillation amplitude of the beam particles. The maximum area of the phase space ellipse, i.e. the maximum emittance, that can be covered by a particle without being lost in the machine, is called *beam acceptance* A_z. It is related to the geometrical aperture A_{geo} in the considered plane z according to the formula:

$$A_z(s) = \frac{(A_{geo} \cdot \sigma_z(s))^2}{\beta_z(s)}. \tag{2.43}$$

A particle that hits the opening will be lost at that location, as soon as it satisfies the following condition:

$$A_z \geq A_{geo} \cdot \sigma_z(s) \tag{2.44}$$

Moreover in a real accelerator the presence of non-linearities in the magnetics fields influence the oscillations of the beam particle, and the so called *dynamic aperture* defines a volume beyond which the particles will not perform stable oscillations but will be lost after some turns. In Fig.2.7 are represented both the dynamic and the geometric apertures.

2.2.2 Beam halo population

The beam halo is constituted by particles of the beam which are transported out from the core. Ideally the core is stable with oscillation amplitude $A << A_{geo}$. On the contrary the halo particles can be lost at the machine aperture after a certain number of turns. The halo is continuously generated by various effects due to several

processes. These cause beam dynamics instabilities with consequent increase of the beam losses. The beam intensity N versus time can be express as follows:

$$N(t) = N(0) \exp\left(-\frac{t}{\tau}\right) \tag{2.45}$$

where τ is the lifetime of the beam for which the initial beam population N(0) is reduced to a fraction 1/e.
The main effects that influence the circulating particle distribution and cause both the emittance growth and the halo population are [5]:

- *Intrabeam scattering*: the beam particles are deflected with small angles due to multiple Coulomb scattering between particles belonging the same bunch [6].
- *Elastic and inelastic scattering:* with the residual gas molecules within the beam pipe.
- *Beam-beam effects:* after the bunches collide elastically scattered particles can populate the beam halo and cause a decrease in luminosity.
- *Synchrotron radiation damping:* ultra-relativistic particles emit electromagnetic radiation when accelerated [7]. The transverse components are not recovered after passing through the RF cavities and the motion in the $x - y$ plane is dumped. These processes are continuos and they spread the particles towards the tails of the Gaussian particle distribution.

The more the halo population grows, the more the beam losses increases turn by turn. The reasons why the beam halo is dangerous for the machine safety are several:

- Far away from the center of the beam the magnet non-linearities become more important. This leads to unstable motion increasing the possibility to lose the beam halo particles in the machine.
- The energy released by the particles impacting in the matter of the machine equipment can cause damage and life reduction of these devices.

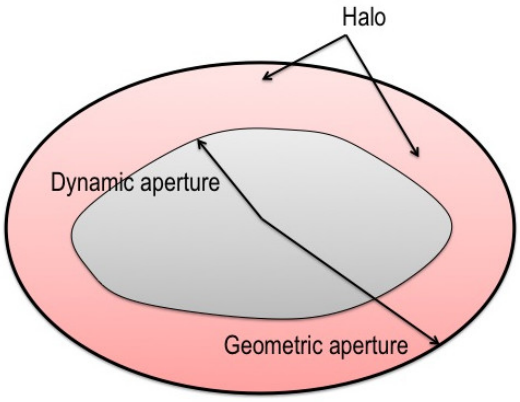

Figure 2.7. Geometrical and dynamic apertures in an accelerator [4].

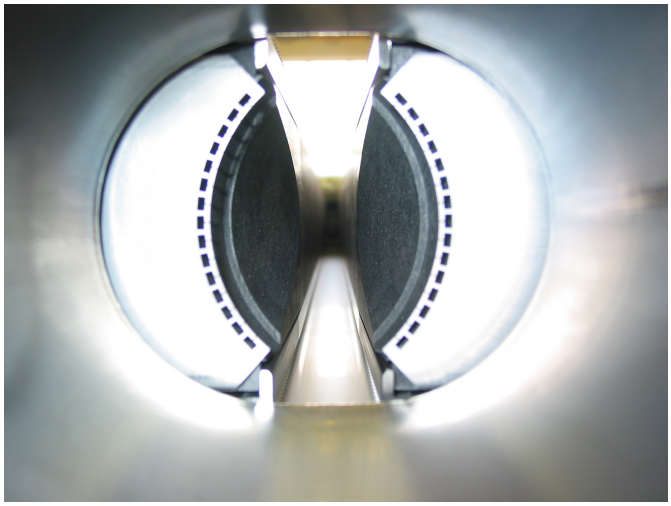

Figure 2.8. Collimator jaws along beam path [8]

- Uncontrolled particle losses in the superconducting magnets can produce energy depositions above the quench limit.
- The halo particles have a large impact parameter and can produce events that can be background source for the experiments.

Therefore, an efficient collimator system is needed to clean continuously the halo particles. Moreover, operation errors like wrong beam injection and extraction, small asynchronies in the dumping system and any other wrong operation that alarm the security systems of the accelerator, can be very dangerous for the machine and the experiments safety. These kind of processes are occasional and unpredictable, then can not be completely avoided, but is possible to limit the damage by means of particle absorbers positioned at the most critical parts of the machine. The collimation system allows to clean the beam halo in a controlled way by concentrating the losses in a dedicated points of the machine. It avoids, or at least reduces, the beam losses on the aperture ensuring the safety of the components and the accelerator itself.

2.2.3 Collimation procedure

Typically, a collimator consists of blocks of material, called jaws (Fig.2.8), located around the beam pipe and installed in several points of the accelerator machine. The jaws are placed between the beam and the mechanical aperture of the machine. The distance between the beam axis and the surface of the jaws is called collimator *half-gap* setting, usually expressed in σ units. Two-stage collimation system is widely used in high intensity machines [9] to localize the beam losses in a restricted area. The closest elements to the beam are the primary collimators, they have to intercept the primary halo particles without interfering with the motion of the beam core. The jaws of the primary collimator are usually made by light Z material that acts mainly as a scatterer on the halo particles. Passing through the jaw, the particles mostly undergo multiple Coulomb scattering that changes the x' angle of the incoming particles. At the exit of the jaw the particles occupy different orbits depending

on the kick received and form a secondary halo. The scattered halo particles can reach the aperture of the machine and for this reason, secondary collimators are installed downstream of the primaries, creating a so called two-stage cleaning system represented in Fig2.9. Because the half-gap of the secondary collimators is larger

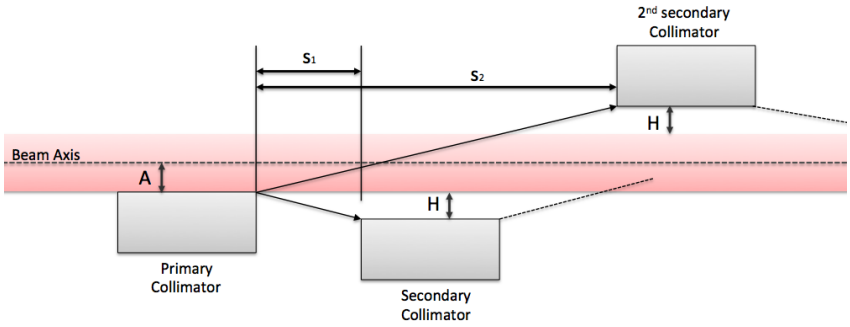

Figure 2.9. Two-stage collimation system.

than the half-gap of the primaries, only the particles which were scattered by the primary collimators are caught. In particular, by placing A and H equal to the normalized distances of the primary and secondary collimators respectively, the particles that escape are contained within a normalized acceptance circle of radius (A+H). If it is within the acceptance of the machine, the particles will be intercepted by the primary collimator some turns later.The minimum scattering angles $\pm b'_{min}$ at the primary collimator needed to reach the secondary collimators are:

$$b'_{min} = \pm \frac{1}{sort\beta_1}(A + H) \sin s_1 \tag{2.46}$$

where β_1 is the β-function at the primary collimator and s_1 is the longitudinal distance between the primary and the secondary collimator.

2.2.4 Cleaning performance

Different parameters are often used to quantify the cleaning performance of the collimation system. If N_p is the number of particle escaping the cleaning insertion with a betatron oscillation amplitude A, bigger than a certain amplitude A_i, and N_{abs} the total number of particles absorbed in the collimation system, the *Global Cleaning Inefficiency*, is defined by:

$$\eta_g(A_i) = \frac{N_p(A > A_1)}{N_{abs}}. \tag{2.47}$$

More the Inefficiency $\eta_g(A_i)$ is smaller, more the cleaning system is efficient. A second parameter must be introduced: the *Local Cleaning Inefficiency*. It provides the distribution of the losses along the ring. For collimation studies is important to know the loss distribution along the ring because the not stopped particles by the collimator material are lost locally in the machine and could cause quenches in the magnets. The Local Cleaning Inefficiency is given by:

$$\eta_c = \frac{N_{loss}}{\Delta s \cdot N_{abs}} \tag{2.48}$$

where N_{loss} refers to the particles lost in a Δs length. In order to avoid magnets quench, the value of η_c must be stayed below the *Local Cleaning Inefficiency at the quench limit*:

$$\eta_c < \frac{R_q \cdot \tau}{N_{tot}} \tag{2.49}$$

in which R_q identifies the maximum allowed particle loss per meter before quench of the magnets, τ is the beam lifetime and N_{tot} is the total beam intensity. The beam lifetime τ, previously introduced by Eq.2.45, is a parameter that quantifies the evolution of the beam loss in a storage ring. In linear approximation, the loss rate from the beam is defined as: N_{tot}/τ.

2.2.5 Maximum beam intensity from cleaning inefficiency

The LHC collimators should withstand losses necessary to run the machine close to the quench limit of the superconducting magnets. The maximum allowed proton loss rate R_{loss} at the collimators is given by the quench limit R_q and the local cleaning inefficiency η_c:

$$R_{loss} = \frac{R_q}{\eta_c} \tag{2.50}$$

that is correlated to the beam lifetime by:

$$\tau \approx \frac{N_{tot}}{R_{loss}}. \tag{2.51}$$

An estimate of the maximum allowed beam intensity N_{tot} at the quench limit is obtained in case of slow continuous losses by combining Eq.2.50 and Eq.2.51 [5]:

$$N_{tot}^{\max} = \frac{\tau \cdot R_q}{\eta_c} \tag{2.52}$$

Therefore, the maximum charges injected in the machine is limited by the performance of the collimation system (η_c): for a given beam lifetime, the higher the local cleaning inefficiency, the lower is the number of particles that can circulate in the ring without inducing superconducting magnets queches. From Eq.2.52 the equivalent quench limit η_q can be calculated as follows:

$$\eta_q = \frac{\tau^{\min} \cdot R_q}{I_{nom}} \tag{2.53}$$

where $I_{nom} = N_{tot}$ is the nominal beam intensity and $\tau^{\min}$ is the the minimum beam lifetime. Local losses on superconducting magnets must always be compared to η_q in order to estimate $N_{tot}^{\max}$.

Chapter 3

The Large Hadron Collider

At CERN, the European Organization of Nuclear Research, takes place the world's largest and most powerful particle accelerator: the Large Hadron Collider (LHC) [10]. It is a circular accelerator designed with the aim of testing the predictions of The Standard Model particle theory, particularly looking for the theorized, and now discovered, Higgs boson and possible supersymmetric particles predicted by the supersymmetry theory. The LHC is located at the Franco-Swiss border near Geneva and is installed in a 27 km long circular tunnel at a depth ranging from 50 to 175 m underground. The LHC is capable of accelerating protons and ions. The design centre-of-mass energy for protons and ions collisions is at 14 TeV and

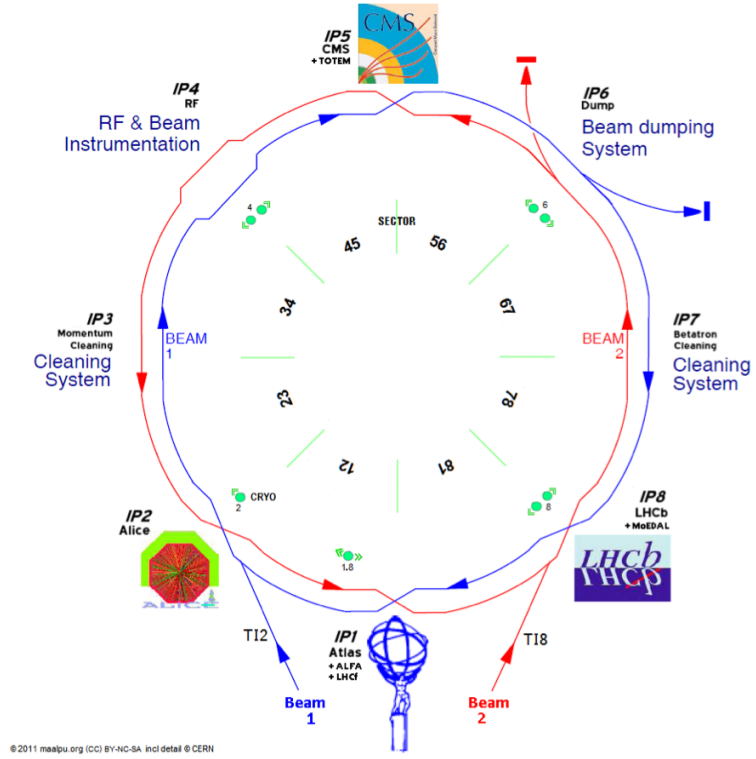

Figure 3.1. Layout of the LHC. Four sections host the experiments, other the collimation, the RF and the dump system [8].

1.15 PeV respectively. The two beams are bent to stay on their circular orbits by super conducting magnets cooled in a bath of superfluid helium to 1.9 K degrees. They collide in four detectors of the LHC experiments: ALICE, ATLAS, CMS and LHCb. Since 2010 the LHC was running. The first period 2010-2011 at 3.5 TeV per beam, then in 2012-2013 the beam energy was increased to 4 TeV. The design parameters are not yet achieved and for this reason on March 2013, the LHC has started a shutdown period (LS1) in order to upgrade the machine and make it ready to reach the nominal beam energy. The re-starting of the machine is expected in the early 2015.

3.1 The accelerator complex

The LHC is the last of a complex accelerator chain (Fig.3.2) that allows to reach the operation energy for the circulating beams in the LHC ring [11]. After the extraction from the hydrogen source at about 50 keV, the protons enter in the 35 m long LINear ACcelerator (LINAC), where their energy is increased up to 50 MeV. After they are injected in the the Proton Synchrotron Booster (PSB) that brings them to 1.4 GeV. With this energy they are ready to be transferred in to the Proton Synchrotron (PS) where are grouped into trains of bunches with 25 or 50 ns spacing and they reach the energy of 26 GeV. Then, the protons are transferred to the SPS (Super Proton Synchrotron), where they are accelerated up to 450 GeV and finally injected into LHC split in two beams. The LHC is divided in several insertions (IRs) where all the components and the experiments are installed [13]. The 27 km length are divided into eight arcs and eight straight sectors, that consist in 23 FODO cells. The superconducting dipoles of 15 m length each, are designed to work with a 8.3 T magnetic field at the temperature of 1.9 K. The two beams (Fig.3.1) are injected into the machine in IR2 (Beam 1) and IR8 (Beam 2) and accelerated up to the nominal top energy by the radio frequency cavities located in IR4. The four collision points host the detectors: the two biggest experiments are ATLAS (A Toroidal LHC ApparatuS) [14] (Point 1) and CMS (Compact Muon Solenoid) [15] (Point 5). LHCb (Large Hadron Col- lider beauty) [16] (Point 8) is dedicated to study the decay of B mesons and ALICE (A Large Ion Collider Experiment) [17] (Point 2) is optimized for heavy ions collisions. The normal operation of the machine is called the *Physics* period, during which the beams are stored and kept colliding for many hours. Once the Physics period ends or in case of a failure, a dump system located in IR6 extracts the beams from the ring. The insertions IR3 and IR7 are dedicated to the momentum and betatron cleaning respectively.
One of the most critical parameters for a particle collider is the *Luminosity*. It is defined by the accelerator parameters, as follows:

$$\mathcal{L} = \frac{n_b N_b^2 f \gamma}{4\pi \epsilon_n \beta^*} F \tag{3.1}$$

where N_b is the number of particles per bunch, n_b is the number of bunches per beam, f is the revolution frequency, γ is the relativistic gamma, β^* the beta function at the collision points and F the geometric luminosity reduction factor due to the crossing angle of the colliding bunches. $\epsilon_n = \epsilon \beta_{rel} \gamma_{rel}$ is called normalized transverse

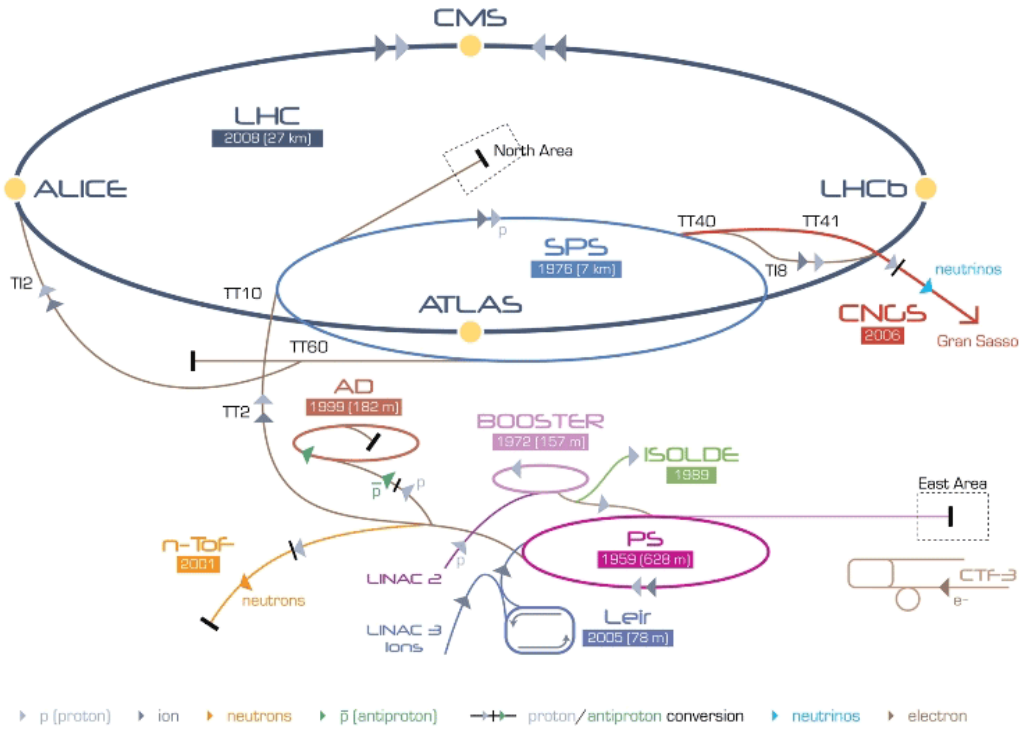

Figure 3.2. Accelerator complex at CERN [12].

beam emittance and it stays constant with the energy. The $\mathcal{L}$ allows to calculate the interaction rate for a certain process: $dN_p/dt = \sigma_p \cdot \mathcal{L}$, where σ_p is the process cross section. The higher is the luminosity, the greater is the number of interesting events produced during each collision. In 2011, with beam energy of 3.5 TeV the maximum peak luminosity arrive to $4{\times}10^{33}$ cm^{-2} s^{-1}. In 2012, with beam energy of 4 TeV the maximum peak luminosity arrive to $0.77{\times}10^{34}$ cm^{-2} s^{-1}, still below the designed luminosity of 10^{34} cm^{-2} s^{-1} but allowed to produce enough events to discover the Higgs boson. The main parameters for the nominal proton beam operation are shown in Table 3.1.

3.2 The LHC collimation

The superconducting magnets would quench at 7 TeV even if a small amount of energy (around 30 mJ/cm^{-3}, corresponding to a local loss of $4{\times}10^7$ protons) is deposited into the superconducting magnet coils. Therefore, a very efficient collimation system is required in order to intercept and absorb any beam losses in a safe and controlled way.

3.2.1 LHC collimator design

The closest parts to the beam are the collimator jaws. Most of the LHC collimators consist in two jaws with the beam passing in the centre between them, see Fig.3.3 and 3.4. They are made of different materials, according to their role in the hierarchy discussed in 2.2.3. The jaw surfaces are constituted by a flat part, determining the active length (different for each collimator type) and by a 10 cm tapering part at both

Table 3.1. LHC main design parameters from [13]. The table shows the design values of the parameters (at injection and collision). The last column contains the values used during the 2012 physics operation.

	Injection	**Design collision**	**2012 collision**
Beam data			
Energy [GeV]	450	7000	4000
Relativistic gamma	479.6	7461	4263
Number of particle per bunch	1.15×10^{11}		1.4×10^{11}
Number of bunches	2808		1380
Bunch spacing [ns]	25		50
Transversal normalized emittance [µm rad]	3.75		2.5
Stored energy per beam [MJ]	23.3	362	146.5
Energy loss per turn [eV]	1.15×10^{-1}	6.71×10^{3}	0.72×10^{3}
Peak luminosity related data			
RMS bunch length [cm]	11.4	7.55	9.73
Geometry luminosity reduction factor F	-	0.836	0.79
Peak luminosity in IP1 and IP5 [$cm^{-2}s^{-1}$]	-	1.0×10^{34}	0.77×10^{34}
Geometry			
Ring circumference [m]	26658.883		
Ring separation in arcs [mm]	194		
Magnets			
Number of main bends [m]	1232		
Length of main bends [m]	14.3		
Bending radius [m]	2803.95		
Field of main bends [T]	0.535	8.33	4.76
Lattice			
Horizontal tune	64.28	64.31	64.31
Vertical tune	59.31	59.32	59.32
Momentum compaction α_c	3.225×10^{-4}		
Gamma transition γ_{tr}	55.68		
RF system			
Revolution frequency [kHz]	11.245		
RF frequency [MHz]	400.8		
Harmonic number	35640		
Total RF voltage [MV]	8	16	12
Synchrotron frequency [Hz]	61.8	21.4	26.3

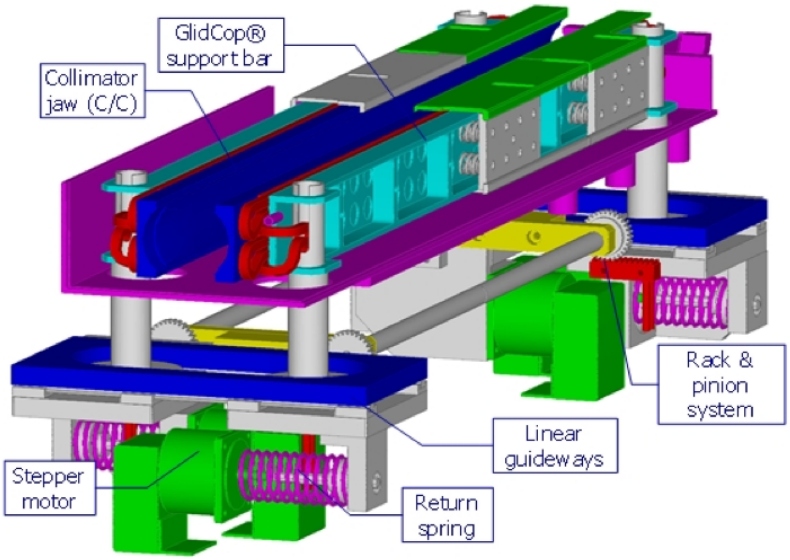

Figure 3.3. Scheme of LHC collimator [8].

ends to minimize geometrical impedance effects. An important feature is that they are movable in order to efficiently intercept the beam halo. Indeed, the collimator jaws must always be centered and aligned with respect to the beam envelope and the actual orbit. The two collimator jaws are put in a vacuum tank. The cooling of jaws and tanks is provided by a heat exchanger with copper-nickel pipes. The aperture and the tilt angle of the jaw is set by four precise stepping motors per collimator. In addition a fifth motor can shift transversally the whole collimator tank for some special collimators. The mechanical stress caused by the contact between materials (jaws and heat exchanger) having different thermal expansion coefficient, is avoided by a GlidCop support bar that presses the cooling pipes against the jaw material by means of clamping springs. This system also enhances the thermal contact between them. Depending on their orientation in the space, collimators can be horizontal, vertical or skew. The azimuthal angle for the skew ones is defined by starting from the positive x-axis and rotating clockwise in the $x - y$ plane.
One of the most discussed point of the collimator design concerns the choice of the material of the jaws. Materials with high atomic number Z, like tungsten, are preferable to reach a sufficient absorption rate for cleaning task. However they are much less robust against mechanical damage than low Z materials (graphite for example) that are preferred to reduce the power deposition in the jaw. Primary

Table 3.2. Material jaws for different collimator types.

Collimator type	Length [m]	Material
Primary	0.6	C
Secondary	1.0	C
Tertiary	1.0	W
Absorber	1.0	C
TCL	1.0	Cu

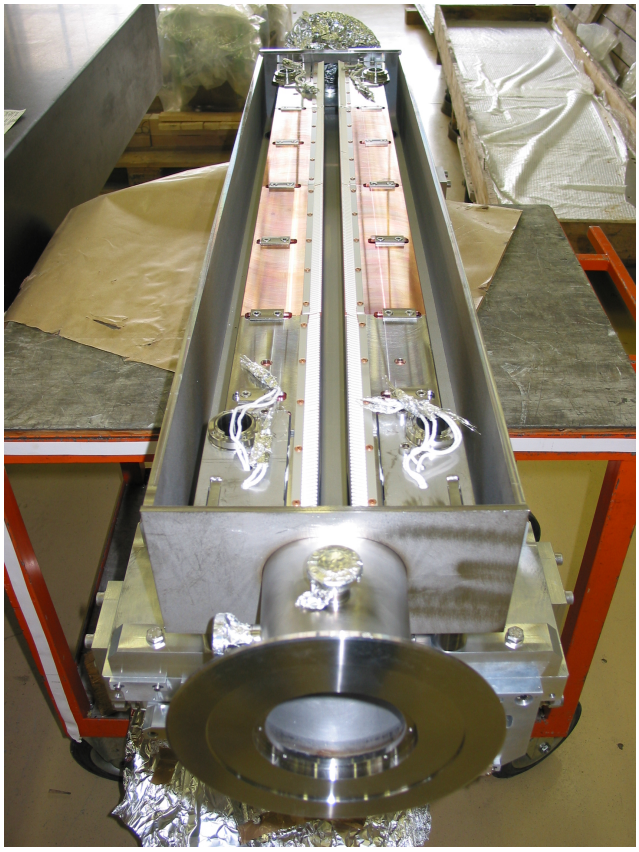

Figure 3.4. Top collimator view. The collimator is installed along the beam pipe. The beam passes within the two movable jaws [8].

and secondary collimator are made of Carbon. In Table 3.2 are summarized the collimator materials used. In order to reduce the risk of beam instabilities [13], the impedance of the collimators should be kept low. On the other hand, a system with sufficiently low impedance, like a copper based one, would induce a risk of material jaw damage in case of high beam losses, with a consequent reduction of the cleaning performance of the collimation system. The choice of a low Z material for primaries and secondaries collimator reduces the energy deposition in the jaws and makes the collimator robust. The primary collimators have an active length of 60 cm, while a 1 m length was chosen for the secondaries, they are built with fiber-reinforced graphite (CFC) jaws. A high Z material is chosen for the absorbers in order to increase the absorption rate.

3.2.2 The multi-stage collimation system at LHC

In the LHC case, the two-stage collimation system described in section 2.2.3 is extended in a multi-stage collimation system. The outgoing particles from the secondary collimators populate the tertiary halo, that can be lost in the cold aperture of the LHC machine. To avoid quenches of superconducting magnets, the tertiary halo particles must be minimized, for this reason further absorbers and tertiary collimators are installed in the most sensitive regions of the machine. In

Fig.3.5 is shown a schematic view of the LHC multi-stage collimation system.
For the beam cleaning is possible to have two different type of cleaning: the betatron and the momentum. The first one allows to limit the transverse extension of the beam halo by removing particles with high betatron amplitude. The second one removes the halo particles that perform large synchrotron oscillations having a large momentum deviation respect to the reference particle. In the case of LHC, there are two different insertions that fulfill the two task separately. Fig.3.6 shows a complete layout (not in scale) of all installed collimators in the LHC with the insertions dedicated to the betatron and momentum cleaning:

- *Betratron cleaning insertion* (IR7): this point of the machine is characterized by low dispersion value and so the transversal shift due to the momentum offset is negligible. In this way the particles at large distance from the beam have a high betatronic amplitude mostly.
- *Momentum Cleaning insertion* (IR3): here the dispersion is higher and the halo particles have a high momentum offset. This insertion, due to optics constraints, the $\beta-$function is not negligible in IR3.

Both the momentum cleaning and the betatron cleaning are performed in the LHC with the multi-stage collimation system.

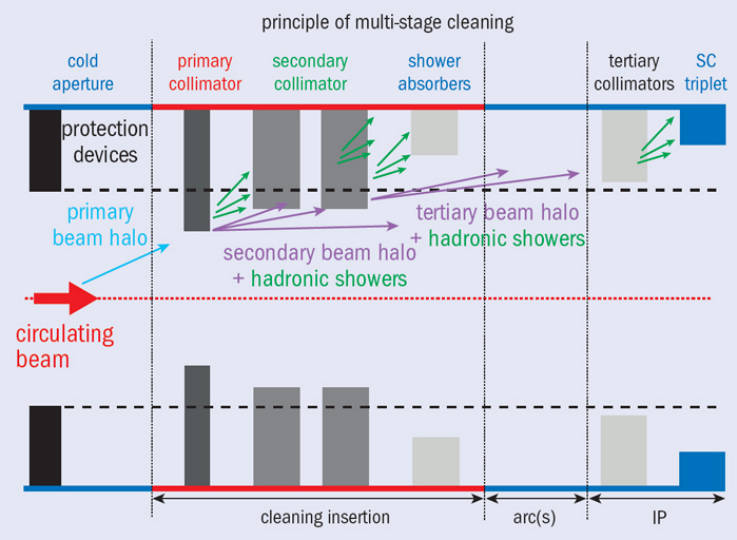

Figure 3.5. Schematic layout of the LHC multi-stage collimation system [18].

3.2.3 Collimator layout for beam cleaning and experiments protection

The LHC collimator hierarchy consists in primary (TCP) and secondary (TCSG) collimators and tertiary (TCLA). At LHC energies, the TCP cannot absorb all protons from the primary halo and a secondary halo leaks out. Secondary collimators (TCSGs), downstream of the TCPs and more open, intercept it. The TCLAs are more open than the TCSGs and must intercept the particles even farther away

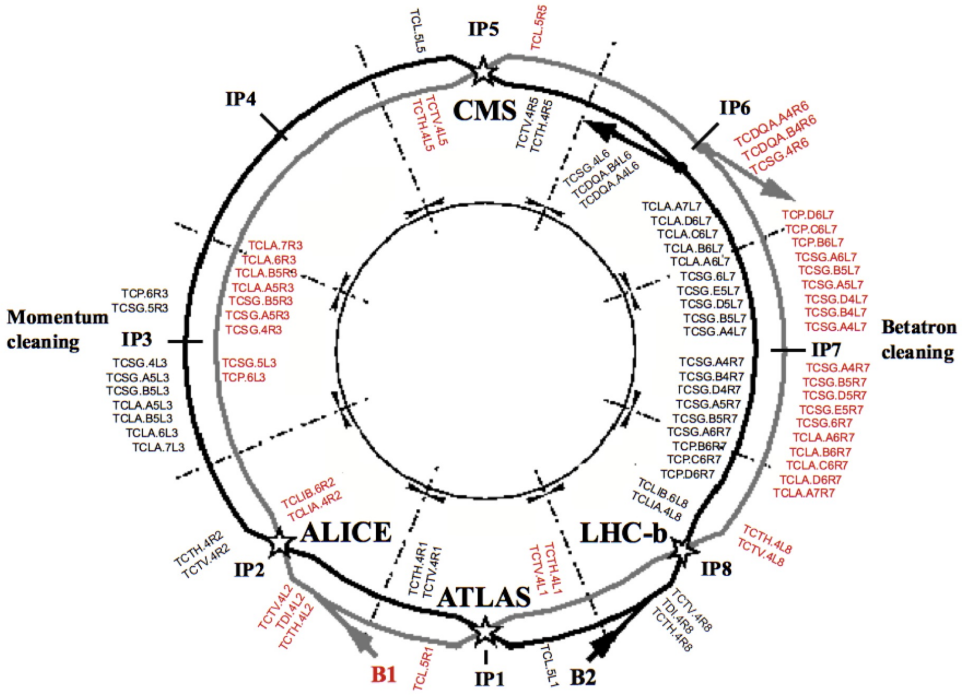

Figure 3.6. General collimators layout and cleaning insertions of LHC [5].

from the core (tertiary halo) and the showers produced by inelastic interactions of the protons inside the TCP and the TCSG jaws. The collimator settings with the half-gap positions for different beam energies are shown in Table 3.3.
Some special collimators are installed in the most critical location of the ring. In order to protect the LHC against possible losses following equipment failures or wrong operation. The injector beam stoppers (TDIs) are vertical collimators made of carbon-carbon jaws of 4.2 m length. They are installed to ensure a correct beam injection setup even in case some of the injector kickers fails: the upper jaw, intercepts particles not sufficiently deflected by the kickers, while the lower jaw catches miskicked beam. In addition, TCLI two-sided vertical collimators are located in IR2 for Beam 1 and IR8 for Beam 2. This type of collimator are moved in when the beam is injected and then retracted before the particle acceleration. In IR6, a dump protection collimator, called TCDQs, is placed, followed by a TCSG that, in case of malfunctioning of the beam extraction system, protects the machine. The TCDQs are several one-side horizontal collimators of 3 m length.
Tertiary collimators TCTH (horizontal) and TCTV (vertical) are installed upstream of the triplet magnets near the experimental points. The triplets are quadrupoles used to reduce the beta function at the collision points (IR1, IR2, IR5 and IR8). The TCTs provide protection during the squeeze of the beam and the collision and also reduce the halo related background in the detectors. They are two sided collimators with 1 m tungsten jaws. Copper absorbers (TCL) protect the machine from particle showers (debris) coming from the collisions in IR1 and IR5, where high luminosity is

Table 3.3. Collimator settings for the different families in the cleaning hierarchy, expressed in units of the beam size σ, at different energies: 450 GeV (injection), 4 TeV (top energy in 2012), 7 TeV (expected top energy after long shutdown) assuming ϵ_{norm}=3.5 µm rad.

		half-gap[σ]		
		450 [GeV]	4 [TeV]	7 [TeV]
IR3	TCP	8.0	12	15
	TCSG	9.3	15.6	18
	TCSM	open	open	open
	TCLA	10	17.6	20
IR7	TCP	5.7	4.3	6.0
	TCSG	6.7	6.3	7.0
	TCSM	open	open	open
	TCLA	10	8.3	10
IR6	TCDQ	8.0	7.6	8.0
	TCSG	7.0	7.1	7.5
IR1	TCTH	13	9.0	8.3
	TCTV	13	9.0	8.3
IR2	TCTH	13	12	25
	TCTV	25	12	25
	TCLI	7.0	open	open
	TDI	6.8	open	open
IR5	TCTH	13	9.0	8.3
	TCTV	13	9.0	8.3
	TCLP	25	10	15
IR8	TCTH	13	12	25
	TCTV	13	12	25
	TCLI	7.0	open	open
	TDI	6.8	open	open
	TCXRP	open	open	open
	TCRYO	open	open	open

reached. After the energy ramp, the beam is squeezed in preparation of the physics operation. Unlike the other collimators, the TCTs are also moved in during the squeeze.

Chapter 4

Collimation cleaning setup

SixTrack is a code written in Fortran-77 used for collimation and beam cleaning studies [19]. The first purpose of SixTrack was to study non linearities and dynamic aperture in circular machines tracking pairs of particles through an accelerator structure over a large number of turns. Aftertwords, the SixTrack code was extended in a new sophisticated version which tracks a large number of halo particles interacting with the collimators [20].

4.1 SixTrack for collimation

The SixTrack code treats the six-dimensional vectors of coordinates (x, x', y, y', s, E), where the s coordinate is the longitudinal position (parallel to the beam direction), E is the energy of the proton, x and y are the perpendicular coordinates to s and x' and y' the angles (Fig.2.1). It is based on an element-by-element tracking using transfer matrices to describe the effect of each lattice element. With a magnet system model it considers the non-linearities up to the 20th order. The new SixTrack version includes the COLLTRACK/K2 program. The K2 code was developed during the 1990's for LHC collimation studies [21]. It is a scattering routine based on a Monte Carlo method that simulates all the physical interactions between the hitting particle and the matter of the collimator jaw. After the end of 2000 the K2 routines were included into the COLLTRACK program which allows to track few millions of particles over hundreds of turns for different halo types and simulate proton scattering processes in various collimator materials, including point-like elastic and inelastic interactions and single-diffractive events. The COLLTRACK/K2 is implemented as a part of the SixTrack source code and this updated version is nowadays the main tool for tracking particles and collimation studies for LHC.

4.2 Particle Tracking

During a SixTrack run, the particles are tracked through the lattice element by element. Their coordinates are transformed according to the type of element using a map derived from the electromagnetic field [4]. The machine optics layout is defined by the *MAD-X* program [22]. To calculate the LHC optics it requires the specification of some parameters such as the magnetic strength and sequence of the

machine elements (including collimators) for the tracked beam (Beam 1 or Beam 2), beam energy, type of tracked particles, crossing and separation schemes at the interaction points. The lattice of the machine is approximated by the model called *thin lens*. The lattice elements have no longitudinal extension and is schematically represented by a marker located at the centre of the elements itself. The whole element length is replaced by a drift space and the distance between two consecutive components is given by the real distance between them plus the half length, see Fig.4.1. The thin lens formalism is used to reduce the CPU effort that would occur as a result of thick-lens tracking. In some cases, in order to increase the precision for a thick element is possible to split it in several thin lenses.

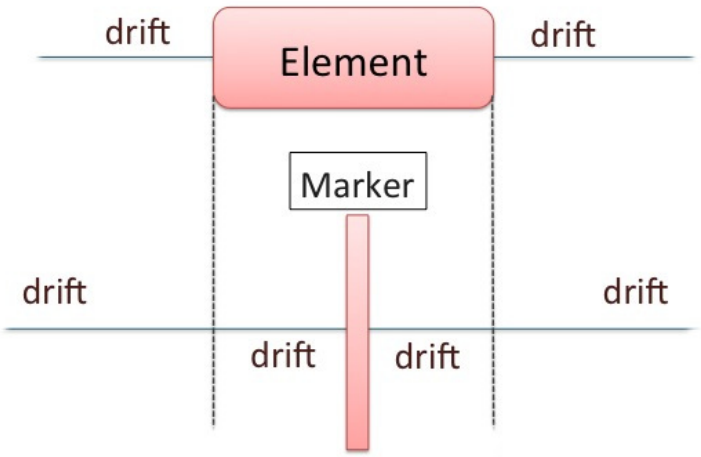

Figure 4.1. The thin lens formalism. On the top, an element in the lattice, on the bottom the same element in the thin lens scheme.

4.3 Input files to run SixTrack

The latest version of the SixTrack source code for collimation studies can be found at: ***SixTrack code web-page***.
To perform SixTrack simulations are needed specific input files containing details about:

- machine lattice, in particular magnetic strength and sequence of the machine elements (including collimators)
- collimator properties: name, opening, length, material, rotation angle, offset and β-function at collimators
- SixTrack setting with the main tracking parameters such as maximum number of turns, number of particles and energy.

```
SINGLE ELEMENTS------------------------------------------------------------
ip1              0   0.000000000e+00   0.000000000e+00   0.000000000e+00   0.000000000e+00   0.000000000e+00   0.000000000e+00
drift_0          0   0.000000000e+00   0.000000000e+00   1.500000000e+00   0.000000000e+00   0.000000000e+00   0.000000000e+00
mbas2.1r1       25   0.000000000e+00   0.000000000e+00   0.000000000e+00   0.000000000e+00   0.000000000e+00   0.000000000e+00
drift_1          0   0.000000000e+00   0.000000000e+00   1.851500000e+01   0.000000000e+00   0.000000000e+00   0.000000000e+00
tas.1r1          0   0.000000000e+00   0.000000000e+00   0.000000000e+00   0.000000000e+00   0.000000000e+00   0.000000000e+00
d_c6t_17         0   0.000000000e+00   0.000000000e+00   3.587000000e+00   0.000000000e+00   0.000000000e+00   0.000000000e+00
mqxa.1r1..1      2  -1.390283835e-02   0.000000000e+00   0.000000000e+00   0.000000000e+00   0.000000000e+00   0.000000000e+00
drift_5          0   0.000000000e+00   0.000000000e+00   1.698666667e+00   0.000000000e+00   0.000000000e+00   0.000000000e+00
drift_7          0   0.000000000e+00   0.000000000e+00   1.144000000e+00   0.000000000e+00   0.000000000e+00   0.000000000e+00
mcbxh.1r1        1  -1.000000000e-05   0.000000000e+00   0.000000000e+00   0.000000000e+00   0.000000000e+00   0.000000000e+00
mcbxv.1r1       -1  -1.000000000e-05   0.000000000e+00   0.000000000e+00   0.000000000e+00   0.000000000e+00   0.000000000e+00
```

Figure 4.2. Fragment of the fort.2 file used to describe the geometry and strength parameters in SixTrack.

4.3.1 Machine lattice

The machine lattice can be provided to SixTrack through the input file *fort.2*. For the work presented here, this file is obtained by running MAD-X using the LHC official layout [22]. This is the standard tool to describe particle accelerators, simulate beam dynamics and optimize beam optics. The command: "*sixtrack, radius=17E-03*", generates a file called *fc.2* with the basic structure of the lattice. This file, renamed as *fort.2* [19], is used by SixTrack for the element-by-element tracking. Fig.4.2 shows a section of the fort.2 file. MAD-X dumps all the consecutive linear element in one bloc and all the non linear elements in-between. The single element properties are read by parsing the fort.2 file. The first column is the name of the element, and the other the element properties.

4.3.2 Collimator properties

In the case of running SixTrack for collimation studies, a collimator database, containing the details of all the collimators, is also read. This file is called *CollDB_2012_b1* for Beam 1, and *CollDB_2012_b2* for Beam 2, it contains the following information:

- Total number of collimators
- Collimator name
- Collimator setting expressed in σ units from the beam centre (this parameters can be also setup later in the fort.3 file, if so, the setting here will be ignored)
- Collimator jaw material:
- Jaw active length [m]
- Azimutal angle [rad] of collimator jaws
- Transverse collimator gap offset respect to the centre of the beam orbit [m]
- The Twiss parameter β_x and β_y [m] at the collimator location

Fig.4.3 shows a section of this file.

Table 4.1. Collimator materials and densities implemented in SixTrack.

Material	Density [g cm^{-3}]
C=Carbon	2.26 (1.65)[1]
C2=Carbon	4.52
BE=Beryllium	1.848
AL=Aluminum	2.70
CU=Copper	8.96
W=Tungsten	19.3
PB=Lead	11.35

[1] This density is implemented in the new SixTrack version (see Chap.5).

4.3.3 SixTrack setting file

SixTrack setting and the main tracking parameters are set up in the *fort.3* file. It contains the number of particles to be tracked, given as a multiple of 64, the beam energy, the emittance both in the horizontal and vertical plane and the halo type distribution. The tracking can be performed for a beam halo generated in the the chosen plane (horizontal or vertical) with a smear $\pm\delta A_{x,y}$ around the normalized amplitude $A_{x,y}$ in σ units. The smear gives information about the "thickness" of the halo. Therefore, no computing time is lost tracking the beam core. In this file is possible to choose one of the following halo distributions [8]:

1. Flat distribution in the selected plane between $A_x \pm \delta_x$ (horizontal) or $A_y \pm \delta_y$ (vertical). The amplitude in the other plane is zero.

2. Flat distribution in the selected plane with a Gaussian distribution cut at 3σ in the other plane. This is illustrated in Fig.4.4 where on the left is shown the distribution in the phase space plane $(x - x')$ and $(y - y')$ and on the right the distribution in the transverse plane $(x - y)$. In particular, this case is used in the simulations presented here.

3. Flat distribution in the selected plane plus a Gaussian distribution cut at 3σ in the other plane, with an energy spread and a longitudinal bunch length defined.

4. Halo distribution read from an external file.

5. Radial transverse distribution of radius A_r that corresponds to a flat distribution both in the horizontal and vertical planes with $A_x = A_y = A_r/\sqrt{2}$

In addition is possible to use the *pencil-beam* configuration on the selected collimator. In this case is possible define the desired impact parameter in sigma units on the collimator selected, the offset and the energy spread of the halo particle. The distribution types available for the pencil-beam case are: pencil-like distribution, rectangular beam, Gaussian beam both in x and y directions and rectangular beam in x and Gaussian in y.

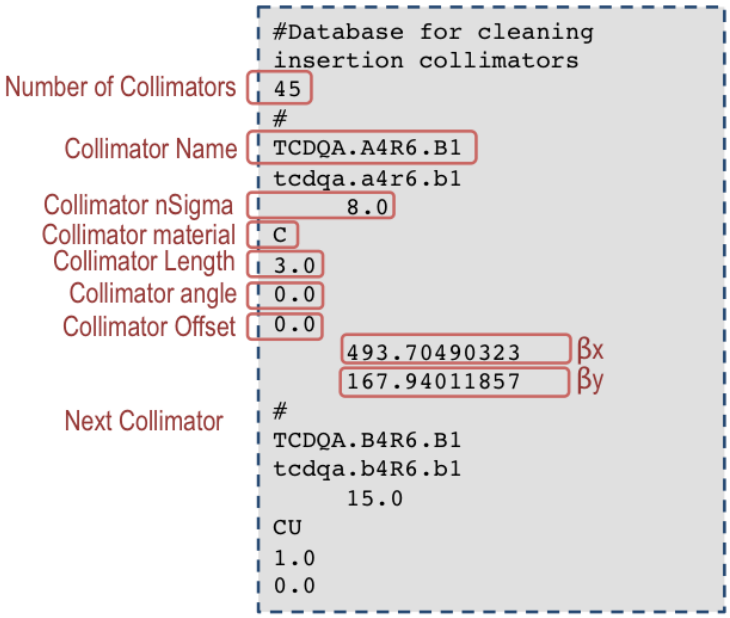

Figure 4.3. Fragment of the collimator database file with the tracking parameters and collimator setting.

In the fort.3 file is also possible to select the collimator setting (in sigma units) instead of using the collimator database. In Fig.4.5 is shown a section of the fort.3 file.

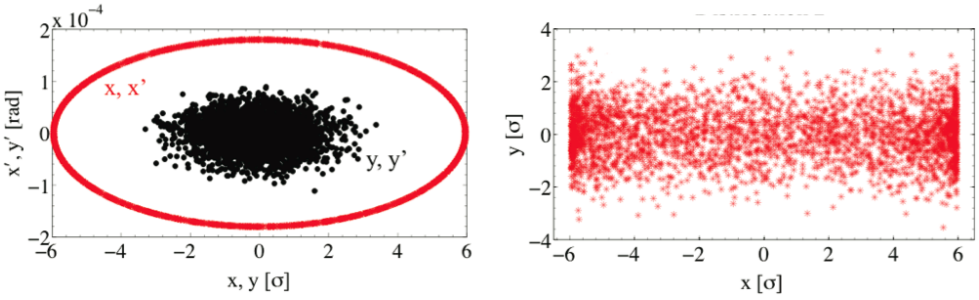

Figure 4.4. Halo distribution in the phase space $(x - x')$and $(y - y')$ and transverse plane $(x - y)$ for the case of a flat distribution in the selected plane with a Gaussian distribution cut at 3σ in the other plane [5].

4.4 Post processing and simulation outputs

SixTrack computes the trajectories of the halo particles along the accelerator machine by using the six-dimensional phase space coordinates (x, x', y, y', s, E). The particles interact with the collimator and they are tracked until an inelastic scattering occurs within the jaw. Scattered particle trajectories are stored in the *tracks2.dat* file. The transverse coordinates information about the inelastic interactions occurred are

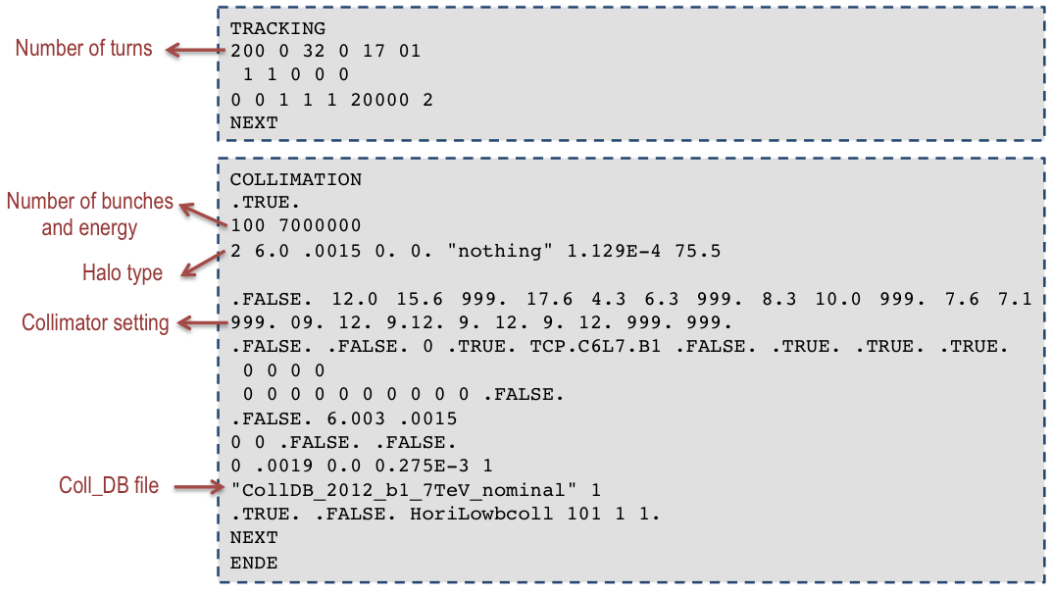

Figure 4.5. Extract from the *fort.3* input file to the SixTrack collimation routine

contained in the *FLUKA_impacts.dat* file. The *FirstImpacts.dat* file contains the transverse and longitudinal coordinates at the entrance and at the end of the jaw for the ingoing and outgoing protons that hit the collimator for the first time. This file contains also the *impact parameter* b defined as the transverse offset between the impact location and the edge of the jaw. A summary of the number of impacts on the jaw and absorbed protons for each collimator, is given by the output file *coll summary.dat*. The information related to the collimator setting and main optics parameters at the collimators are listed in the *collgaps.dat* file, in addition the *efficiency.dat* file contains the global cleaning efficiency data defined in Eq.2.47. In order to localize the losses along the LHC ring, a post processing comparison between the aperture model, not including collimators and protection elements, and the particle trajectories from the SixTrack output file tracks2.dat is needed. This comparison is performed by the *BeamLossPattern* program that permits to identify loss locations with an arbitrary resolution Δs. Then is generated the output file *LPI_PartLost.dat* with 10 cm resolution. In Fig.4.6 is shown an example of a particle trajectory in the LHC aperture model. By using the LPI_PartLost.dat file another program called *CleanInelastic* cleans up the FLUKA_impacts.dat from the fake absorptions due to particles formerly lost in the machine aperture and keeps only the information about particles absorbed in the collimator jaws. Then a new file, called *impacts_real.dat* is generated. This is the main input for energy deposition and background studies performed by the FLUKA code [24, 25, 26]. FLUKA program calculates the showers of particles generated by the inelastic interactions of the primary protons with the different collimator jaw materials.

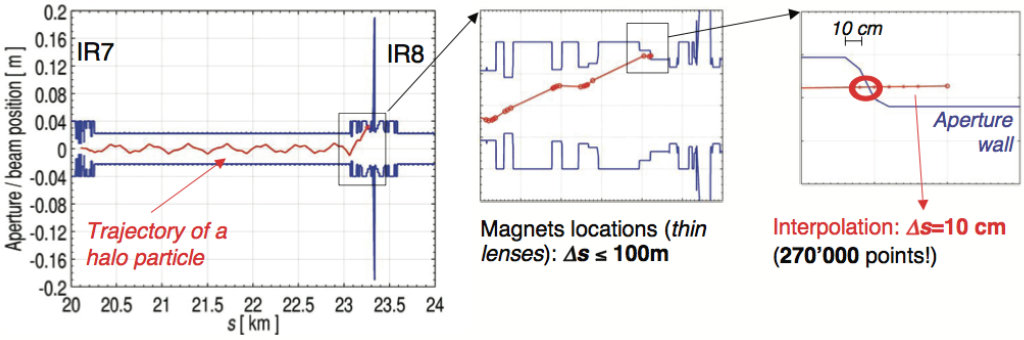

Figure 4.6. Example of a trajectory of a particle lost in the LHC aperture [23]

4.5 SixTrack reference plots for collimation studies

SixTrack is a complex software, when it is run for collimation studies, the user can configure many parameters such as: the machine layout, collimator setting, beam halo, etc... In order to validate the code that is being used and check the input parameters, we have developed a Python software library to generate a set of reference plots. This can be useful for several reasons:

- to validate changes made on local private versions,
- to verify different kind of input parameters,
- for comparisons with other tracking routines and
- as a starting point for new user on SixTrack simulations.

A summary of the reference plot types with the respective files needed is shown in Fig.4.7. In the next sections will be presented the most relevant reference plots.

File Name	Plot type
• impacts_real files • LPI files	✓ Standard LossMaps
• impacts_real files • FirstImpacts files • FLUKA_impacts files • Dist0 files	✓ Phase Space (x' vs x) ✓ Phase Space (y' vs y) ✓ Transverse Distibution (y vs x)
• impacts_real files • FLUKA_impacts files	✓ Absorption s_pos. in the jaw
• LPI files	✓ Transverse Distribution for LPI losses
• impacts_real files	✓ Number of particles absorbed at TCT collimator and at IR6
• collgaps.dat file	✓ Positions in number of σ for all the collimators

Figure 4.7. Summary list of reference plots with the SixTrack output files to generate them.

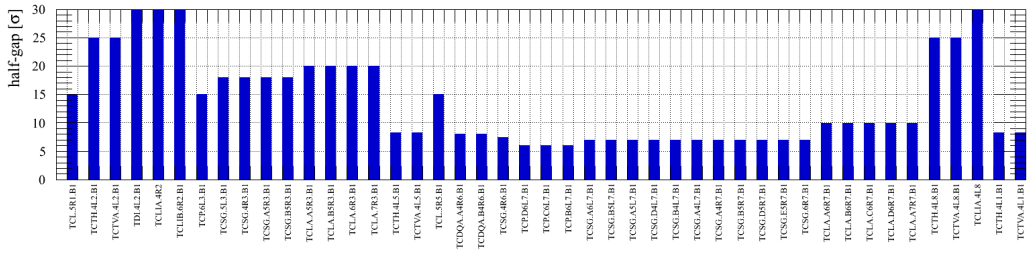

Figure 4.8. Collimator setting with the half-gap in σ units for the 7 TeV case.

4.5.1 Collimator setting and layout

As discussed in section 4.1.3, from the collgaps.dat file is possible to collect information about the collimators used. In particular, it contains the IDs to identify the collimators, the rotation angle of each collimator, the β_x and β_y (expressed in meters) at the collimator location, the half-gap both in meters and σ units, the jaw material and the collimator length, the tilt angles and the σ_x and σ_y (in meters) at the collimator. The reference plot in Fig.4.8 shows the complete 7 TeV collimator settings, the collimators with a half-gap larger than $25\,\sigma$ are totally open. This setting corresponds to the nominal configuration shown in Table 3.3 The complete collimator layout for the same energy beam is represented in fig.4.9. It shows the position along the LHC ring of each collimator used.

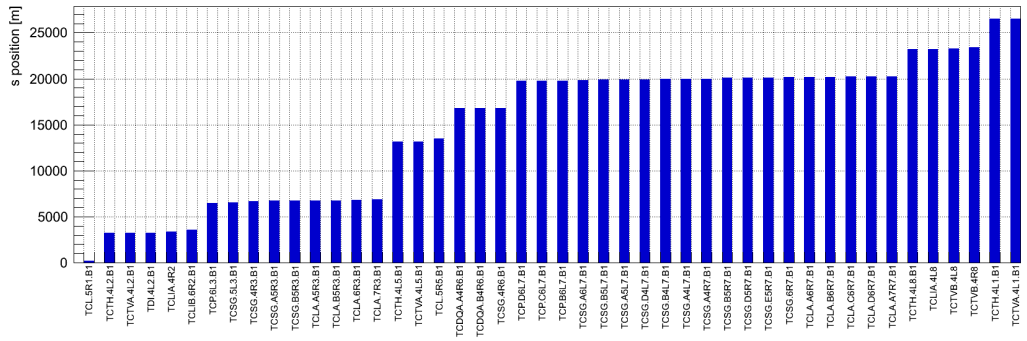

Figure 4.9. Collimator layout for Beam 1 4 TeV.

4.5.2 Distribution of the generated beam halo

SixTrack performs the tracking for several types of halo distributions (see section 4.3.3).The halo type selected in the fort.3 file is generated at IP1 and the spatial coordinates and angle of the distribution are contained in the output file called *dist0.dat*. Fig.4.10a illustrates the circular halo crown and the Gaussian cut at $3\,\sigma$ in the other plane, for Beam 1 at 7 TeV. In particular, are represented the phase spaces $x - x'$ and $y - y'$ with the x' and y' projections. The spatial coordinates and the angles are normalized to the $\sigma_{x,y}$ and $\sigma'_{x,y}$ calculated by using Eq.2.18 and Eq.2.19 respectively. In this case the β-function at IP1 is $\beta = \beta^* = 0.55\,\text{m}$. Fig.4.10b shows

the transverse halo distribution in the $x-y$ plane and the projections in x and y directions. The transverse coordinates are normalized to the $\sigma_{x,y}$ at IP1 as above.

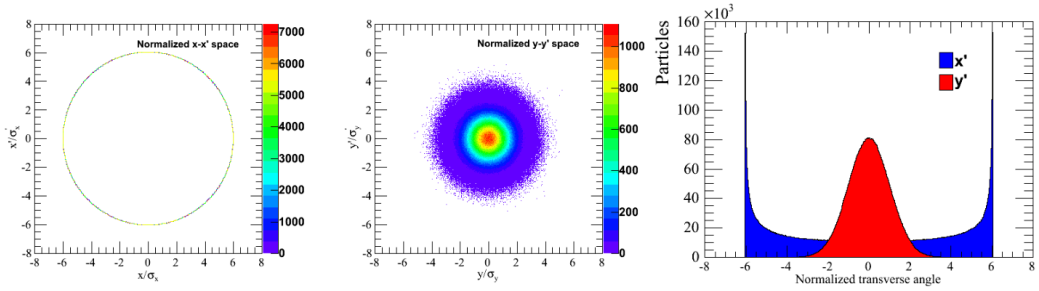

(a) Halo generated in the x-x' and y-y' spaces with x' and y' projections.

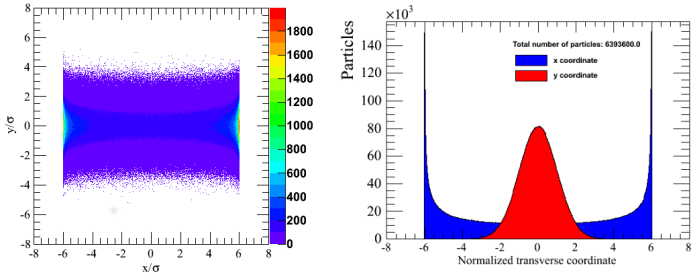

(b) Transverse distribution of the halo generate and projections in x and y directions.

Figure 4.10. Particle distribution in different spaces: horizontal halo in the $x-y$ plane with annular distribution in the $x-x'$ phase space and Gaussian distribution in the $y-y'$ phase.

4.5.3 Distribution of impacts at primary collimators

The reference plots that show the impacts at the collimator have been made for two different cases:

- first impacts of the halo particles at the primary collimators
- all impacts of the protons at the different collimators.

The halo particles hit the collimator with a certain impact parameter b, defined as the transverse offset between the jaw surface and the impact point. It is a positive value, typically in the range of 0<b<100 µm at the first impact. By using the information contained in the First_impacts.dat file, such as the impact parameters and the ingoing coordinates at the collimator, is possible to draw the plot in Fig.4.11. It shows, for the horizontal halo case (Beam 1 at 7 TeV), the transverse distribution of the first impacts on the primary collimators. In this case, the x position is always positive, because it represents the impact parameter on the collimator jaw. The x and y coordinates are normalized by using Eq.2.18 and Eq.2.19 with the γ and β values at primary collimator locations. Because the halo generated is in the horizontal plane, there is not any hits on the vertical primary collimator, however some of the halo particles hit the corner side of the skew collimator. The impacts shape on the skew primary collimator is geometrical explained in the Fig.4.11c.

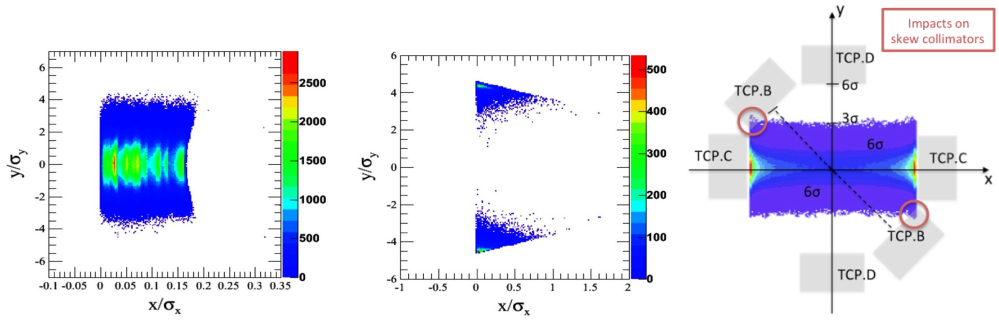

(a) Horizontal TCP (b) Skew TCP (c) Geometrical representation

Figure 4.11. Transverse distribution of the first impacts on the primary collimators.

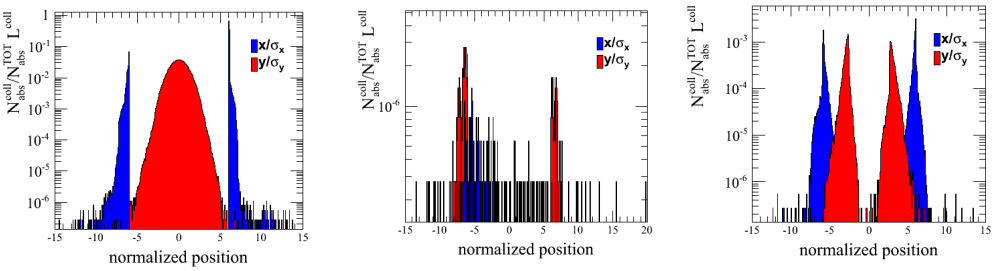

(a) Horizontal TCP (b) Vertical TCP (c) Skew TCP

Figure 4.12. Transverse distribution projections of the impacts on the primary collimators.

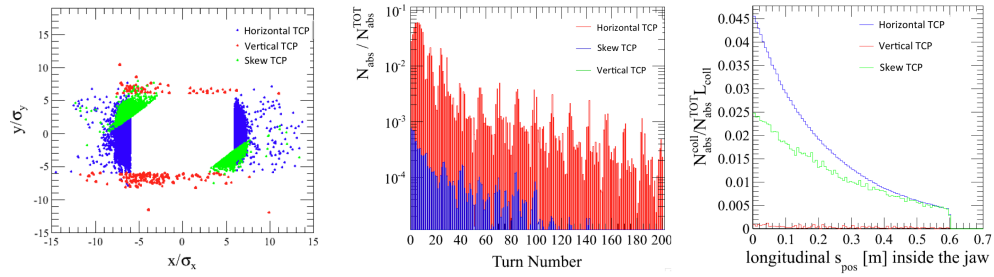

(a) Impacts distribution (b) Impacts at each turn (c) Impacts along s_{pos}

Figure 4.13. All impacts plots.

Up to now we show the distributions of the first impacts. However, particles can hit several collimators before being absorbed or lost in the aperture. Fig.4.13a shows all the impacts at the three primary collimators in IR7, in red for the vertical plane and blue for the horizontal plane.The difference is now that particles scattered in the horizontal or skew collimator can reach the vertical collimator and thus we see the impacts in Fig.7.11b The number of particle absorbed at each collimator N_{abs}^{coll} is normalized to the collimator length L^{coll} and to the total number of particles absorbed N_{abs}^{TOT}. Fig.4.13a shows the superposition of all the impacts at the three TCP in IR7. The different colors represent the three primary collimators: horizontal (blue), vertical (red) and skew (green). The impacts_real.dat file contains also information about the turn during which the proton is lost at the collimator. Fig.4.13b shows the number of particle absorbed at the primary collimators per turn. The impacts along the longitudinal s position is shown in Fig.4.13c.

4.5.4 Distribution of impacts at TCTs and dump protection

The experimental insertions host horizontal (TCTH) and vertical (TCTV) tertiary collimators to provide protection to the triplet magnets. The triplets are assembly of three quadrupole magnets used to reduce the optical β-function at the collision points. The LHC machine has triplets in IR1, IR2, IR5 and IR8 insertions.
The tertiary collimators are two-sided collimators formed by 1 m copper jaws with a tungsten inlay. For 7 TeV simulations, with β^* of 0.55 m, they are set at $8.3\,\sigma$ in IR1 and IR5, while more relaxed gaps at $25\,\sigma$ are used for the TCTs in IR2 and IR8, with β^* of 10 m.
The dump system is installed in the extraction region in IR6, where the TCDQs absorb the beam swept over the machine aperture in order to avoid radiation damage. One horizontal TCSG collimator is located next to TCDQs to provide further protection to the downstream machine elements. In order to check and verify the simulation results, Fig.4.14 shows the number of impacts on tertiary collimators in IP1, IP2, IP5, IP8 and in the dump protection system in IP6. The losses are normalized to the total number of particles absorbed for Beam 1 horizontal halo case at 7 TeV.

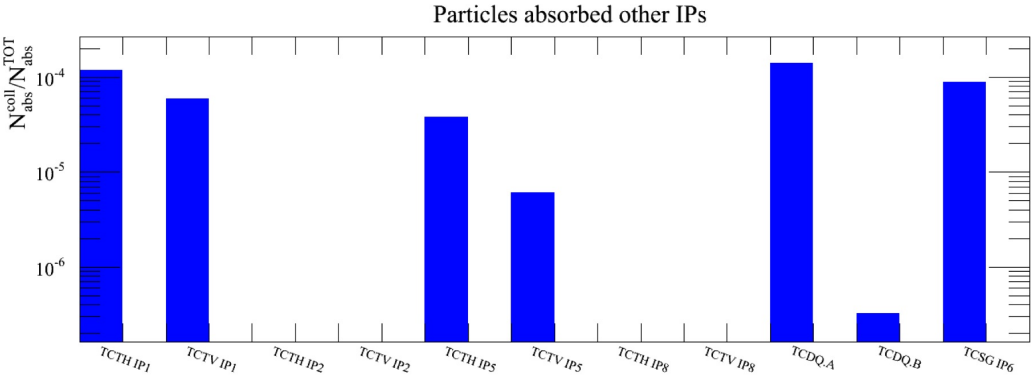

Figure 4.14. Number of absorbed particles at different IP collimators, normalized to the total number of absorbed particles.

4.5.5 Particle lost at aperture in the Dispersion Suppression region at IR7

The IR7 insertion contains the betatron cleaning system where the particles with large betatron amplitude in both vertical and horizontal directions are scattered by the primary collimator jaws and absorbed by the secondary collimators. The most critical area in terms of losses is the region downstream of IP7 (for Beam 1) that is called the Dispersion Suppressor (DS). This region consists in a lattice cells with one dipole magnet missing, reducing so the dispersion function. The dispersion suppression regions are located at the end of each LHC arc and the tunnel geometry determines their lengths. A plot that shows the transverse distribution of the losses in the DS region, in the range of 20270-20350 m, with the projections in the x and y directions, is shown in Fig.4.15. The curved shape profile shows the simulated beam pipe.

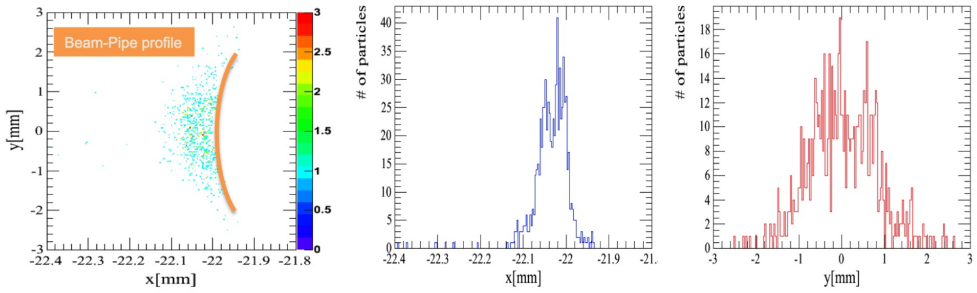

(a) Transverse distribution **(b)** Transverse distribution projections

Figure 4.15. Distribution of the particle lost in the aperture of the DS region in IR7.

4.5.6 Standard loss maps and cleaning efficiency

The SixTrack simulation results allow to draw detailed maps of loss location along the whole LHC ring, for different optics and collimator settings, by using specific SixTrack outputs file. In particular, reading the `impacts_real.dat` is possible to calculate the particles absorbed at the collimators, while by reading the `LPI_PartLost.dat` is possible to compute the number of particles lost at the machine apertures.
These detailed maps are called *beam loss maps* and show the local cleaning inefficiency η_c, defined in Eq.2.48, along the length of the machine with a Δs=10 cm resolution. An example of a loss map is shown in Fig.4.16 for Beam 1 horizontal halo case at 7 TeV. The red lines, called *warm losses*, identify beam losses in normal conducting magnets that work at room-temperature. The blue lines represent the *cold losses* that show the location of proton losses in superconducting magnets. In order to prevent the quench of the superconducting magnets, the cold losses must not exceed the quench limit defined in Eq.2.49. The cleaning inefficiency at the collimators are represented by the black lines. In the case of collimators the resolution Δs in the cleaning inefficiency definition is substituted by the collimator jaw active length. For this reason at the primary collimators, with a 0.6 m jaw length, the cleaning inefficiency can be greater than one. Fig.4.16b shows a zoom of the betatron

cleaning insertion (IR7) where are located the Q8, Q9, Q10 and Q11 superconducting magnets.

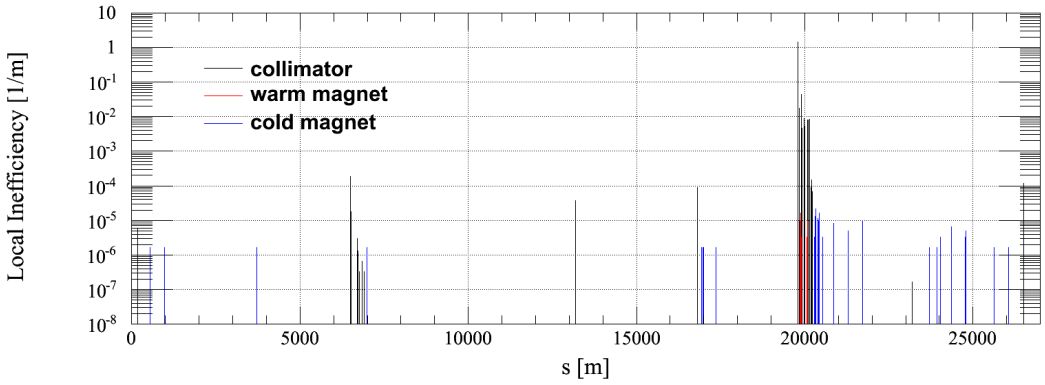

(a) Full ring loss map

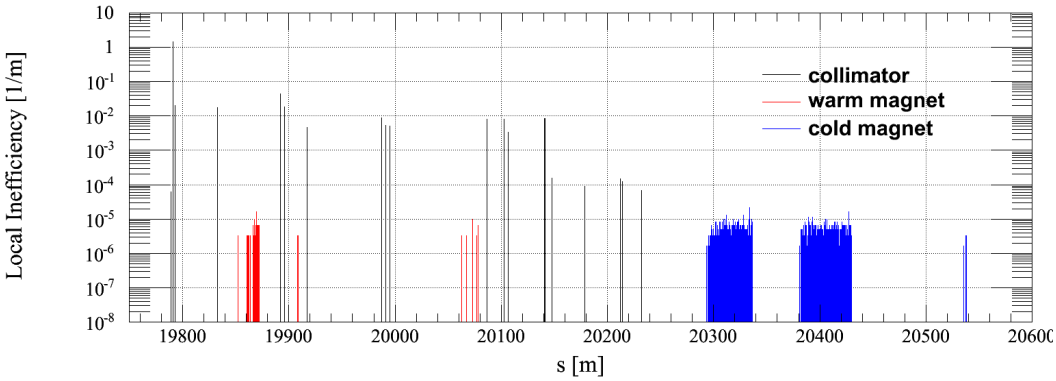

(b) Loss map at the betratron cleaning insertion IR7

Figure 4.16. Simulated beam loss map at 7 TeV for Beam 1 in the horizontal plane. Simulation done using the 7 TeV collimator settings defined in Table 3.3.

Chapter 5

Improved physics model for SixTrack scattering routine

The high energy proton beams of the LHC interact with the matter of the collimator jaws through scattering mechanisms due to interactions of the incoming protons with either the electro-magnetic field of the atoms or the strong potential of the nucleus [27]. The scattering mechanisms are modeled and implemented in SixTrack with a Monte-Carlo code deriving from the K2 scattering routine. The K2 is a software package, developed during the 1990's by T.Tranker and J.B Jeanneret [21], for setting up and testing collimation systems in circular accelerators for proton beams.
In this code we classify the interactions between a high energy proton and the matter as follow:

- *Nuclear interaction*, with a finite cross sections:
  - inelastic scattering with the nucleus of total cross section σ_{pN}^{in}
  - elastic scattering with the nucleus of total cross section σ_{pN}^{el}
  - scattering with whole nucleus of total cross section σ_{pN}^{tot}
  - proton-nucleon elastic scattering of total cross section σ_{pp}^{el}
  - single diffractive scattering of total cross section σ_{pp}^{SD}

  The inelastic interactions produce a variety of lower energy particles that are lost within the nearest collimation section. Instead, the other interactions leave the energy of the particle in a range that is well accepted by the optics of the accelerator.
- *Coulomb scattering*, a stochastic process that occurs when the incoming particle has a large impact parameter. The incoming particle feels the long range overlapping fields of all ions or molecules and is kicked by small angles. Only if the particle gets closer to an ion, it is scattered with a substantial kick described by the Rutherford scattering formula. Thus the Coulomb scattering can be described in two different ways:
  - Large angle Rutherford scattering with a finite cross section, σ_{Rth}, for particles that have small impact parameter on the ions and

  - Multiple Coulomb scattering (mCs) described as a stochastic process for particles that have a long range interaction

.

- *Ionization:* the electrons of the atomic shells are kicked off because of the energy released by the passing particle. The particle loses a small amount of energy proportional to the length of the traversed matter.
- *Hard electro-magnetic processes like pair production:* these processes are marginal below 10 TeV and are not implemented in the Monte-Carlo code.

The cross sections of the SixTrack scattering routine have been updated taking into account recent experimental data. In addition, other improvements were carried out in order to describe better the interaction processes. All of them will be presented in the next sections with a brief theoretical description followed by the changes carried out on the routine.

5.1 SixTrack scattering routine

The scattering routine of SixTrack is divided in different subroutines, each one with a specific purpose. An overview of the calling sequence between the subroutines is shown in Fig.5.1. The starting point to simulate the proton scattering within the collimator jaw, is established only whether the proton hits the collimator. This is determined in the subroutine called `Collimate2`. Considering now the x-coordinate as: $x = |x - \text{half-gap}_{coll}|$ in the collimator frame (see Fig.5.2) a particle that has $x \geq 0$ surely hits the collimator, that for definition is at $x \geq 0$, in this case the proton sees all the jaw length (see Fig.5.2 (1)). When $x < 0$ and $x' \leq 0$ the proton doesn't hit the collimator while in case of $x' > 0$ and $x < 0$ the proton hits the edge of the jaw and the longitudinal s position of entrance must be calculated.

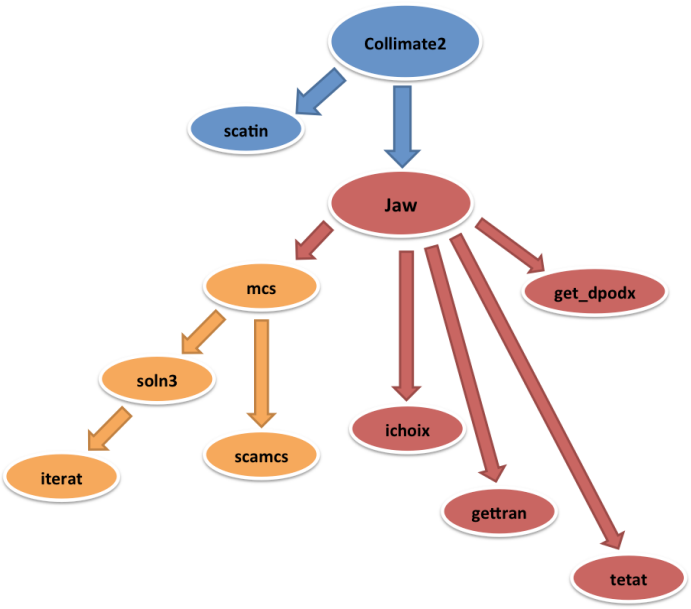

Figure 5.1. Scheme of the calls between different subroutines in SixTrack scattering routine.

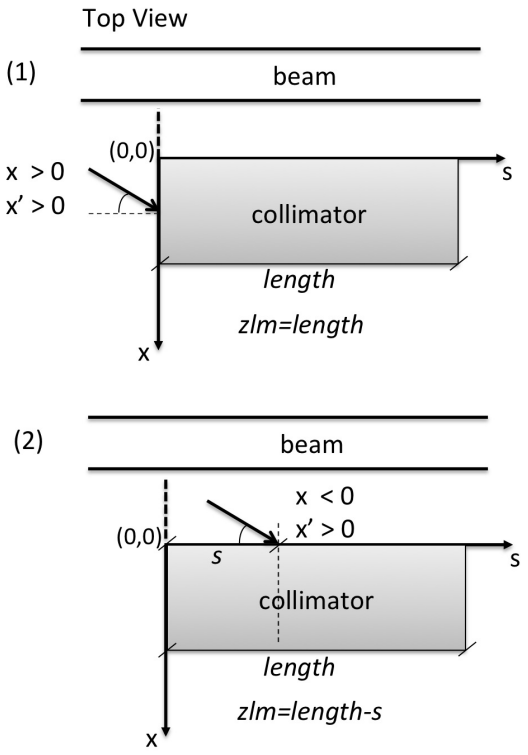

Figure 5.2. Representation of particle position close to collimator jaw.

In the first case Fig.5.2 (1) the impacting particle sees a collimator of full length L. However, in the second case, Fig.5.2 (2) the particle sees only a section of the collimator length $(L - \frac{x}{x'})$. If s results to be greater than the collimator length it means that the proton is passing above the edge of the collimator.
In the subroutine called `scatin` the cross sections are initialized in two-dimensional arrays that contain both the interaction type and the collimator material (Beryllium, Aluminum, Copper, Tungsten, Lead, Carbon and special carbon fibers).
The interactions between the proton and the matter of jaw are implemented in the main subroutine called `jaw`. In this subroutine the interaction length is randomly generated several times, until the proton is absorbed or leaves the collimator jaw. The proton travels the entire interaction length doing multiple scattering and losing energy by ionization. The rms angle kick due to multiple Coulomb scattering is computed by the subroutine `mcs` and the energy lost per unit length, dp/dx, is calculated by the function `get_dpodx` that has been implemented in the new SixTrack version to calculate the Bethe-Bloch equation. At the end of the path, the function `ichoix` chooses the kind of interaction occurred by using a cumulative probability evaluated from the cross section value. Afterwards, the function `gettran` generates randomly the *Mandelstam* variable $t = (p\theta)^2$ for the selected process and from it the subroutine `tetat` calculates the angle θ and its projections in the x direction and y directions, in order to apply the angle changes. If an inelastic process occurs, the particle is lost at the collimator, otherwise another Monte-Carlo

interaction length is generated and the proton continues to travel along the jaw. The method is iterated until the interaction length generated is greater than the remaining length of the collimator, the proton does multiple Coulomb scattering until the end of the jaw: this is the last step of the scattering routine.

5.2 Electromagnetic processes

A charged heavy particle, as the proton, moving inside matter loses energy mainly due to the excitation and ionization of the medium atoms [27, 28]. This type of interactions are processes mediated by the electromagnetic field associated to the incoming charged particle and the medium targets. In addition to the energy released electromagnetically, there are effects that occur for approaching distances smaller than the atomic radius. In this case the transferred momentum is usually very small respect to the particle momentum. The charged particle traversing the medium undergoes a lot of deflections of its trajectory due to the elastic scattering with the nuclei, this process is known as multiple Coulomb scattering.

5.2.1 Ionization

For relativistic charged particles, other than electrons, and neglecting radiative effects the mean rate of energy lost by ionization is given by the Bethe-Bloch formula (1930)[27, 29]:

$$-\frac{dE}{dx} = Kz^2\frac{Z}{A}\frac{1}{\beta^2}\left[\frac{1}{2}ln\frac{2m_ec^2\beta^2\gamma^2T_{max}}{I^2} - \beta^2 - \frac{\delta}{2}\right] \tag{5.1}$$

where m_e is the electron mass, Z and A are the atomic number and the atomic mass of the medium. The quantities β and γ are the kinematic variables. The mean excitation energy I is an empirical value given by $(10 \pm 1\,eV) \cdot Z$ for elements heavier than the oxygen. T_{max} is the maximum kinetic energy that can be imparted to a free electron in a single collision. The last term in Eq.5.1, $\delta/2$ is the so called density effect correction.

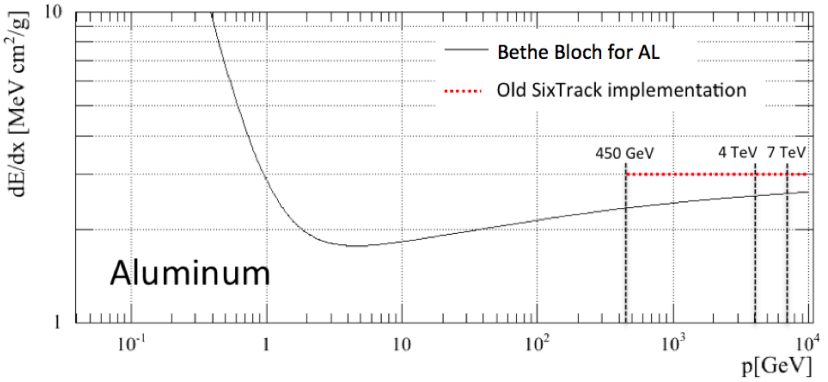

Figure 5.3. Implemented Bethe-Bloch formula in the case of Aluminum compared with the previous SixTrack reference value used for simulations.

The new function `get_dpodx` has been implemented in order to calculate the Bethe-Bloch equation 5.1. In the previous version, the values of energy lost by ionization were taken at the same reference energy E_{ref}=450 GeV for different materials. To better evaluate the energy loss rate dE/dx, the function 5.1 is now computed for protons of any given energy. This evaluation is performed after a conversion to metric units by using the material density. Fig.5.3 shows the Aluminum energy lost by ionization calculated with the function `get_dpodx` in SixTrack for any given energy. The previous reference value at E_{ref}=450 GeV used for the simulations at any energy is also shown with the dashed red line. Table 5.1 quantifies the differences between the two implementations. In the first column are shown the predicted energy lost for different materials with the old routine. Then the next column shows the result of the new implementation using the complete Bethe-Bloch equation. The last column shows the relative difference. Notice that in the previous routine the energy loss was always overestimated. The smaller difference is for Aluminum, 13%, and the largest for Tungsten of up to 30%.

5.2.2 Multiple Coulomb Scattering

A charged particle passing through a thickness of material is subject to a large number of small angle deflections all along its trajectory in the medium. These deflections have a stochastic characterization and are due to Coulomb scattering with nuclei, so called multiple Coulomb scattering (mCs). The Coulomb scattering distribution is well represented by the Moliere's theory [30] that deals with small scattering angles.
The distribution function $f(x, x', s)$ for the scattered particle obeys the Fokker-Plank equation, derived and solved by Fermi [31] [32]:

$$\partial_s f + x'\partial_x f = \frac{\theta_0^2}{2}\partial_{x'}\partial_{x'} f \tag{5.2}$$

f represents the probability for the charged particle to be in a certain position x in the transverse direction with an angular deflection x' after traversing a thickness s of material. θ_0 is the rms angular kick received by the particle in the x direction when it traverses a unit of length of matter:

$$\theta_0 = \frac{13.6MeV}{\beta cp} z \frac{1}{\sqrt{\chi_0}} \tag{5.3}$$

Material	dE/dx [GeV/m] at $E = 450$ GeV	dE/dx [GeV/m] at $E = 7$ TeV	Relative difference [%]
Beryllium (Be)	0.55	0.45	18
Aluminum (Al)	0.81	0.71	13
Copper (Cu)	2.69	2.15	20
Tungsten (W)	5.79	4.0	30
Lead (Pb)	3.4	2.36	30
Carbon (C)	0.75	0.62	18

Table 5.1. Loss energy rate for $E_{ref} = 450$ GeV previously tabulated in SixTrack and new values calculated with the new Bethe-Bloch function at $E = 7$ TeV.

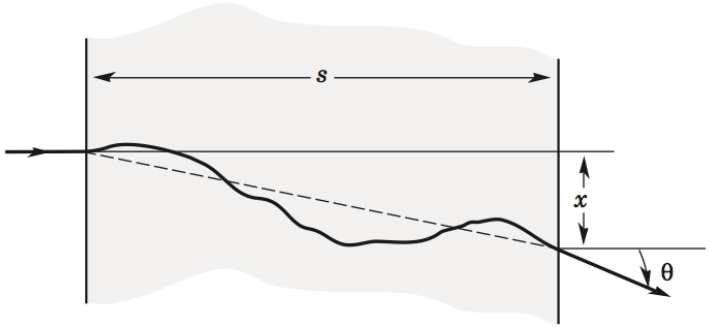

Figure 5.4. Schematic view of MCS in one plane [27].

βc is the velocity of the incoming proton, z the electronic charge of the beam, p the momentum and χ_0 the radiation length of the traversed material. The rms angle after traversing a length s of matter is:

$$\theta(s) = \theta_0\sqrt{s}. \tag{5.4}$$

For a point-like initial distribution represented by:

$$f(s=0,x,x') = \delta(x-x_0)\delta(x'-x'_0), \tag{5.5}$$

the solution of (5.2) is the Fermi distribution:

$$f(s,x,x') = \frac{\sqrt{3}}{\pi\theta_0^2 s^2}\cdot exp\left[-\frac{6}{\theta_0^2 s^3}\left(x-x_0-sx'_0-\frac{s}{2}(x'-x'_0)^2\right)\right]\cdot exp\left[-\frac{1}{2\theta_0^2 s(x-x'_0)^2}\right] \tag{5.6}$$

The equation (5.3) fails to describe multiple Coulomb scattering when the processes is no more stochastic, as in the case of short length of traversed matter, moreover if the incoming proton has a small impact parameter on the nucleus, the Rutherford scattering occurs and the scattering angles are greater than a few of θ_0.
Measures on the rms kick lead to the following correct formula:

$$\theta_0 = \frac{13.6MeV}{\beta cp} z\frac{1}{\sqrt{\chi_0}}[1+0.038\ln(s/\chi_0)] \tag{5.7}$$

which differs from the previous one by the logarithmic term. The rms width is a Gaussian approximation for the central 98% of the projected angular distribution. For Monte-Carlo generation of a joint of (x,x') is convenient to work with two independent Gaussian random variables (z_1,z_2) with mean zero and variance one, and then set:

$$\begin{aligned} x &= x_0 + sx'_0 + z_1 s\theta(s)\frac{(1-\rho_{xx'}^2)^2}{\sqrt{3}} + z_2\rho_{xx}s\frac{\theta(s)}{\sqrt{3}} = \\ &= x_0 + sx'_0 + z_1 s\theta(s)(\frac{z_1}{\sqrt{12}}+\frac{z_2}{2}) \end{aligned} \tag{5.8}$$

$$x' = x'_0 + \theta(s)z_2 \tag{5.9}$$

where has been used the correlation factor $\rho_{xx'} = \sqrt{3}/2$ obtained from the diffusion theory. This method is used in the Monte-Carlo scattering code to simulate the multiple Coulomb process within the jaw.
In the new SixTrack version the mCs Eq.5.3 has been replaced by the Eq.5.7 containing the logarithmic part. SixTrack simulations for a horizontal halo of 7 TeV for different materials of the collimator jaw were carried out to evaluate the difference with respect to the previous rms angle. In particular, these simulations were performed considering the passage of protons through a collimator jaw of 0.6 m length. This analysis was performed using the pencil-beam configuration for Beam 1. In the selected configuration all the impacting particles have the same energy and the same angle x'=0 rad. They are centered on the collimator jaw with an impact parameter b=10 mm. In Fig.5.5a the $\theta^{rms}(s)$ angles in the $s-x$ plane calculated by the Eq.5.3 are shown. The angle is plotted as a function of the s position inside the collimator jaw for different materials. The dashed lines represent the simulations performed without the logarithmic term (old SixTrack), while the solid lines includes the logarithmic correction (new SixTrack). In the case of light materials, like Carbon, Beryllium, and Aluminum the difference between the two cases can be neglected, while for the heavy materials as Lead, Copper and Tungsten the differences become not negligible and can arrive up to 20%. This is shown in Fig.5.5b which shows the relative variation of the θ_x^{rms} angle.
The angle distribution of the protons at the end of the collimator jaw is shown in Fig.5.6. The black line represents the angle distribution from simulations performed without the logarithmic term. The wider red line describes the angle distribution after the correction. A larger spread of the protons outside the collimator can be seen in the latter case. These simulations are carried out for a 60 cm horizontal primary collimator of Carbon. The relative difference between the rms of the two distribution is about 17% for Carbon.

5.3 Nuclear Interactions

The incoming protons discretely interact with the nuclei of the material jaw. Each scattering process is characterized by a finite cross section σ that gives the probability for the process to occur. To specify the cross section and the differential cross sections, related to the probability to find the scattered proton at a given polar angle θ or at a given momentum, the Lorentz-invariant Mandelstam variables are used. Those variables for high energy protons are:

- the transverse momentum transferrer $t = (p\theta)^2$
- the centre of mass energy squared $s \approx 2m_p p$

where m_p is the proton mass.
The total proton-nucleus cross section σ_{pN}^{tot} is given by the sum of different contributions as follow [28]:

$$\sigma_{pN}^{tot} = \sigma_{pN}^{in} + \sigma_{pN}^{el} + \sigma_{pN}^{q-el}. \tag{5.10}$$

The first term is the inelastic cross section and it gives the probability for the proton to be absorbed by the medium, σ_{pN}^{el} refers to coherent elastic scattering with

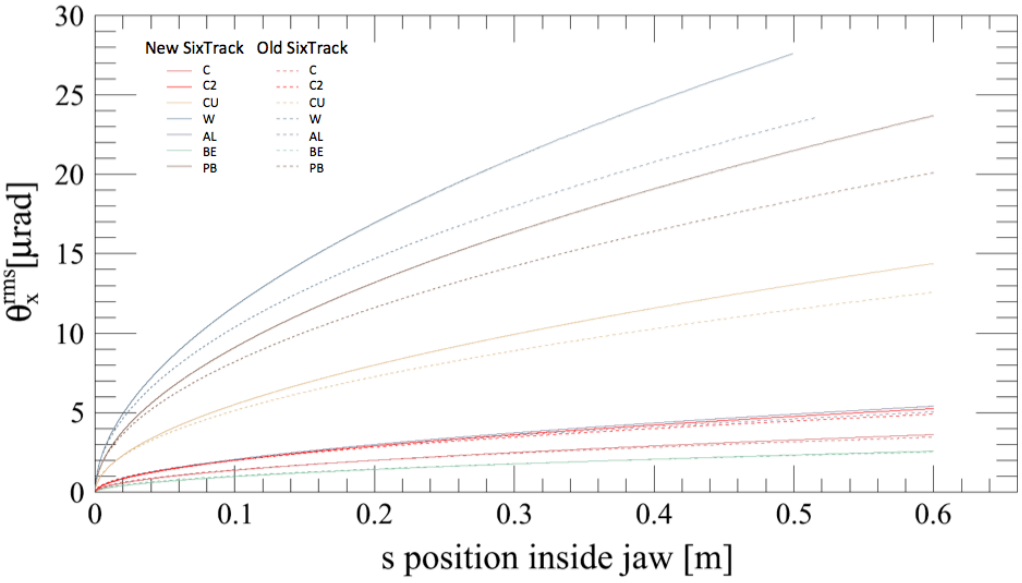

(a) Multiple Coulomb scattering angle (rms) in the s-x plane for several material calculated by using the mCs formula with and without the logarithmic term.

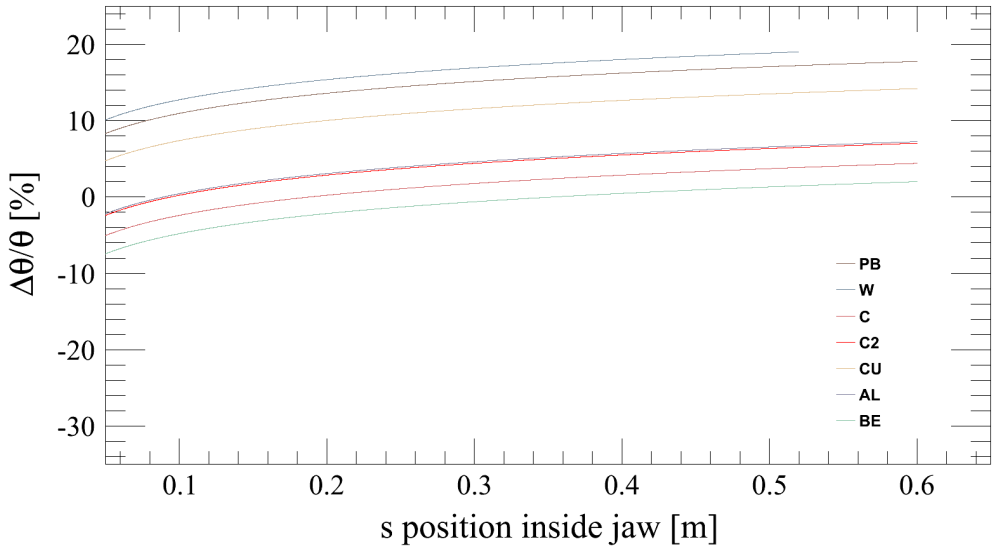

(b) Variation of the mCs rms angle with respect to the formula without the logarithmic part for different materials.

Figure 5.5. Multiple Coulomb scattering angle (rms) in the $(s - x)$ plane for different path with the collimator jaw.

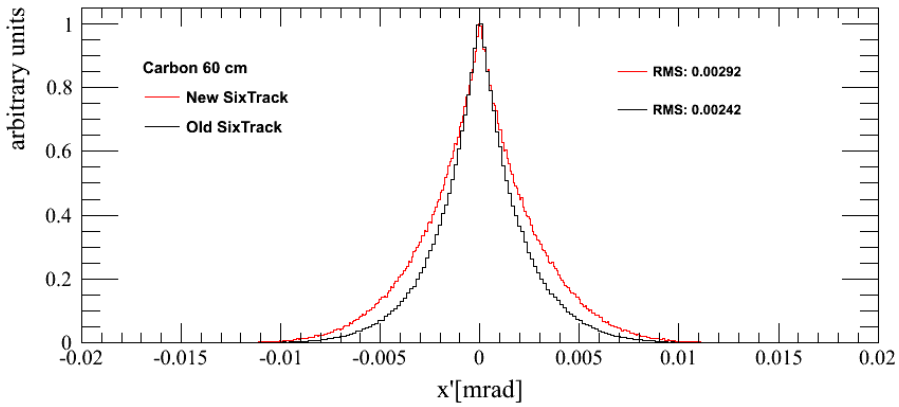

Figure 5.6. Distribution in x' of the particles at the end of the horizontal primary collimator before (blue line) and after (red line) the logarithmic correction in the multiple Coulomb scattering formula.

the whole nucleus and σ_{pN}^{q-el} refers to the quasi-elastic incoherent processes with individual nucleons. For the process σ_{pN}^{q-el}, the incoming proton remains the same but the nucleus might be destroyed. The incoherent scattering with the nucleons, elastic or quasi-elastic, can be assigned to a limited number of the nucleons confined in the nucleus surface given by $n_{eff} = 1.6\,A^{1/3}$ [31][33], where A is the atomic mass of the nucleus. The two contributions considered for the incoherent scattering, can be expressed as:

$$\begin{aligned} \sigma_{pn}^{el} &= n_{eff}(A)\sigma_{pp}^{el} \\ \sigma_{pn}^{SD} &= n_{eff}(A)\sigma_{pp}^{SD} \end{aligned} \tag{5.11}$$

where σ_{pn}^{el} refers to the elastic scattering between the incoming proton and one of the nucleons, σ_{pn}^{SD} refers to the single diffraction dissociation. All the nuclear interactions will be describe in details in the next sections.
The total cross section σ_{pN}^{tot} is related to the mean free path between successive collision with nuclei by the following expression:

$$\lambda_{tot} = \frac{A}{N_A \rho \sigma_{pN}^{tot}} \sim \frac{1}{\sigma_{pN}^{tot}} \tag{5.12}$$

where N_A is the Avogadro number and ρ the medium density.
In terms of Monte-Carlo simulations the distance between two nuclear interactions is a random quantity weighted by an exponential and is given by:

$$\Delta s = -\lambda_{tot} \ln u \tag{5.13}$$

where u is a uniformly distributed number between zero and one. This number represents the probability for any given interaction to occur when the proton travels the Δs distance within the collimator. Fig.5.7 shows the generated mean free path distribution divided by the radiation length χ_0 of the collimator material selected.

5.3.1 Proton-nucleon nuclear scattering

The beam protons are diffused by the nucleons of the matter nuclei by elastic and single diffractive scattering. The experimental data are more abundant and exhaustive for the protons than the neutrons. Since the proton-neutron nuclear scattering is consider equal to the proton-proton scattering, Therefore, the proton-proton quantities will be also used for the proton-neutron case.

Proton-proton elastic scattering

In the previous version of the scattering routine the proton-proton elastic cross section was calculated using a linear fit from experimental data up to $2.08 \cdot 10^3$ GeV center of mass energy.However, the TOTEM collaboration has recently measured the proton-proton elastic cross section up to $\sqrt{s} = 8$ TeV [34]. The measurements of the proton-proton elastic cross section, proton-proton total cross section and proton-proton inelastic cross section are shown in Fig.5.8 [34]. The new measurements of the total and elastic proton-proton cross sections at $\sqrt{s} = 8$ TeV center-of-mass energy bring the opportunity to perform better fits to the data and therefore improve the prediction at intermediated energies. In the new SixTrack version has been implemented the latest fit from TOTEM measurements for the elastic proton-proton cross section shown in Fig.5.8:

$$\sigma_{pp}^{el} = 11.7 - 1.59 \ln s + 0.134 \ln^2 s. \tag{5.14}$$

Notice that since we are simulating high energetic protons into a fixed target (the collimator jaw), the center-of-mass energy under study is about $\sqrt{s} = 114$ GeV for 7 TeV protons. To determine the momentum change and the angle deflection of the scattered proton the differential cross section has to be known, in first approximation can be expressed as:

$$\frac{d\sigma}{dt} = ae^{-b(t,s)t} \tag{5.15}$$

where $b(t, s)$ is the elastic slope factor. In the practical t-range considered at the energy of LHC, the slope factor depends weakly on t, thus can be considered $b(s, t) \approx$

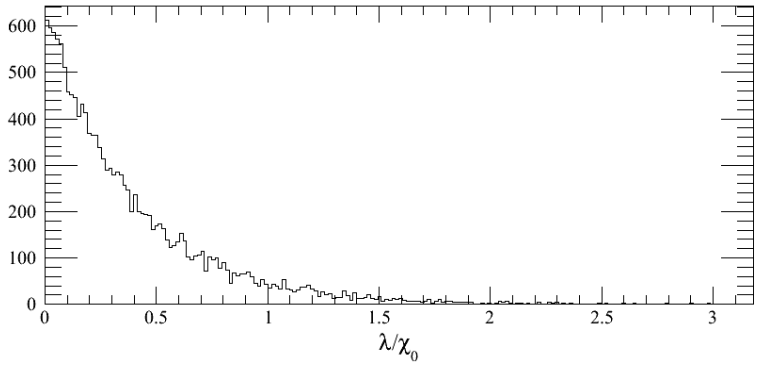

Figure 5.7. Distribution of the mean free path (λ) divided by the radiation length (χ_0) of the material chosen, Carbon for the present case.

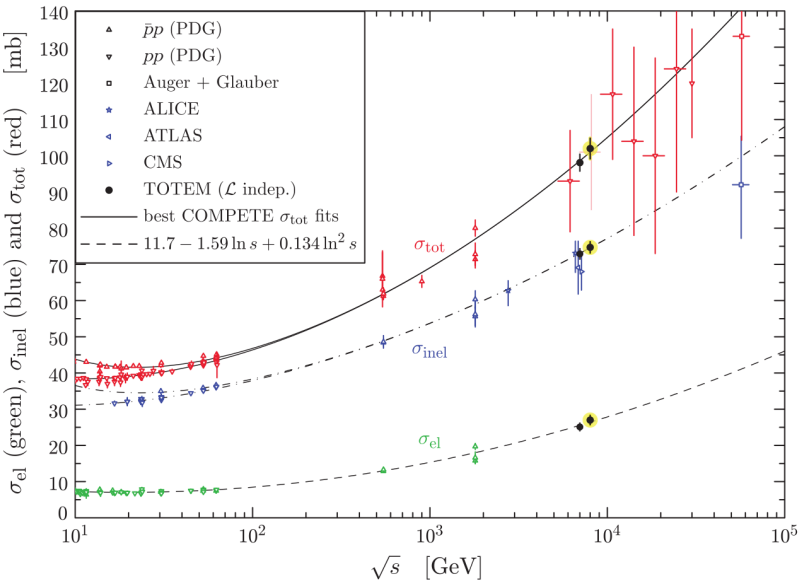

Figure 5.8. Elastic, inelastic and total cross sections from TOTEM Collaboration [34].

$b(s)$. In the previous scattering routine was used a parametrization extrapolated from several accelerator experimental data (ISR at CERN, TEVATRON at Fermilab, RHIC at BNL) for energies up to $\sqrt{s} = 200\,\text{GeV}$. A new parametrization has been implemented to extrapolate more accurately the slope parameter value up to LHC energies. Fig.5.9 shows the elastic proton-proton slope factors from several collaboration data at different center of mass energies[35] including the recent data from TOTEM at $\sqrt{s}$=7 TeV. The dashed blue line represents the fit used in the previous SixTrack version, the black solid line is the new parametrization implemented:

$$b_{pp} = 7.16 + 1.44 \ln \sqrt{s}. \tag{5.16}$$

At the LHC center of mass energy $\sqrt{s} = 114.6\,\text{GeV}$, the relative difference between the previous and the current fit is $\sim 2.5\%$, this value increases with the center of mass energy leading to a more realistic description of the proton-proton elastic scattering for proton beams of higher energy.

Single diffractive scattering

The single diffractive scattering (SD) is a low momentum transfer interaction where one of the protons is coherently excited into a high mass state M without quantum number exchange. This process is dominant within a range of excited masses M:

$$M_0^2 < M^2 < 0.15\,s \tag{5.17}$$

where the lower bound is $M_0 = (m_p + m_\pi) \approx 1\,\text{GeV/c}^2$ and $0.15\,s$ is the coherence limit above which the SD scattering does not occur anymore. The differential cross section can be parametrized, considering the range of $1 \leq M^2 \leq 0.15\,s$, by the

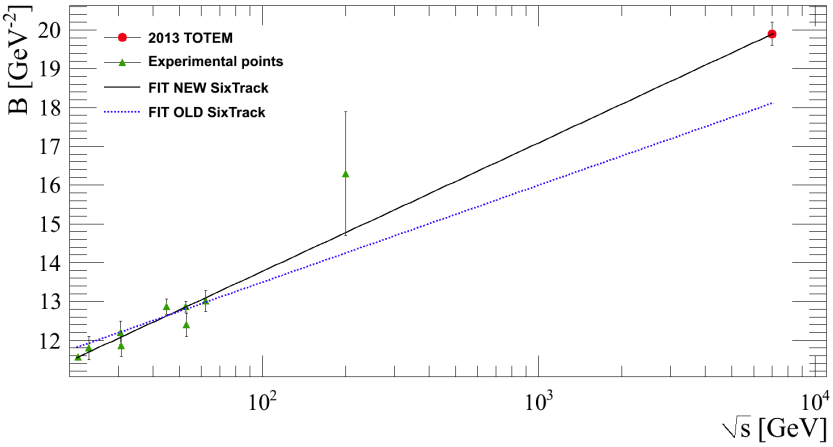

Figure 5.9. The slope parameter for pp and $p\bar{p}$ elastic scattering. Data from different collaboration including the recent TOTEM measurement [34].

following expression [36]:

$$\frac{d\sigma^2}{dtdM^2} = \frac{Ab(M)e^{-b(M)}}{M^2} \tag{5.18}$$

where $b(M)$ is the slope factor and the constant $A = 0.68\,\text{mb}$. Outside this range the cross section is approximately zero.

A new model for the total single diffractive cross section has been considered to update the previous one based on the standard Pomeron flux [36]. The measurement of the $p\bar{p}$ single diffraction dissociation cross section at the $Sp\bar{p}S$ Collider [37] and at Tevatron [38, 39] led to a phenomenological renormalization scheme for the hadronic diffraction [40]. The new model unitarizes the Pomeron flux factor in the triple-Pomeron amplitude preserving the M^2 and t dependence. Fig.5.10 shows the total pp and $p\bar{p}$ single diffractive cross sections data for $\xi < 0.05$ compared to the predictions based on the standard and renormalized pomeron flux (from [40]). The quantity $\xi \approx M^2/s$ is the incident proton momentum fraction carried by the Pomeron. Fig.5.11 shows the triple-Pomeron Feynman diagram for single diffraction where $g(t)$ is the triple-Pomeron ($\mathbb{P}\mathbb{P}\mathbb{P}$)coupling.

Above $\sqrt{s} = 22\,\text{GeV}$, where the pomeron flux factor integral becomes unitary, a linear logarithmic expression has been used in the range $22 < \sqrt{s} < 10000\,\text{GeV}$ to obtain the following parameterization for the total single diffractive cross section (in mb):

$$\sigma_{pp}^{SD}(s) = 4.3 + 0.3 \ln s. \tag{5.19}$$

The single diffractive cross section value extrapolated at LHC energies is predicted by $\sigma_{sd}^{p\bar{p}}|_{\xi<0.05} = 7.15\,\text{mb}$ at $\sqrt{s} = 114.6\,\text{GeV}$ for a 7 TeV incident proton on a rest target.

The slope parameter b cannot be precisely predicted hence an approximated fit, adjusted on measured data, is used:

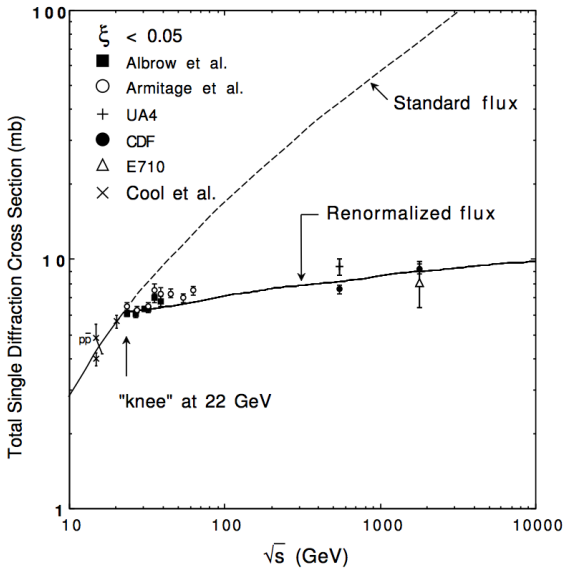

Figure 5.10. Total pp and $p\bar{p}$ single diffractive cross section data for $\xi < 0.05$ compared with prediction based on the standard and renormalized pomeron flux [40].

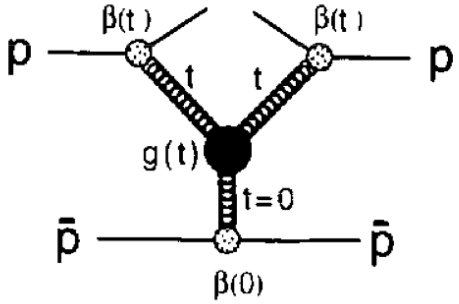

Figure 5.11. Triple-pomeron Feynman diagram for single diffraction [40].

$$b = 2b_{el} \qquad M^2 < 2GeV \tag{5.20}$$

$$b = \frac{1}{36}(106 - 17M^2)b_{el} \qquad 2 < M^2 < 5GeV \tag{5.21}$$

$$b = \frac{7}{12}b_{el} \qquad M^2 > 5GeV. \tag{5.22}$$

Fig. 5.12 shows the total single diffractive cross section obtained using the previous parameterization (blue line) versus the updated one given by Eq.5.19 (red line). In Table 5.2 the single diffractive cross section values, for different beam energies, calculated by the previous parameterization and the updated one are listed with the relative variations. For a 7 TeV proton beam the relative difference is $\sim 40\%$, so the previous SixTrack scattering routine was underestimating the single diffractive contribution. Further simulations to investigate the effect caused by the high cross section difference at the injection energy of 450 TeV should be performed.

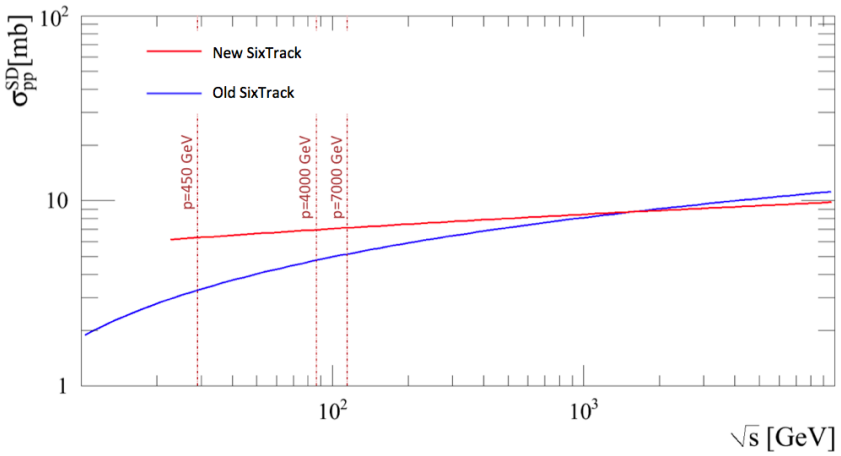

Figure 5.12. Total single diffractive cross section with the previous parameterization (blue line) and the new one calculated by using the Eq.5.19 (red line)

Table 5.2. Total single diffractive cross section values calculated with the previous parameterization and the new one.

Momentum p [GeV]	OLD σ_{SD} [mb]	NEW σ_{SD} [mb]	Variation %
450	3.292	6.321	90
4000	4.778	6.977	50
7000	5.158	7.145	40

Proton-proton total cross section

The proton-proton total cross section has been updated by using a parametrization from the COMPETE collaboration data fit containing the measured TOTEM proton-proton total cross section at $\sqrt{s} = 7\,\text{TeV}$ [34]. The fit is shown in Fig.5.8 and it gives the following total cross section (expressed in mb) :

$$\sigma_{pp}^{tot} = 41 - 2.33 \ln s + 0.315 \ln^2 s. \tag{5.23}$$

In Table 5.3 the total proton-proton cross sections from the previous SixTrack implementation and the new one are presented for several beam energies. The cross sections vary little, the maximum variation is ≈1%.

Table 5.3. Total proton-proton cross sections from the previous SixTrack implementation and the updated one.

Momentum p [GeV]	σ_{pp}^{tot} old fit [mb]	σ_{pp}^{tot} new fit [mb]	Variation %
450	40.0	39.6	1
4000	45.4	45.3	0.2
7000	46.9	47.2	0.7

5.3.2 Proton-nucleus scattering

The beam halo incoming protons are diffracted by the nuclei of the jaw material. The particle can interact coherently with the whole nucleus or incoherently with a limited number of nucleons n_{eff} situated in the nucleus rim. The total proton-nucleus cross section is:

$$\sigma_{pN}^{tot} = \sigma_{pN}^{in} + \sigma_{pN}^{el} + \sigma_{pN}^{q-el}. \tag{5.24}$$

Proton-nucleus elastic scattering

The proton-nucleus elastic cross section is calculated by subtracting all the other contributions from the total cross section σ_{pN}^{tot}.
For the differential cross-section $d\sigma/dt$ the slope factor b_{pN} has been measured for hadron beams on various target materials at different energies [41]. The measured values are reported in Fig.5.13. The A-dependance of the elastic pN scattering slope factor can be derived from a linear fit on the data:

$$b_{pN} = 14.1A^{0.65} \tag{5.25}$$

this parametrization is used for unmeasured nuclei like Tungsten.

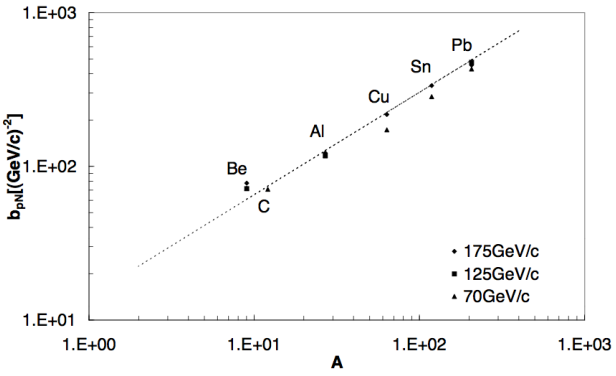

Figure 5.13. Experimental measurements of the slope factor parameter for proton-nucleus elastic scattering b_{pN} versus atomic weight A [31].

Proton-nucleus inelastic scattering

Due to lack of neutron data, the proton measured values are used to calculate the neutron-nucleus inelastic scattering cross section; therefore is assumed $\sigma_{pN}^{in} \approx \sigma_{nN}^{in}$. The proton-nucleus inelastic cross section is inherited from the dependence of the σ_{pN}^{tot} cross section in the following way:

$$\sigma_{pN}^{in} = \sigma_{pN,ref}^{in} \cdot \frac{\sigma_{pN}^{tot}}{\sigma_{pN,ref}^{tot}} \tag{5.26}$$

The reference proton nucleus inelastic cross section $\sigma_{pN,ref}^{in}$ has been updated using recent data of the nuclear interaction length from the Particle Data Group [42].

Table5.4 shows the atomic mass, the interaction length and the reference inelastic cross section for several materials [42]. The inelastic cross section is calculated as follows:

$$\sigma_{pN}^{in} = \frac{A}{N_A \rho \lambda_{int}}. \tag{5.27}$$

where A is the atomic mass, N_A the Avocadro number and λ_{int} the nuclear interaction length. The inelastic cross section scales approximately with the nuclei atomic mass as $A^{0.71}$.

Table 5.4. Atomic mass, nuclear interaction length and reference inelastic cross section for different materials [42].

Material	A [g/mol]	λ_{int} [g/cm^{-2}]	$\sigma_{pN,ref}^{in}$ [b]
Beryllium	9.01	77.8	0.192
Aluminum	26.9	107.2	0.418
Copper	65.6	137.3	0.769
Tungsten	183.8	191.9	1.591
Lead	207.2	199.6	1.724
Carbon	12.01	85.8	0.232

Proton-nucleus total cross section

The proton-nucleus total cross section can be expressed as the sum of the coherent and the incoherent components:

$$\sigma_{pN}^{tot} = \sigma_{pN}^{coh,tot} + \sigma_{pN}^{incoh,tot}(s) \tag{5.28}$$

where the coherent term does not depend on s. The reference total cross section can be also expressed as the sum of the coherent and the incoherent components:

$$\sigma_{pN,ref}^{tot} = \sigma_{ref}^{coh,tot} + \sigma_{pN,ref}^{incoh,tot}(s). \tag{5.29}$$

By subtracting the previous two expressions the following equation is obtained:

$$\sigma_{pN}^{tot} - \sigma_{pN,ref}^{tot} = \sigma_{pN}^{incoh,tot}(s) - \sigma_{pN,ref}^{incoh,tot}(s). \tag{5.30}$$

Expanding the incoherent contributions of the n_{eff} nucleons, the s-dependence is explicited in the following formula:

$$\sigma_{pN}^{tot} = \sigma_{pN,ref}^{tot} + n_{eff}(A)(\sigma_{pp}^{tot} - \sigma_{pp,ref}^{tot}). \tag{5.31}$$

As well as the inelastic proton-nucleus cross section, the total proton-nucleus cross section has been updated using the latest data from [42], in particular the Eq.5.27 has been applied using the specific nuclear collision length of each material considered. Table 5.5 shows the atomic mass, the nuclear collision length and the reference total proton-nucleus cross sections for different materials [42].

Table 5.5. Atomic mass, nuclear collision length and reference total proton-nucleus cross sections for different materials [42]

Material	A [g/m]	λ_{coll} [g/cm^{-2}]	$\sigma^{tot}_{pN,ref}$ [b]
Beryllium	9.01	55.3	0.271
Aluminum	26.9	69.7	0.643
Copper	65.6	84.2	1.253
Tungsten	183.8	110.4	2.765
Lead	207.2	114.1	3.016
Carbon	12.01	59.2	0.337

5.3.3 Rutherford scattering

The Rutherford scattering at large angles, is added, as in the previous SixTrack version, to the total cross section by considering the following formula:

$$\frac{d\sigma_{rth}}{dt} = 4\pi\alpha^2(\hbar c)^2\frac{Z^2}{t^2}e^{-0.856\cdot10^3 tR^2} \tag{5.32}$$

where the fine structure constant $\alpha = 1/137$, the conversion factor $(\hbar c)^2 = 0.389$ GeV^2 mbarn, the Z is atomic number and R is the radius of the nucleus. The unmeasured nuclear radii are calculated by the following:

$$R = 2\hbar c\sqrt{b} \tag{5.33}$$

(where $\hbar c = 0.197$ GeV fm). The exponential factor is the nuclear form factor for a Gaussian charge distribution while the term proportional to $1/t^2$ is the classical Rutherford formula for Coulomb scattering with a point-like charge. The Rutherford scattering is considered only above the limit where the multiple scattering is no longer valid. In particular, the limit is imposed at $\theta_{cut} = 2.325\,\theta_0$ where θ_0 is the rms angular kick received by the particle for a traversed unit length of matter. With the θ_{cut} value only the 1% tail of the multiple Coulomb scattering is missing. The Rutherford cross section is computed integrating the Eq.5.33 in the range $[t_{cut} = (p\theta_{cut})^2, \infty]$.

5.4 Material properties

The SixTrack code contains a dedicate code block where several material properties (density, atomic mass, radiation length etc.) are initialized. These properties are used in the whole software, as well in the scattering routine to generate the mean free path and calculate the cross section values. Some of the nuclear properties for several jaw materials are summarized in Table 5.6. The previous Carbon density value has been replaced by the Carbon/Carbon Tatsuno/Across (AC150K) density value shown in Table 5.6. The AC150K material constitutes TCPs and TCSPs collimators. This material has the same atomic structure of graphitic Carbon but its compaction rate significantly reduces the density with respect to the common graphite one. The new SixTrack routine contains the correct density for the Carbon material used in the LHC collimator jaws.

Table 5.6. Nuclear and atomic properties for implemented materials in SixTrack, in particular atomic weight A, density ρ and radiation length χ_0.

Material	A [g mol^{-1}]	ρ [g cm^{-3}]	χ_0 [m]
Beryllium (Be)	9.01	1.848	0.353
Aluminum (Al)	26.98	2.70	0.089
Copper (Cu)	63.55	8.96	0.0143
Tungsten (W)	183.85	19.3	0.0035
Lead (Pb)	207.19	11.35	0.0056
Carbon (C)	12.01	1.65 [1]	0.188

[1] New implemented AC150K density.

5.5 Detailed distribution of individual processes

As discussed above, when a charged particle passes through a thickness of material undergoes continuos processes due to the electromagnetic interaction, such as multiple Coulomb scattering and ionization, and discrete processes due to the point-like interactions with the material nuclei. Each discrete process is characterized by a finite cross section related to its probability to occur and by a differential cross section that gives the probability to find the scattered proton with a certain angle and momentum. After each simulated processes the interaction details, such as angle of the scattered proton, final proton energy, interaction length and interaction type are recorded in a specific file called `interactions_inside_jaw.dat`.

The angular distributions of the proton-proton single diffractive scattering, proton-proton elastic scattering and proton-nucleus elastic scattering are shown in Fig.5.14, Fig.5.15 and Fig.5.16 respectively. The simulations have been performed using the pencil beam configuration in the case of horizontal halo at 7 TeV for Beam 1. The selected collimator is the TCP.C6L7, made by AC150K material with a length of 60 cm. In particular, all the impacting particles have the same energy and the same angle $x' = 0$ rad. From the plots is possible to observe that the major angular spread is given by the single diffractive scattering.

The single diffractive scattering is characterized by a not negligible particle momen-

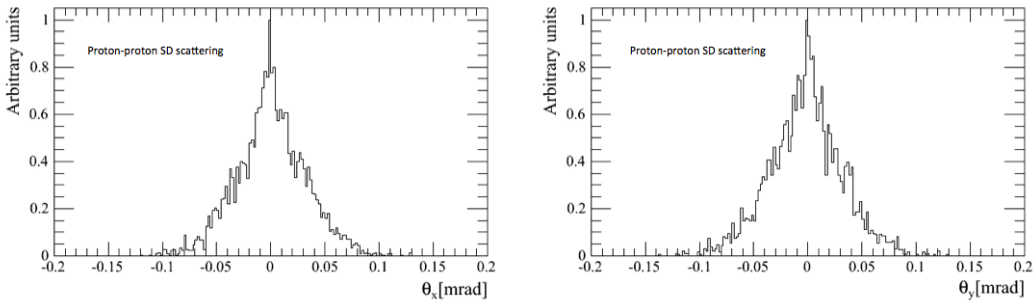

Figure 5.14. Angular distribution of the proton-proton single diffractive scattering in x and y directions.

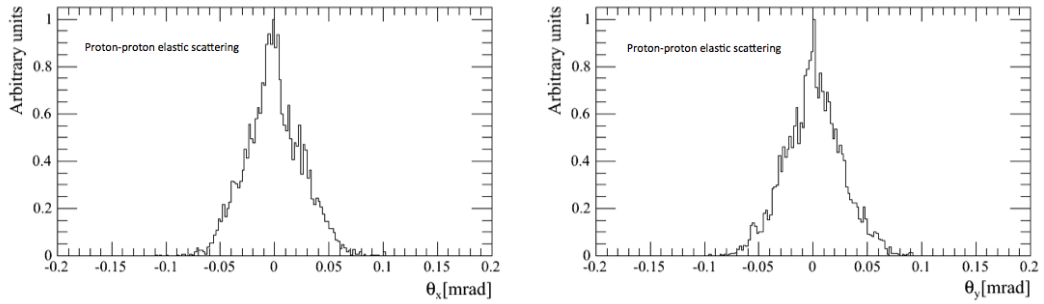

Figure 5.15. Angular distribution of the proton-proton elastic scattering in x and y directions.

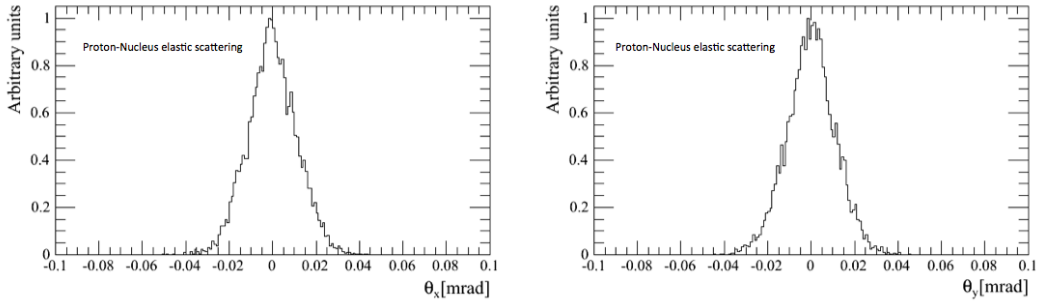

Figure 5.16. Angular distribution of the proton-nucleus elastic scattering in x and y directions.

tum transfer to the nucleus producing an new excited state of mass (see section 5.3.1). The distribution of the energy variation with respect to the initial momentum, defined as: $\Delta E = p_f - p_0$, is presented in Fig.5.17. The ionization contribution has been subtracted from the final particle momentum. Most of the diffracted particles were affected by an energy variation between 2 GeV and 15 GeV, while the variation energy of the particles in the distribution tail reaches the 50 GeV.

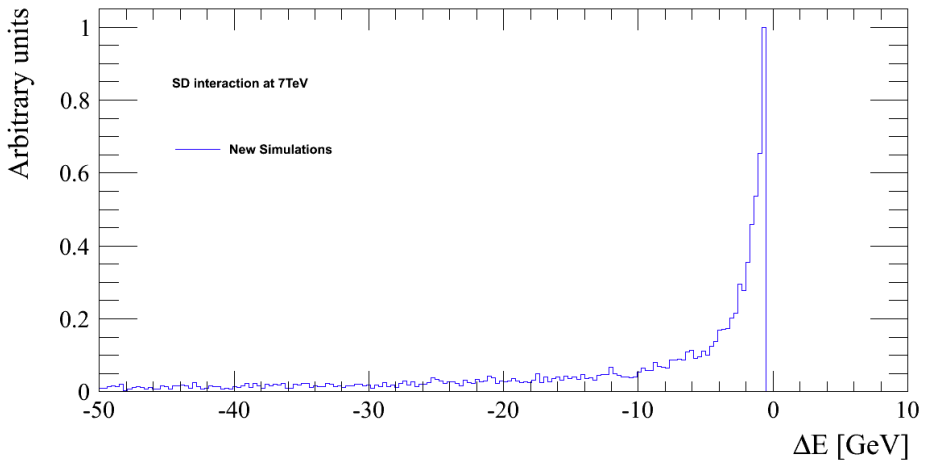

Figure 5.17. Energy variation of the scattered proton after p-p single diffractive process.

Chapter 6

Validation of the improved scattering routine of SixTrack

The improvements in the scattering routine of SixTrack were described in detailed in the previous Chapter. Detailed distributions of the outgoing angle and the change of energy were shown for different interactions. However, the final validation of the code has to be done in a more general way.
In this chapter we investigate the change on the simulated distribution of the losses along the LHC ring after every change on the code. In particular we give especial emphasis at the change on the cleaning inefficiency in the dispersion suppression region of the IR7 and at the impacts at the TCTs in the IR1 and IR5.
The previous SixTrack routine was validated agains the data with protons at 3.5 TeV beam energy. Here we reproduce these results an give an update on the changes after the improvements in the scattering routine.

6.1 Effect of scattering routine updates on simulations

In order to investigate the effect of each change in the SixTrack scattering routine, the losses in the dispersion suppression region of IR7 and the number of absorbed protons at the collimators are studied for each individual change. The eight changes implemented in the SixTrack scattering routine that are described in Chapter 5 are:

- **case 0:** This case corresponds to the previous SixTrack version.
- **case 1:** Update of the Carbon density that matches the Carbon used in the present collimation system.
- **case 2:** Case 1 with the update on the multiple coulomb scattering process, adding the logarithm part on the calculation of the angle rms.
- **case 3:** Case 2 with the implementation of the Bethe-Bloch equation to calculate the energy loss by ionization.
- **case 4:** Case 3 with the update of the proton-proton elastic cross section, σ_{pp}^{el}, including new data measurement from TOTEM Collaboration.

- **case 5:** Case 4 with the updated of the proton-proton total cross section, σ_{pp}^{tot}, including new data measurement from TOTEM Collaboration.
- **case 6:** Case 5 with the updated of the proton-proton single diffractive cross section, σ_{pp}^{SD}.
- **case 7:** Case 6 with the updated of the proton-nucleus total cross section, σ_{pN}^{tot}, from the PDG.
- **case 8:** Case 7 with the updated of the proton-nucleus inelastic cross section, σ_{pN}^{in}, from the PDG.

6.1.1 Simulation setup

In order to study the effect of the changes implemented in the scattering routine, the simulations of protons at 7 TeV energy with LHC nominal settings before and after the changes are compared. For these simulations we used the collimator settings shown in Fig. 6.1, expressed in beam sigma size with normalized transverse emittance of 3.5 mm mrad. The beta-star at IP1 and IP5 was set to 0.55 m and to 10 m in IP2 and IP8 as shown in Fig. 6.2.

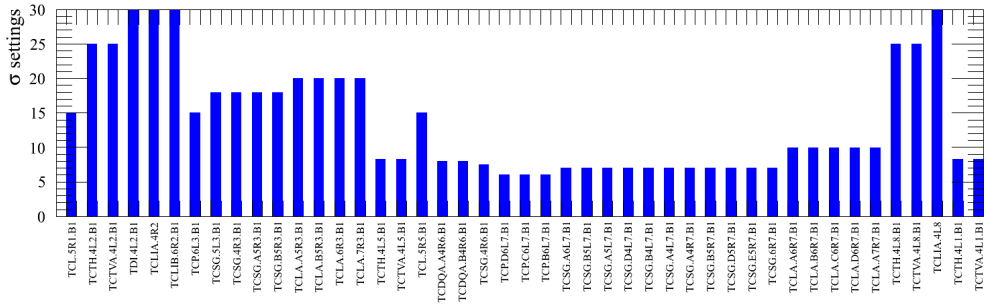

Figure 6.1. Collimator settings for Beam 1 at 7 TeV, assuming normalized transverse emittance of 3.5 mm mrad.

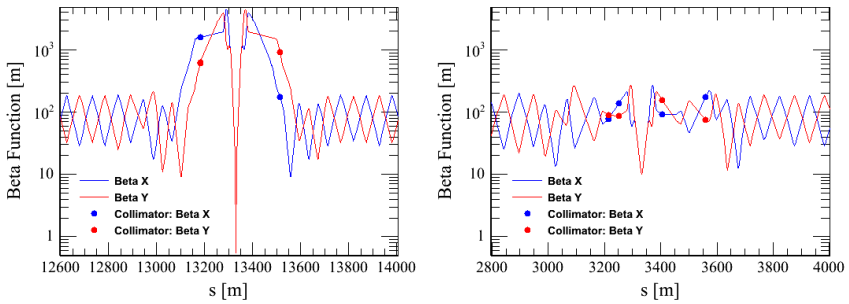

Figure 6.2. Beta function at IP5 (same for IP1) and IP2 (same at IP8) for Beam 1, protons at 7 TeV, nominal LHC optics.

6.1.2 Cleaning inefficiency

The cleaning inefficiency, previously introduced, represents the number of particles leaking from the collimation system that can be lost in the aperture. For a betatron halo cleaning in the LHC, the highest cleaning inefficiency occurs at the dispersion suppressor of IR7, typically Q9 cell. This means, that the superconducting magnets in that area are the most affected by the leakage from collimators. Fig. 6.3 shows the cleaning inefficiency for two simulations, protons at 7 TeV for each individual change on the scattering routine. The case 0 bin corresponds to the old simulation routine and case 9 to the final version. At 7 TeV all the changes tend to increase the leakage into the DS of IR7. This effect goes in the correct direction since, as it will be shown later, the comparisons with data show that the old simulations were underestimating the betatron cleaning leakage. The final effect is around a factor of 2 higher leakage at 7 TeV for Beam 1 horizontal halo. The case at 4 TeV follows the same tendency, although individual processions were slightly decreasing the leakage, the final effect is also a factor of 2 higher leakage in Q9.

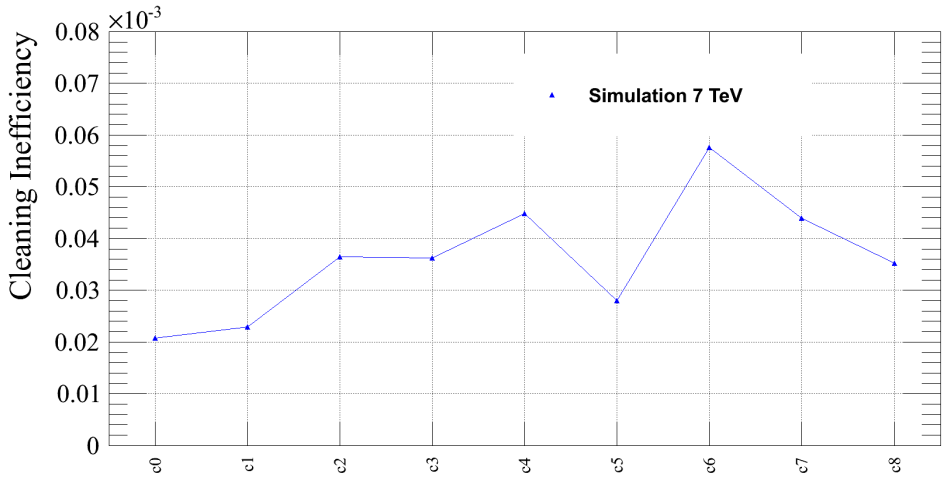

Figure 6.3. Cleaning inefficiency for simulations at 7 TeV in the IR7 cold magnets. The different labels on the x-axis correspond to each one of the changes made on the scattering routine as explained in Section 6.1

6.1.3 Impacts at collimators

The particles absorbed at all collimators are shown in Fig 6.4 for the simulation of Beam 1 horizontal halo with protons at 7 TeV. The red line and the red points represent the impacts using the old SixTrack version simulations while the blue line and the blue points are the impacts of the new SixTrack simulations. From the plot is possible to deduce that the effect of the new simulations is to increase the fraction of particles absorbed downstream the primary collimators. This could be the net effect of increasing the single diffractive cross section. Increasing this cross sections, will increase the probability of having protons that have a first impact at the primary collimator deflected with a lower momentum but still accepted for the machine and therefore lost downstream.

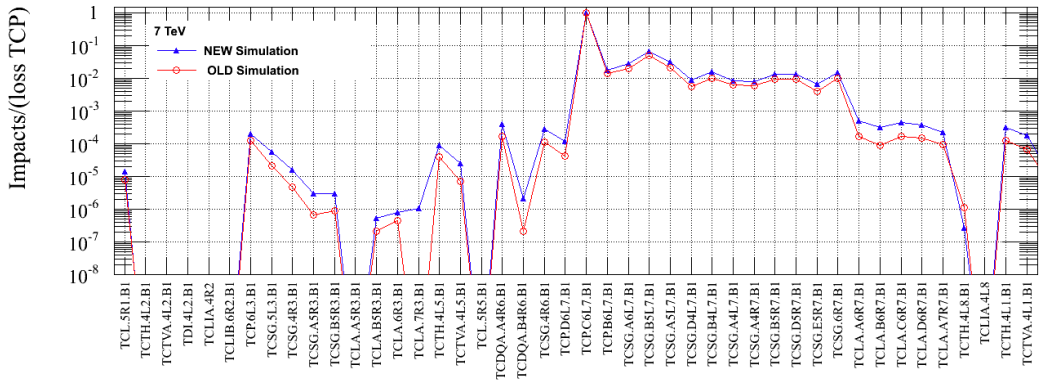

Figure 6.4. Particles absorbed at all collimators normalized to the particles absorbed at the horizontal primary collimator in IR7.

6.2 Measurements of beam losses at the LHC

During LHC Run I (2010-2013), beam losses were generated periodically on dedicated low intensity fills in order to validate the collimation hierarchy settings and to identify the limiting locations along the LHC ring. The beam was blown up independently in vertical and horizontal plane until the beam tails touch the collimators, generating beam losses in all the collimation system.

6.2.1 Generation of beam losses: ADT and resonance method

To validate the collimation system, the beams are excited artificially in order to generate sufficient loss rates to measure the collimation cleaning. Two methods have been used to blow up the beam and perform the loss maps: the Tune resonance (QT) and the Transverse Dumper (ADT) method. The resonance method is a technique to move the tune across a third order resonance in the vertical and horizontal plane. The excited beam in a plane can be affected by the tune changes in the other plane causing beam instability and uncontrolled losses in the machine. In most of the cases the beam is dumped during the loss map measurements, for this reason a controlled transverse blow up of the beam is required. The ADT method allows to perform aperture measurements and loss maps with high intensity bunch trains without a limited bunch number needed. This technique was extensibly used during 2012 and 2013 runs, and developed to blow-up transversely the LHC proton beams [43, 44]. This method is based on white noise beam excitation in selected bunches, both in the horizontal and the vertical plane independently. The speed of transverse blow-up can be precisely controlled. This method is very precise and allows to control the losses very accurately during the data taking. At the end of 2012 run it was possible to excite individual 25 ns separated bunches without affecting the adjacent bunches. The ADT method was used for the collimation quench test in 2013 where losses up to 1MW were generated over few seconds in a very controlled way with unsafe beam intensity in the machine.

6.2.2 The BLM system

In order to protect the LHC superconducting magnets against quench and beam induced damage, the losses are monitored mainly by the Beam Loss Monitoring System (BLM) that detects and quantifies the amount of lost beam particles. It generates a beam abort trigger when the losses exceed predetermined threshold values. The BLMs are ionization chambers to detect secondary particles originating from the beam losses on the lattice elements: cold magnets, collimators, warm magnets, etc. The detectors probe the transverse tails of the hadronic showers emerging from the cryostat, which are induced by lost beam particles. The voltage applied to the electrodes of the ionization chamber moves the ionization charges inducing a signal current on the two electrodes. In the ideal ionization chamber the measured current is proportional to the amount of charges liberated by energy deposition from the passing particle. About 4000 detectors are installed, mostly around the quadrupole magnets, but also downstream each collimators, to control the beam losses and provide machine protection.

6.2.3 Loss maps during LHC Run I (2010-2013)

The local betatron cleaning inefficiency from 2010 to 2012 is shown in Fig 6.5 [45]. The figure shows an excellent stability of the cleaning performance. The changes of cleaning inefficiency appears when the collimator settings were changed. In 2011 the machine was running with the so-called relaxed collimators settings, while in 2012 the so-called tight collimator settings (with reduce aperture) were used which resulted on reducing the leakage in the DS of IR7.

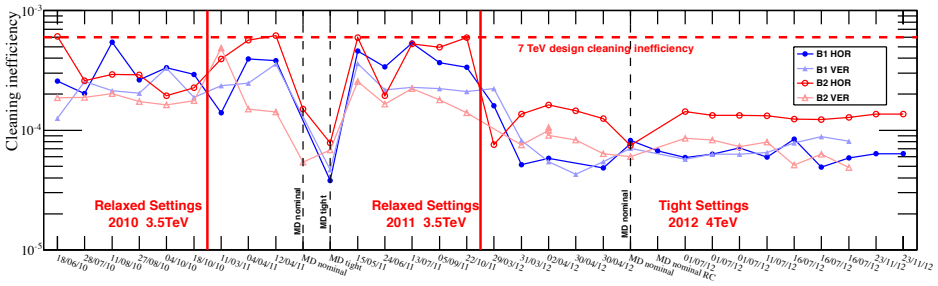

Figure 6.5. Collimation cleaning inefficiency as function of time since 2010 until end of 2012 run [45].

Fig.6.6 shows a loss map of LHC during the Run I with the tight setting configuration. The distribution of the losses in the betatron cleaning insertion IR7 is also shown in Fig.6.7.

6.3 Validation of the SixTrack scattering routine with data

The ultimate validation of the SixTrack scattering routine should be done by comparing the simulation predictions with the real measurements. This was done with

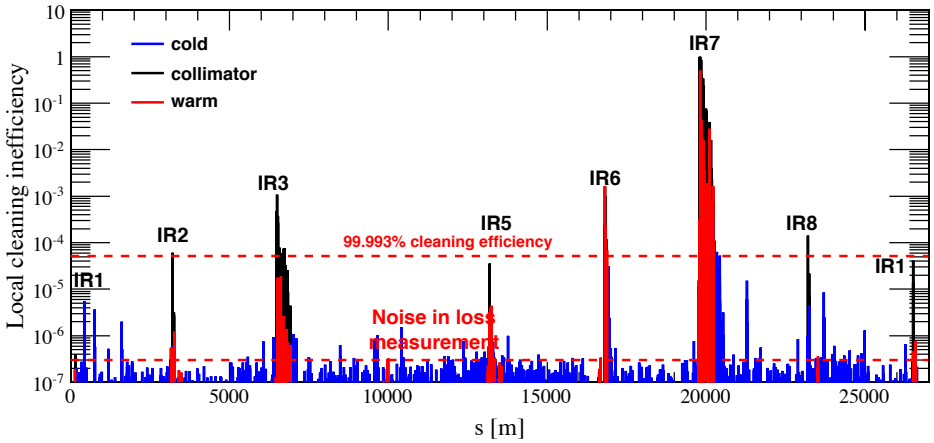

Figure 6.6. Distribution of the losses in the LHC ring [45].

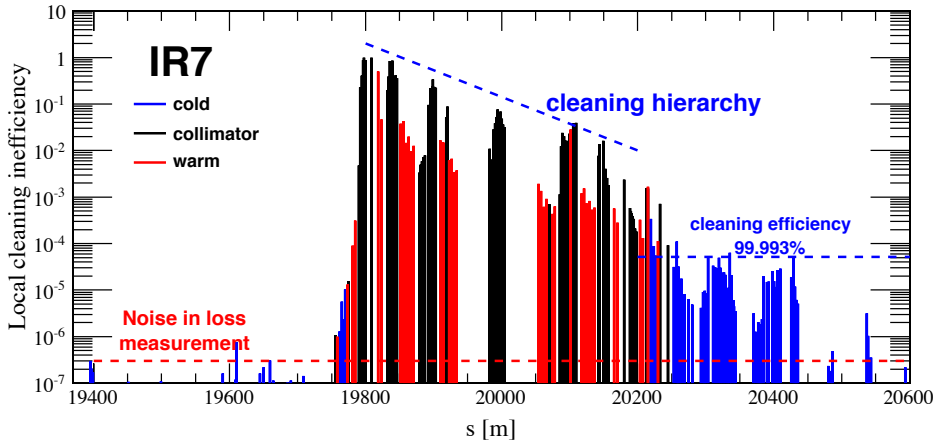

Figure 6.7. Distribution of the losses in the betatron cleaning insertion IR7 [45].

the previous routine [46] by comparing the qualification loss maps with protons at 3.5 TeV beam energy. Here we present the new comparison after the improvements on the scattering routine.

6.3.1 Machine configuration

This time the optics are configured to run with protons at 3.5 TeV beam energy. The beta-star in IP1 and IP5 was set to 1.5 m as shown in Fig.6.8. Fig. 6.9 shows the beta-star configuration of IP2 (left) and IP8 (right). In this case, IP2 was configured with $\beta^\star = 10\,\mathrm{m}$ while IP8 was configured with $\beta^\star = 3\,\mathrm{m}$.

6.3.2 Collimator settings

In 2011 the LHC machine was running with the so-called relaxed collimator settings. These settings are more relaxed, which means with more aperture than the nominal settings but sufficient cleaning is still provided at the proton energy of 3.5 TeV. Table 6.1 and Fg.6.10 show the settings used for the simulations. The collimators

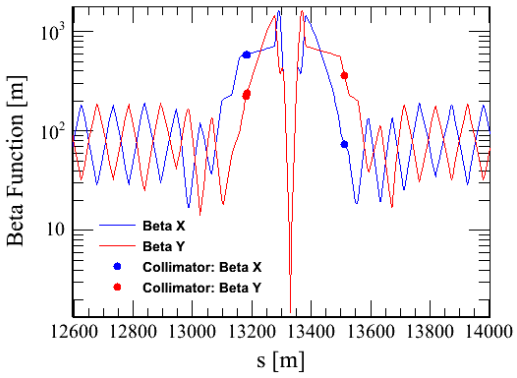

Figure 6.8. Beta-star at IP5 for protons at 3.5 TeV, the same beta-star was used in IP1.

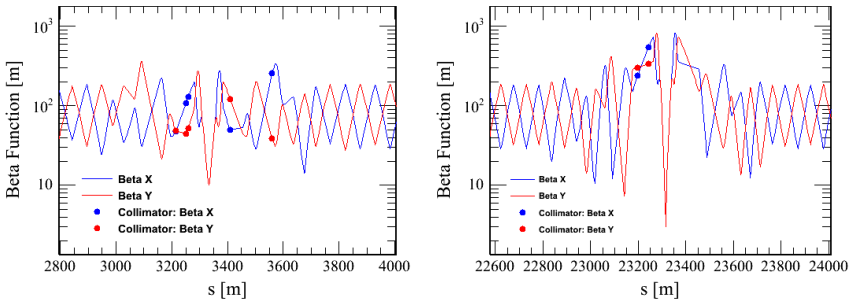

Figure 6.9. Beta-star at IP2 (left) and IP8 (right) for protons at 3.5 TeV.

that are not listened are completely opened in the simulations.

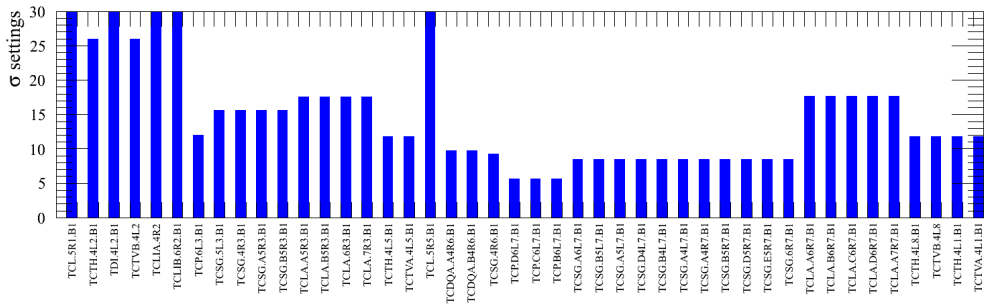

Figure 6.10. Collimator settings for Beam 1 with protons at 3.5 TeV.

6.3.3 BLM response factor

SixTrack simulations provide the estimation of the impacts at the collimators and the particles lost at the aperture along the LHC ring. However, data measurements are done by recording the showers from protons impacting different parts of the LHC (collimators, beam pipe, etc.) with ionization chambers located downstream

Table 6.1. Collimator settings during 2011 Run with protons at 3.5 TeV beam energy, the settings are expressed in beam sigma size assuming 3.5TeV µ mrad.

IP	**Collimator Type**	**Aperture** $[\sigma]$
IP3	TCP	12.0
IP3	TCSG	15.6
IP3	TCLA	17.6
IP7	TCP	5.7
IP7	TCSG	8.5
IP7	TCLA	17.7
IP6	TCDQ	9.8
IP6	TCSG	9.3
IP1	TCTH	11.8
IP2	TCTH	26.0
IP5	TCTH	11.8
IP8	TCTH	11.8
IP1	TCTV	11.8
IP2	TCTV	26.0
IP5	TCTV	11.8
IP8	TCTV	11.8

the showers. Therefore, is important to convert the number of impacting or lost protons into the expected signal recorded with the BLMs. In order to perform the data-simulations comparison, this conversion factors are calculated with the FLUKA code [24, 25]. The FLUKA program takes the output from SixTrack, thus the distribution of the impacts, and adds the hadronic shower and the BLM response. These factors can be expressed as a matrix transformation between the impacts at the collimators and the corresponding BLM signal, see Eq. 6.1. Where $\mathrm{BLM_H}$ and $\mathrm{BLM_V}$ denotes the simulated BLM signal for the monitor placed after the horizontal and vertical collimators respectively. $\mathrm{I_H}$ and $\mathrm{I_V}$ are the impacts at the horizontal and vertical collimators respectively and a_{11}, a_{12}, a_{21} and a_{22} are the conversion factors. Table 6.2 and 6.3 show these factors of the primaries collimators in IP7 and the tertiary collimators in IP1 and IP5, for the halo generation in the horizontal and vertical respectively of Beam 1.

$$\begin{pmatrix} \mathrm{BLM_H} \\ \mathrm{BLM_V} \end{pmatrix} = \begin{pmatrix} a_{11} & a_{12} \\ a_{21} & a_{22} \end{pmatrix} \cdot \begin{pmatrix} \mathrm{I_H} \\ \mathrm{I_V} \end{pmatrix} \tag{6.1}$$

Table 6.2. BLM response factors from FLUKA and SixTrack for Beam 1 horizontal halo, in units of 10^{-4} GeV/p [46] [47].

	a_{11}	a_{12}	a_{21}	a_{22}
TCP IP7	0.531	0.956	0.006	0.307
TCT IP1	3.661	0.219	0.570	1.758
TCT IP5	3.329	0.229	0.643	1.712

Table 6.3. BLM response factors from FLUKA and SixTrack for Beam 1 vertical halo, in units of 10^{-4} GeV/p [46] [47].

	a_{11}	a_{12}	a_{21}	a_{22}
TCP IP7	0.531	0.956	0.006	0.307
TCT IP1	3.824	0.210	0.604	1.723
TCT IP5	3.569	0.281	0.781	1.637

6.3.4 Comparisons between data and simulations

The triplet quadrupole magnets are installed to reduce the optical β function in the collision points of LHC. Tertiary collimators provide local beam cleaning to protect the triplets avoiding magnet quenches.
The TCTs intercept the the tertiary halo reducing the number of particle impacting on the superconducting triplet magnets. A comparison between measurements and simulations of the impacts at the tertiary collimators are presented in Fig.6.11 at 3.5 TeV for Beam 1 horizontal halo case (top) and vertical halo case (bottom). Both the measured and simulated losses are normalized to the number of particle lost at TCP collimators. The black line represents the BLM experimental data [46], in particular the experimental points are the average ratio over all 2011 loss maps. The simulations have been performed for a perfect machine using the new SixTrack version and the old SixTrack version: they are shown in the plot in blue and red respectively. The dashed lines represent the simulation without FLUKA factor conversion while the solid lines represent the simulations after applying the BLM response factors calculated by FLUKA simulations [47].

Table 6.4. Maximum of losses on the cold magnets for the simulations with the new SixTrack version and the old SixTrack version (Beam 1 horizontal halo case).

Cold Magnet	Max loss/(loss at TCP) New routine	Max loss/(loss at TCP) Old routine
Q8	3.073×10^{-5}	1.725×10^{-5}
Q9	6.260×10^{-5}	3.558×10^{-5}
Q10	7.967×10^{-6}	2.156×10^{-6}
Q11	3.870×10^{-5}	1.833×10^{-5}

Table 6.5. Integrated losses on the cold magnets for simulations with the new SixTrack version and the old SixTrack version (Beam 1 horizontal halo case).

Cold Magnet	Integrated loss/(loss at TCP) New routine	Integrated loss/(loss at TCP) Old routine
Q8	1.617×10^{-4}	8.217×10^{-4}
Q9	4.454×10^{-3}	2.255×10^{-3}
Q10	5.691×10^{-5}	1.617×10^{-5}
Q11	3.910×10^{-3}	2.096×10^{-3}

The FLUKA factors used in this analysis are shown in Table 6.2 and 6.3. From the plot it is possible to appreciate an increase by a factor of ~ 4 with respect to

previous simulations producing a better estimation of the simulated losses compared to experimental data. The complete simulated loss maps for Beam, horizontal halo case, at 3.5 TeV are shown in Fig.6.12. The cleaning inefficiency on the y-axis has been replaced by the ratio between the particles lost and the losses at the TCP collimator. Fig.6.12a shows the losses in the complete ring simulated by using the new version of the scattering routine, a zoom in the IR7 insertion is also shown in Fig.6.12b.

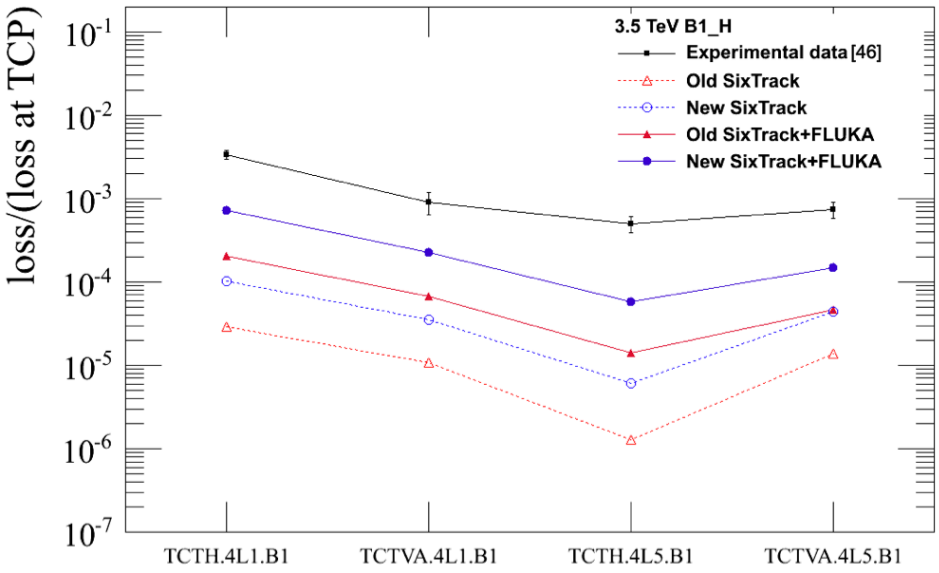

(a) Beam 1 horizontal halo

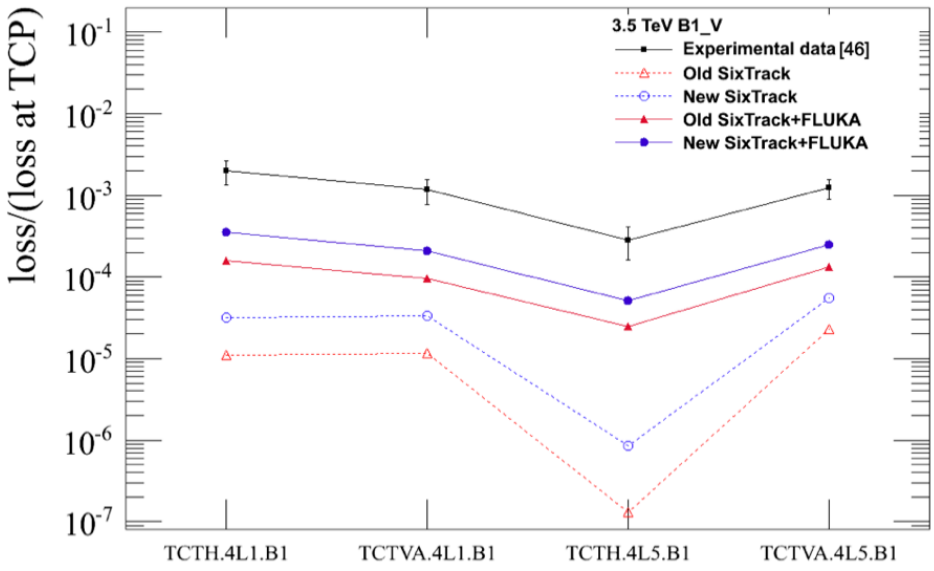

(b) Beam 1 vertical halo

Figure 6.11. Losses at 3.5 TeV from experimental data compared with the simulations performed with the new and old SixTrack version.

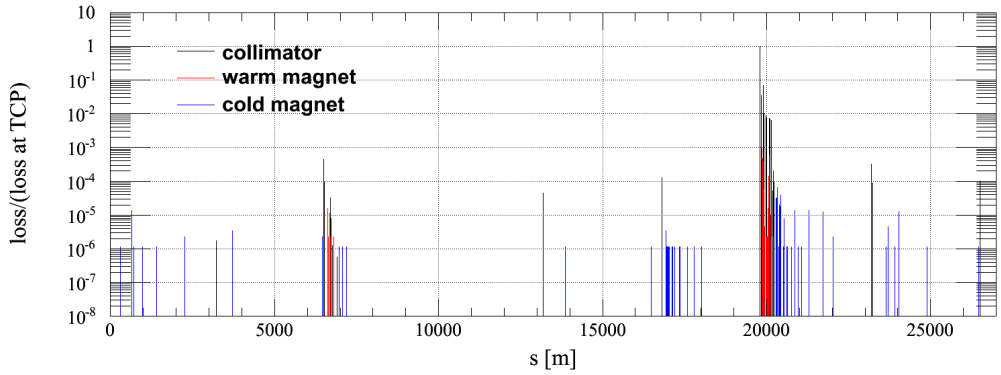

(a) Complete simulated loss map at 3.5 TeV for Beam 1 horizontal (new SixTrack version).

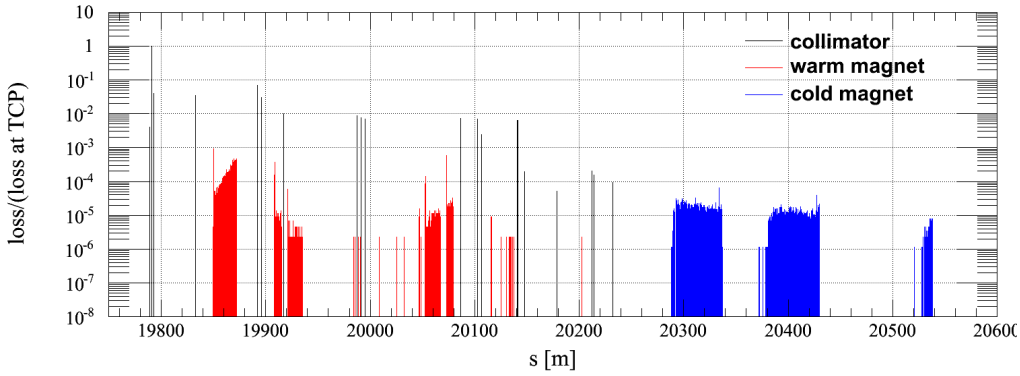

(b) Zoom in IR7 of simulated loss map at 3.5 TeV for Beam 1 horizontal (new SixTrack version).

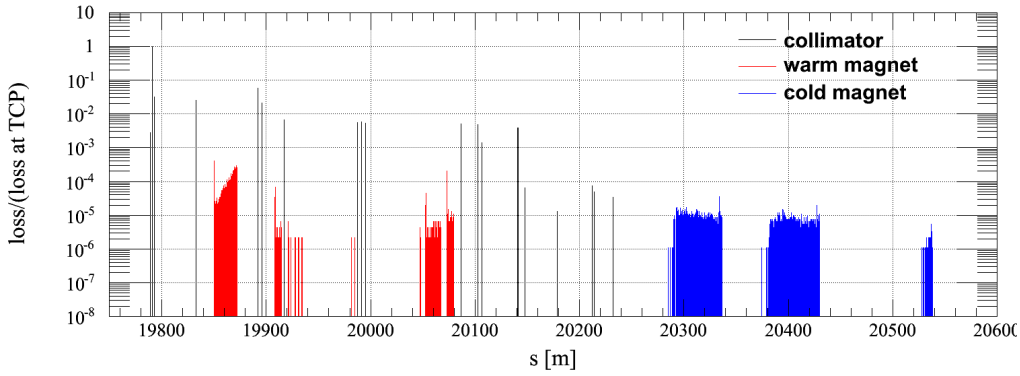

(c) Zoom in IR7 of simulated loss map at 3.5 TeV for Beam 1 horizontal (old SixTrack version).

Figure 6.12. Simulated loss map at 3.5 TeV.

In addition the losses in the IR7 insertion simulated by using the old SixTrack version are represented in Fig.6.12c. Considering the simulation with the new SixTrack version, from the loss maps it is possible to notice an increase of the losses all around the ring. Giving particular attention to the cold magnets located in IR7, Table 6.4 gives the values of the maximum losses on the magnets for the new SixTrack version and the previous one. In the case of the Q10 magnet is reached an increase by a

factor of ~ 4 compared to the previous routine simulations. Table 6.5 shows the integrated losses for each cold magnets in IR7.
The results of the 2011 comparison between measurements and simulation at the TCT collimators are presented in Fig.6.13 from [46] for Beam 1 horizontal halo and Beam 1 vertical halo. Both the measured and the simulated losses are normalized to the number of particle lost at TCP collimators. The red line represents the BLM data, the green line are the simulations from SixTrack and the orange line represents the simulated impacting particles converted to the BLM signal using the FLUKA factors shown in Table 6.2 and 6.3 for Beam1 horizontal and vertical halo respectively. The plots are made by considering the machine with imperfections. The SixTrack simulation with a not perfect machine has been done by including the influence of random collimator imperfections such as error on tilt angles, beam center, gap and jaw curvature in IR7. A factor of 5 is obtained by comparing the perfect machine case in Fig.6.11 for the old SixTrack routine simulations with the imperfect machine case in Fig.6.13. From this comparison is possible to deduce that applying the new routine simulations to the imperfect machine case, a factor of 5 from the imperfect case will bring the simulation predictions extremely close to the data.

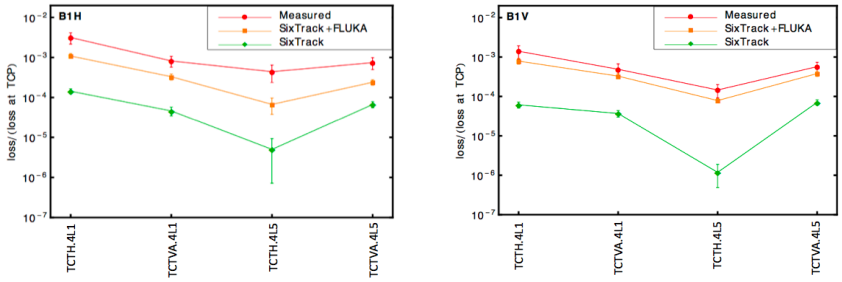

Figure 6.13. BLM signal ratio on horizontal and vertical TCTs to the TCPs in simulations with machine imperfections and measurements in the 2011 machine [46].

Chapter 7

Improved estimation for 7 TeV cleaning performance

The LHC has built to store, accelerate and provide particle collisions with a maximum particle momentum of 7 TeV with a nominal peak luminosity of $\mathcal{L}$=10^{34} cm^2 s^{-1}. During the first run of the LHC with beam energies of 3.5 TeV and 4.0 TeV, no experiences of quenches induced by losses from circulating beams occurred. This situation might change at 7 TeV because of the reduced quench margin of the superconducting magnets. Hence an excellent control of particle losses must be provided by the collimation system. SixTrack simulations using the updated scattering routine have been performed to predict the cleaning performance at the designed energy of 7 TeV.

7.1 Machine configuration at 7 TeV

The LHC collimation system is designed to intercept beam losses and to absorb them in the dedicated cleaning insertions in IR3 (momentum cleaning) and IR7 (betratron cleaning). During the LS1 shutdown period the collimation system is being updated to provide adequate beam cleaning and machine protection at 7 TeV. The nominal design collimator setting in IP3 and IP7 is presented in Table 7.1, the all collimator settings are presented in Table 3.3. The complete collimator layout for the nominal designed energy is shown in Fig.7.1, where in the y-axis are shown the s-position in the LHC ring, the collimators settings used for all collimators are shown in Fig.7.2, where in y-axis are shown the half-gap positions in σ units.

Table 7.1. Collimator settings in IP3 and IP7 for the 7 TeV machine configuration

7 TeV Collimator setting [σ]					
IP3			**IP7**		
TCP	TCSG	TCLA	TCP	TCSG	TCLA
15	18	20	6	7	10

During 2012 the LHC was operating at 4 TeV with beta star at the ATLAS and the CMS interaction points of 0.6 m. The high luminosity insertions expects a beta star value at IP1 and IP5 of 0.55 m. The collision optics at 7 TeV in these two insertions are characterized by crossing angle of $\pm$ 142.5 µrad. This scheme provides

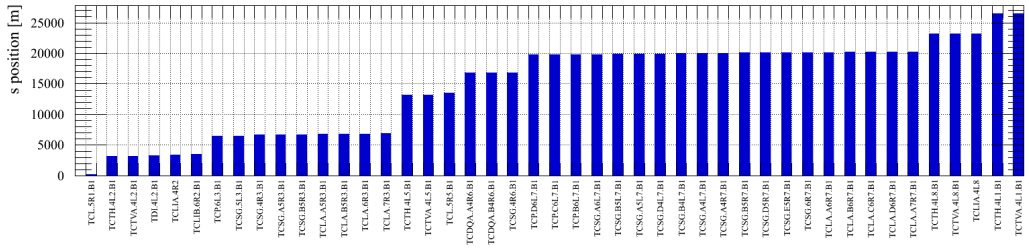

Figure 7.1. Collimator layout for Beam 1 at 7 TeV proton energy.

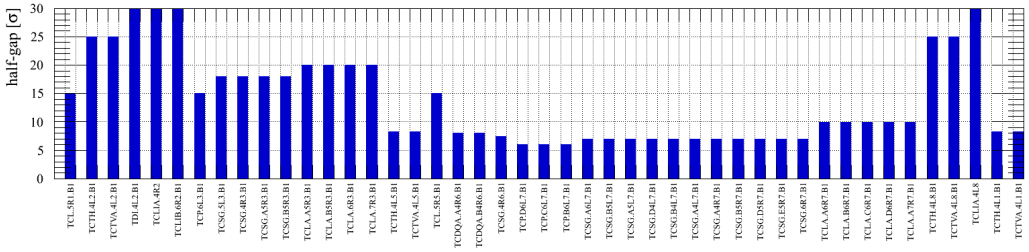

Figure 7.2. Collimator settings at 7 TeV proton energy.

an average beam-beam separation of 9.4 σ. It is really important to keep a sufficient separation between the two colliding beams to reduce any effects from long-range beam interaction. The main limit on the bunch intensity is indeed related to the beam-beam effects. The IR2 insertion hosts the ALICE detector with $\beta^* = 10$ m for protons and 0.5 m for Pb ions. The transverse beam separation is 5 σ. In IR8 is installed the LHCb experiment, here the collision optics expects a beta star of 10 m. In IP2 and in IP8 the crossing angle are $\pm$ 150 µrad and $\pm$ 200 µrad respectively. The IR3 insertion hosts the Momentum Collimation system and provides momentum cleaning. Hence the collimators must be placed at locations with high dispersion and low betatron function, while the collimators in IR7 are placed at low dispersion function to provide betatron cleaning. The β-function in IR3 and in IR7 are shown in Fig.7.3, where the solid points indicate the β-function in a particular collimator.

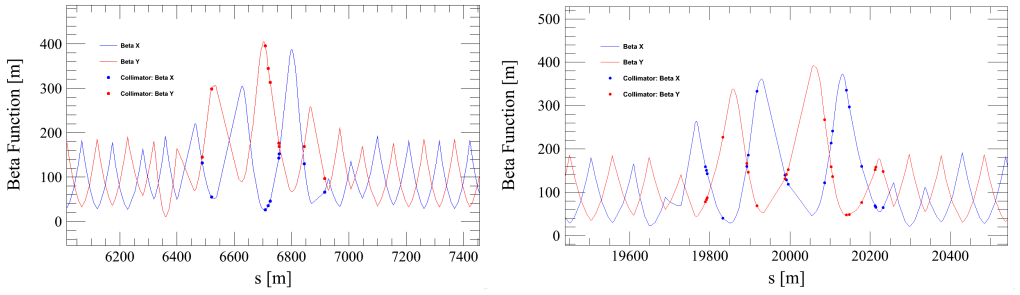

Figure 7.3. β-function in IR3 (left) and IR7 (right) for Beam 1 using nominal LHC optics.

7.2 Loss maps at 7 TeV

The better agreement between the experimental data and the updated SixTrack version, shown in Chapter 6, leads to a better estimation of the losses around the ring at 7 TeV beam energy. In this section are presented the complete loss maps and the detailed distributions of the losses at the betatron cleaning insertion (IR7), for Beam 1 and Beam 2, performed with the new SixTrack version. For Beam 2 the positions of the machine elements (collimators, warm magnets, cold magnets, etc...) appear inverted because Beam 2 circulates in the opposite direction.

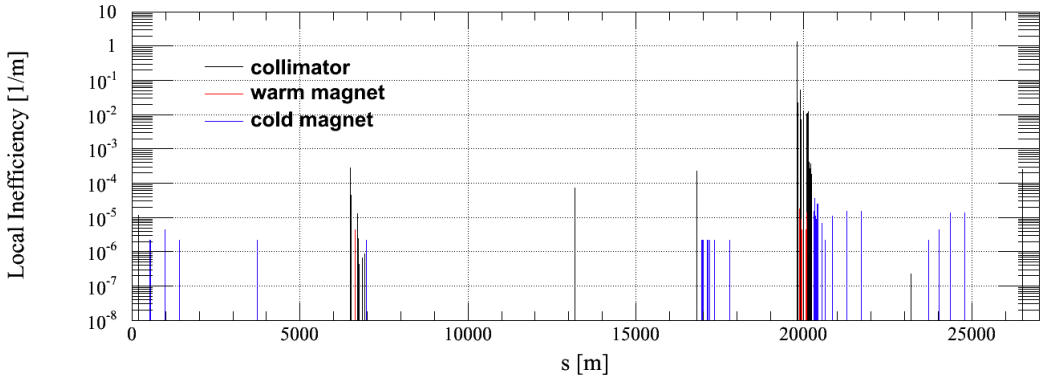

(a) Full ring

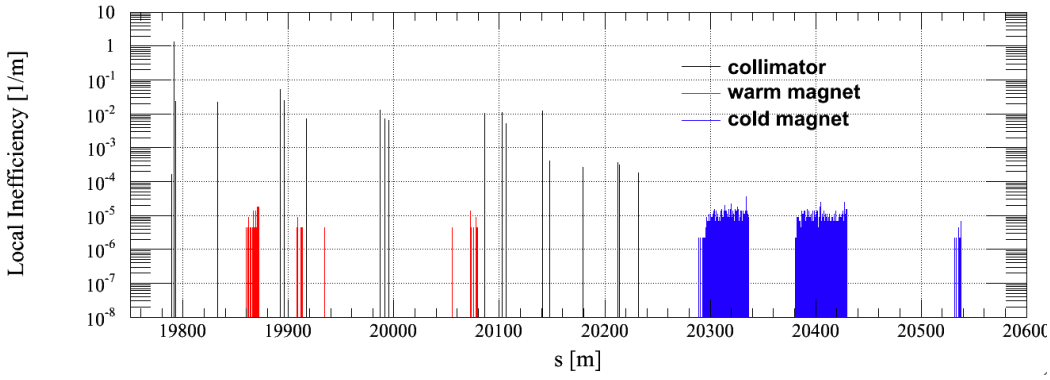

(b) Betatron cleaning insertion IR7

Figure 7.4. Simulated beam loss map at 7 TeV with the new routine for Beam 1 horizontal halo case.

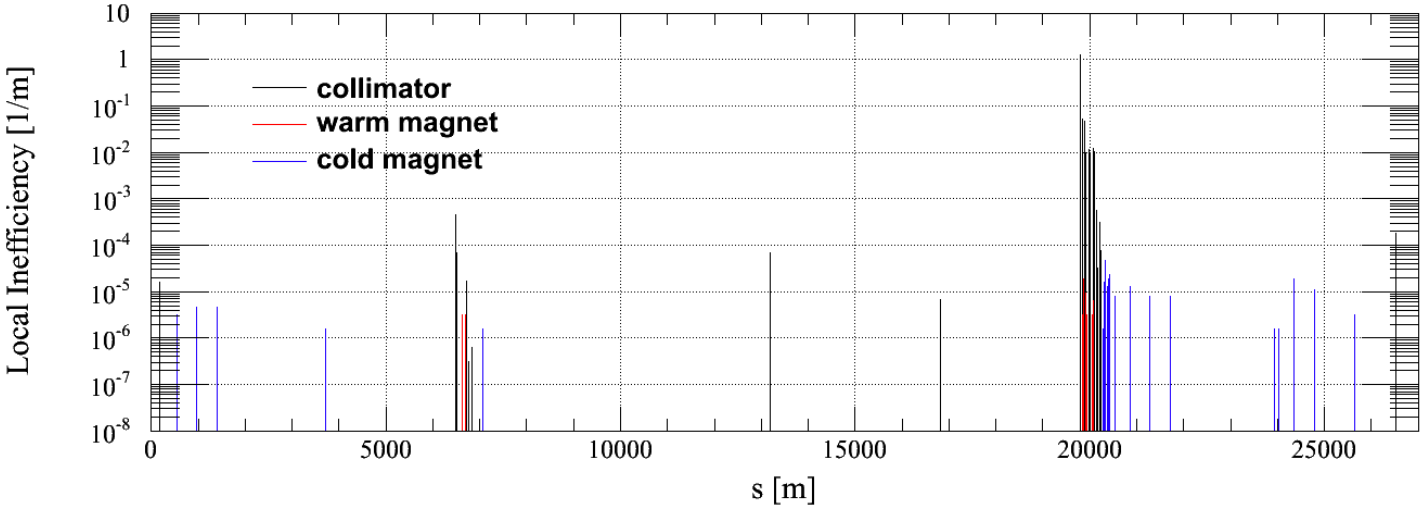

(a) Full ring

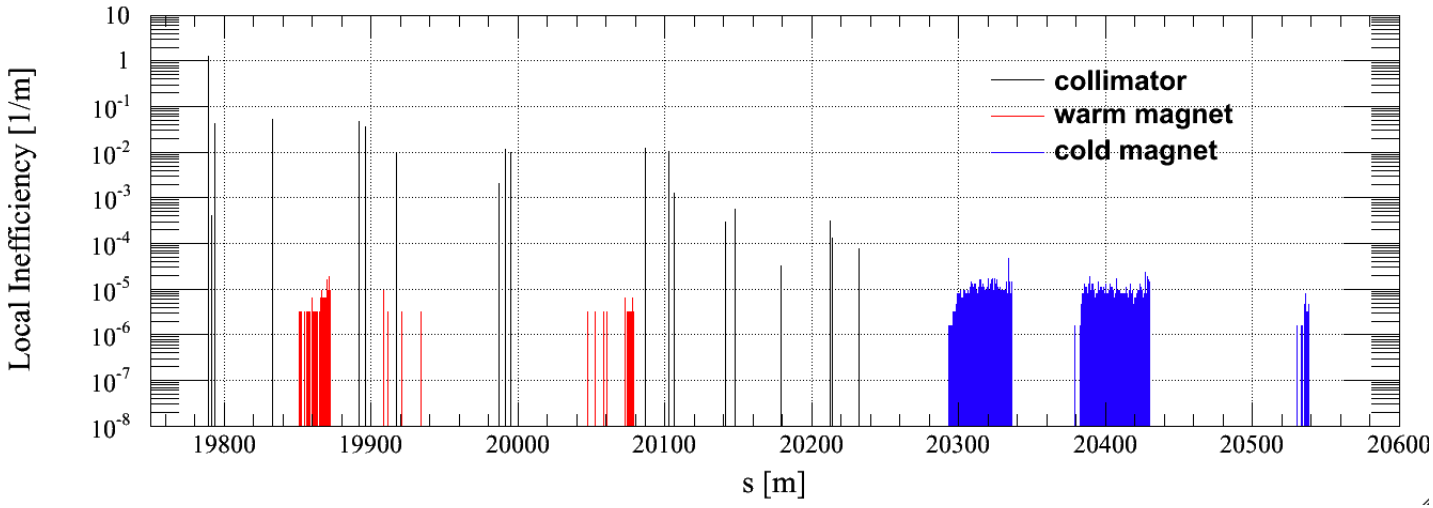

(b) Betatron cleaning insertion IR7

Figure 7.5. Simulated beam loss map at 7 TeV with the new routine for Beam 1 vertical halo case.

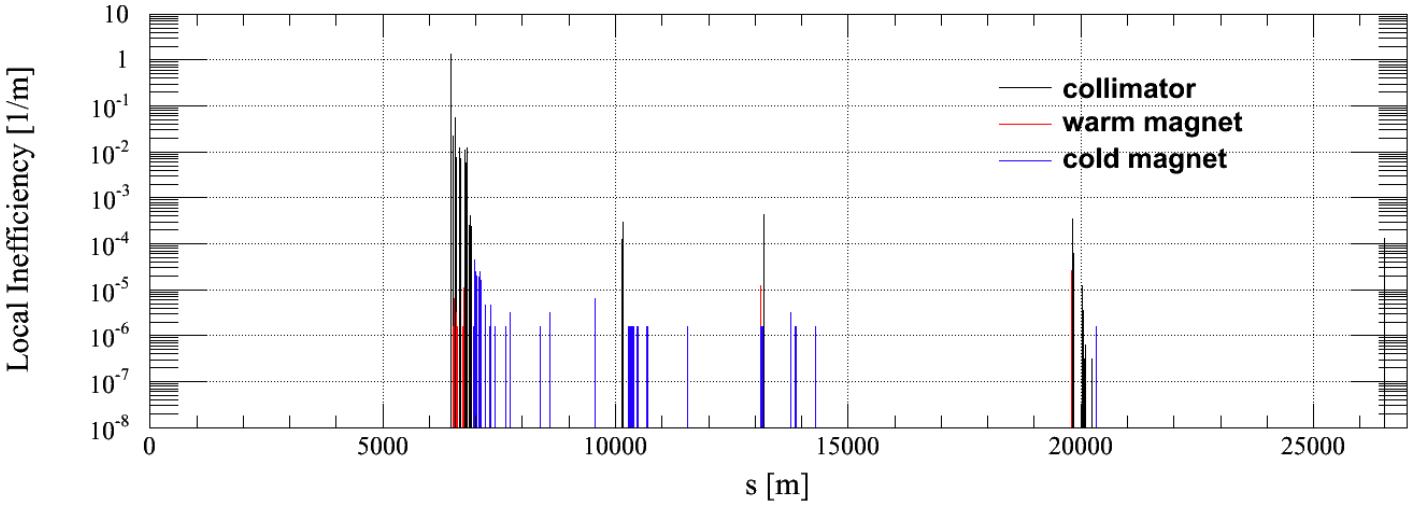

(a) Full ring

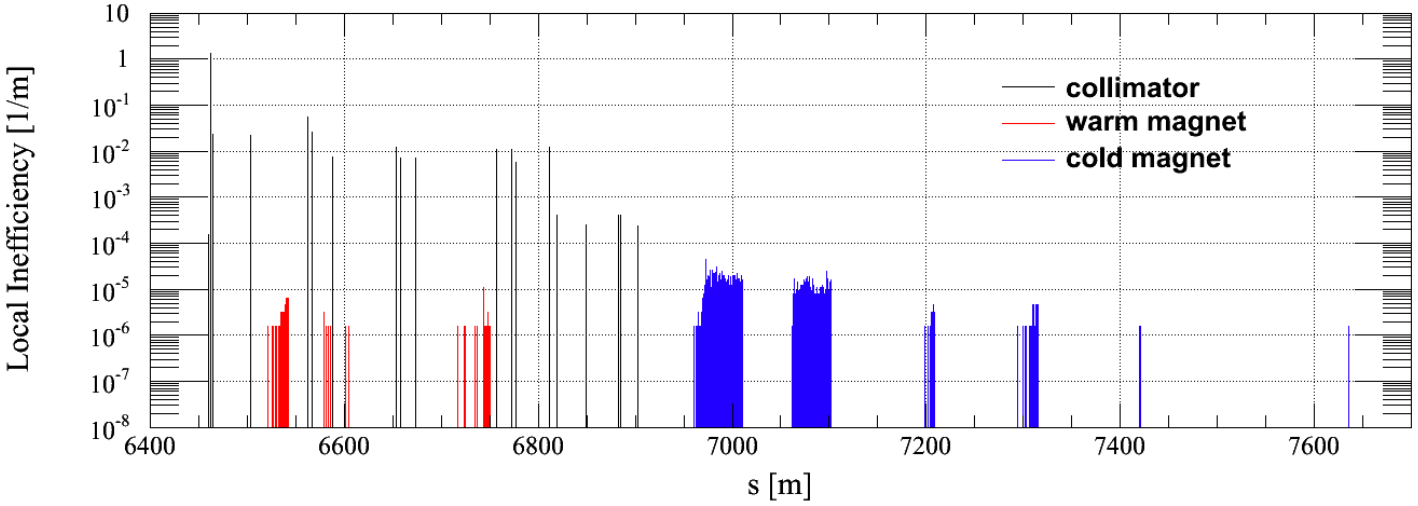

(b) Betatron cleaning insertion IR7

Figure 7.6. Simulated beam loss map at 7 TeV with the new routine for Beam 2 horizontal halo case.

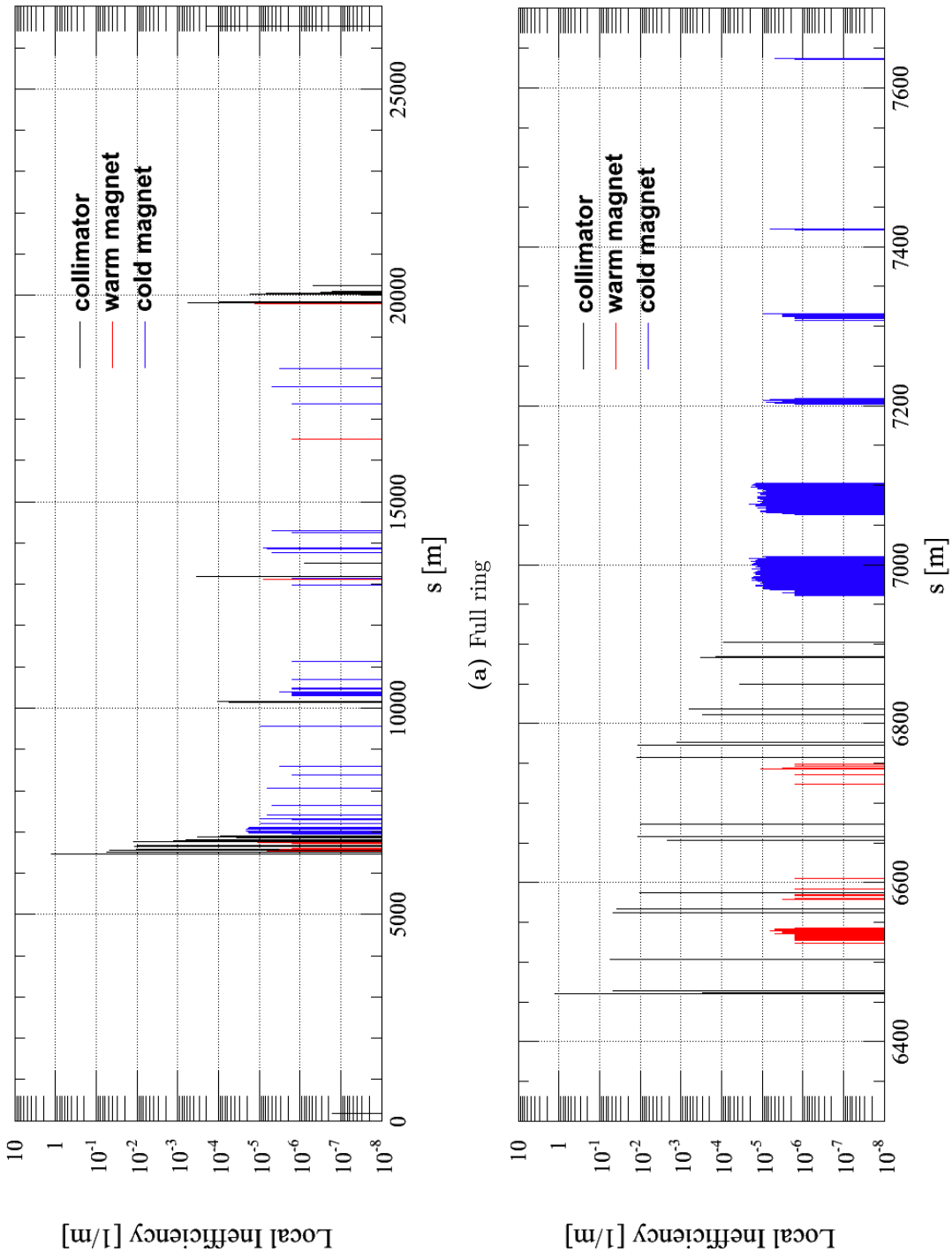

(a) Full ring

(b) Betatron cleaning insertion IR7

Figure 7.7. Simulated beam loss map at 7 TeV with the new routine for Beam 2 vertical halo case.

7.3 Impacts at the primary collimators

Primary collimators are installed in the momentum cleaning insertion (IR3) and in the betatron cleaning insertion (IR7). In IR3 the primary collimators are set with a half-gap of $15\,\sigma$ while in the IR7 they are set with a half-gap of $6\,\sigma$.
In the multi-stage collimation system the TCPs intercept the primary halo, generated in this case at $6\,\sigma$ from the center of the beam orbit. Fig.7.8 shows the simulated impacts at primary collimators in IR7 with the new scattering routine, for Beam 1 with a horizontal halo distribution, while Fig.7.9 shows the case of Beam 1 with a vertical halo distribution. The transverse distribution is presented with the projections in x and y directions normalized to the collimator σ. The number of particles lost at the collimator are normalized to the collimator length and to the total number of particles absorbed at collimators. In Fig.7.10 and Fig.7.11 are shown the simulated impacts at the primary collimators in IR7 for Beam 2 with a horizontal and a vertical halo distribution respectively.

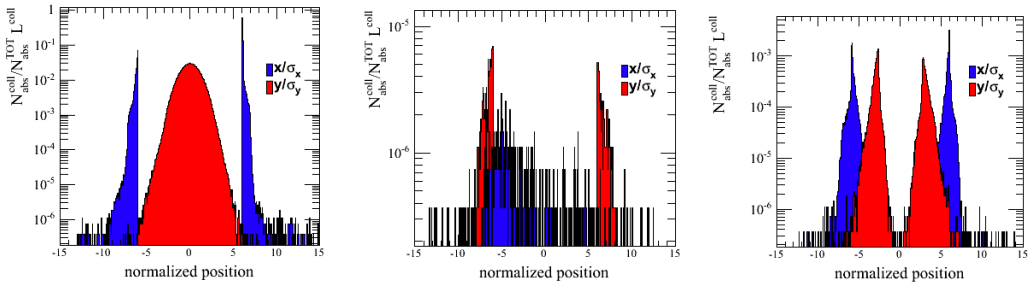

(a) Horizontal TCP **(b)** Vertical TCP **(c)** Skew TCP

Figure 7.8. Transverse distribution projections of the impacts on the primary collimators, Beam 1 horizontal halo.

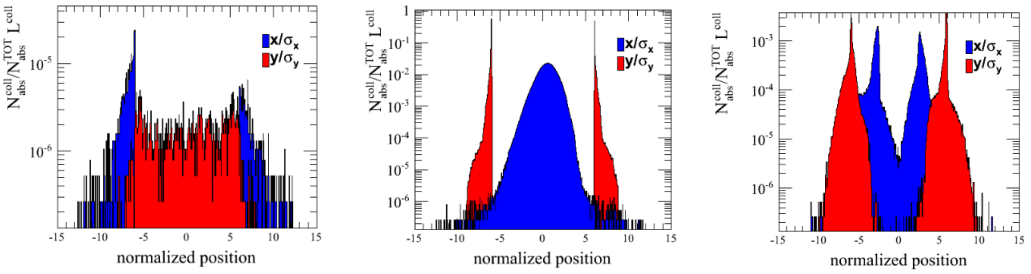

(a) Horizontal TCP **(b)** Vertical TCP **(c)** Skew TCP

Figure 7.9. Transverse distribution projections of the impacts on the primary collimators, Beam 1 vertical halo.

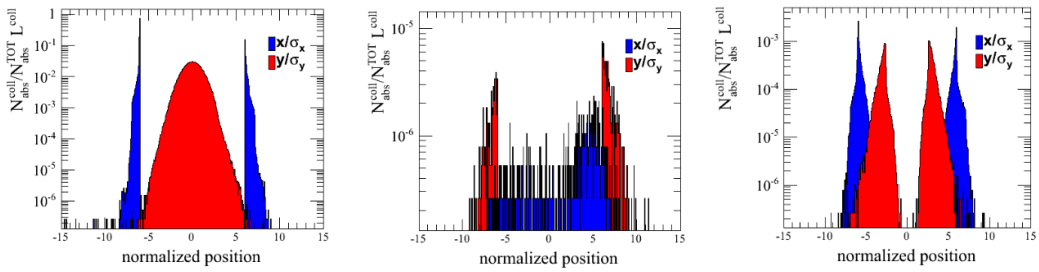

(a) Horizontal TCP **(b)** Vertical TCP **(c)** Skew TCP

Figure 7.10. Transverse distribution projections of the impacts on the primary collimators, Beam 2 horizontal halo.

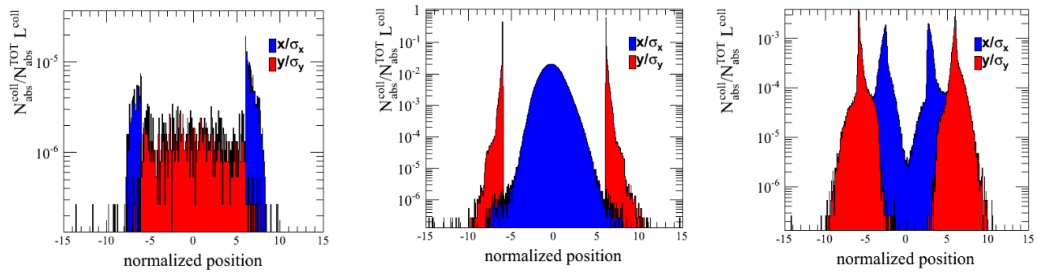

(a) Horizontal TCP **(b)** Vertical TCP **(c)** Skew TCP

Figure 7.11. Transverse distribution projections of the impacts on the primary collimators, Beam 2 vertical halo.

7.4 Losses at Dispersion Suppressor region at IR7

The dispersion suppressor (DS) region is a transition between the LHC arcs and the insertions which aims to reduce the machine dispersion inside the insertions. The dispersion suppressor regions are located at the end of each LHC arc and the tunnel geometry determines their lengths. The critical locations for the LHC collimation system are the dispersion suppressors of cleaning insertions where dispersive losses reach their maximum.

The IR7 insertion contains the betatron cleaning system where the particles with large betratron amplitude in both vertical and horizontal directions are scattered by the primary collimator jaws and absorbed by the secondary collimators. The dispersion suppressor region in IR7 extends from Q8 to Q11 magnets, the protons with a transverse amplitude large enough to impact on the vacuum chamber leave the insertion and are lost on the machine apertures depositing energy on the machine equipments.

Fig.7.12 shows the transverse distribution of the simulated impacts by using the new routine in the ranges r_1=20270-20350 m (top) and r_2=20370-20450 m (bottom) of the the dispersion suppressor. The impacts are shown together with the projections in the x and y directions. The total number of particle lost in the cold magnets normalized by the total number of particles simulated is shown in Fig.7.13 for Beam 1 horizontal halo case. The red line represents the simulations coming from the

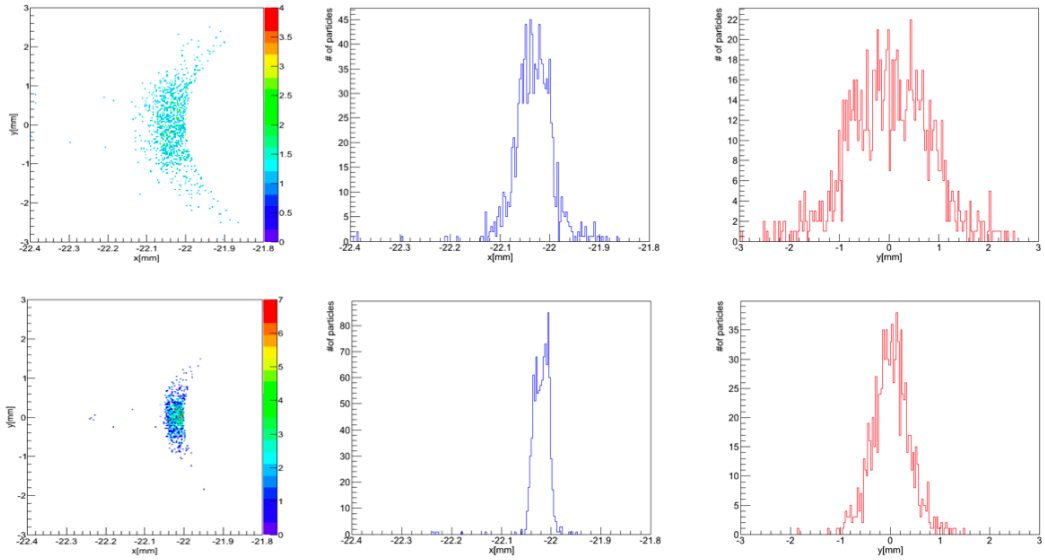

Figure 7.12. Transverse distribution of the particle lost in the dispersion suppressor in IR7 for Beam 1 with horizontal halo distribution.

updated routine while the black line are the simulations of the previous SixTrack version . The total number of particle lost in the cold magnets has been calculated by integrating the histogram shown in Fig.7.12. With the new SixTrack version the losses increase by about a factor of 2 in the first range r_1 and by a factor of 1.5 in the second range r_2.
A comparison at 7 TeV of the number of particles lost at DS in IR7 between the updated scattering routine and the old one is presented in Table 7.2 - 7.5 for Beam 1 and Beam 2 with horizontal and vertical halo distributions. Table 7.2 - 7.5 show the number of particle lost in each range with the ratio defined as the number of lost particles divided by the total number of particle generated.

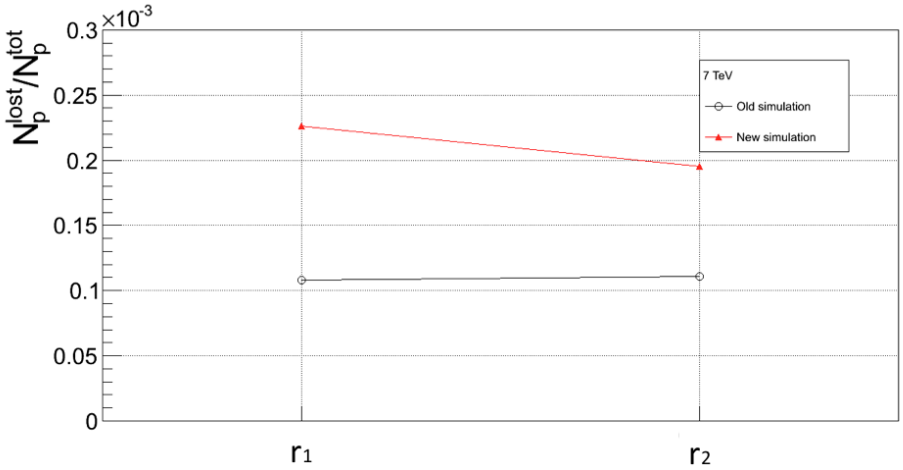

Figure 7.13. Total of particle lost in the DS region at IR7 for Beam 1 horizontal halo case.

Table 7.2. Beam losses and the ratio of the number of lost particles divided by the total number of particle generated in the dispersion suppressor at IR7 Beam 1 horizontal halo case.

	r_1=20270-20350		r_2=20370-20450	
	Ratio	Losses	Ratio	Losses
New Routine	2.26×10^{-4}	1078	1.95×10^{-4}	930
Old Routine	1.08×10^{-4}	596	1.11×10^{-4}	612

Table 7.3. Beam losses and the ratio of the number of lost particles divided by the total number of particle generated in the dispersion suppressor at IR7 Beam 1 vertical halo case.

	r_1=20270-20350		r_2=20370-20450	
	Ratio	Losses	Ratio	Losses
New Routine	2.31×10^{-4}	1477	2.36×10^{-4}	1509
Old Routine	1.34×10^{-4}	857	1.48×10^{-4}	946

Table 7.4. Beam losses and the ratio of the number of lost particles divided by the total number of particle generated in the dispersion suppressor at IR7 Beam 2 horizontal halo case.

	r_1=20270-20350		r_2=20370-20450	
	Ratio	Losses	Ratio	Losses
New Routine	4.22×10^{-4}	2698	2.11×10^{-4}	1349
Old Routine	2.61×10^{-4}	1668	1.38×10^{-4}	882

Table 7.5. Beam losses and the ratio of the number of lost particles divided by the total number of particle generated in the dispersion suppressor at IR7 Beam 2 vertical halo case.

	r_1=20270-20350		r_2=20370-20450	
	Ratio	Losses	Ratio	Losses
New Routine	2.95×10^{-4}	1886	1.95×10^{-4}	1247
Old Routine	1.77×10^{-4}	1131	1.20×10^{-4}	767

With the new routine the losses increase from a factor of 1.5 to a factor of 2 compared to the simulated losses with the old SixTrack version.

7.5 Impacts on TCTs

Collisions at $\sqrt{s} = 14\,\text{TeV}$ require a high efficiency collimator system due to the maximal energy deposition and local aperture restrictions at the experimental triplets. The triplets consist in three quadruple magnets installed to reduce the optical β function at the IPs. In order to protect the triplet magnets local beam cleaning is provided by the tertiary collimators (TCTs). The tertiary collimators intercept and dilute the tertiary halo, avoiding quenches because of the less impacting energy on the superconducting triplet magnets. The number of particles absorbed by the

tertiary collimators are shown in Fig.7.14 for B1 horizontal halo case. The blue line represents the simulation performed with the new version of the scattering routine, while the red line represents the simulations performed with the old one. The number of expected impacts increase by a factor of ∼2 for the new routine with respect to the old one. In both cases, new and old simulations, the number of particles absorbed by the TCTs in IR2 is below 10^{-7}. The increase of particle absorbed is expected from the data comparison since the new version simulations get closer to the experimental data by about a factor of 2 with respect to the old routine. In particular, the behavior for both versions is the same except for the tertiary collimators at IP8. In this case the previous version shows more impacts on the tertiary collimators by a factor of ∼4 with respect to the new one for the horizontal TCT collimator. Moreover no hit affects the vertical tertiary collimator in IP8 in the case of the previous routine while few impacts can be observed with the simulations carried out with the updated SixTrack routine, however the errors in these points are larger due to the lack of statistics.

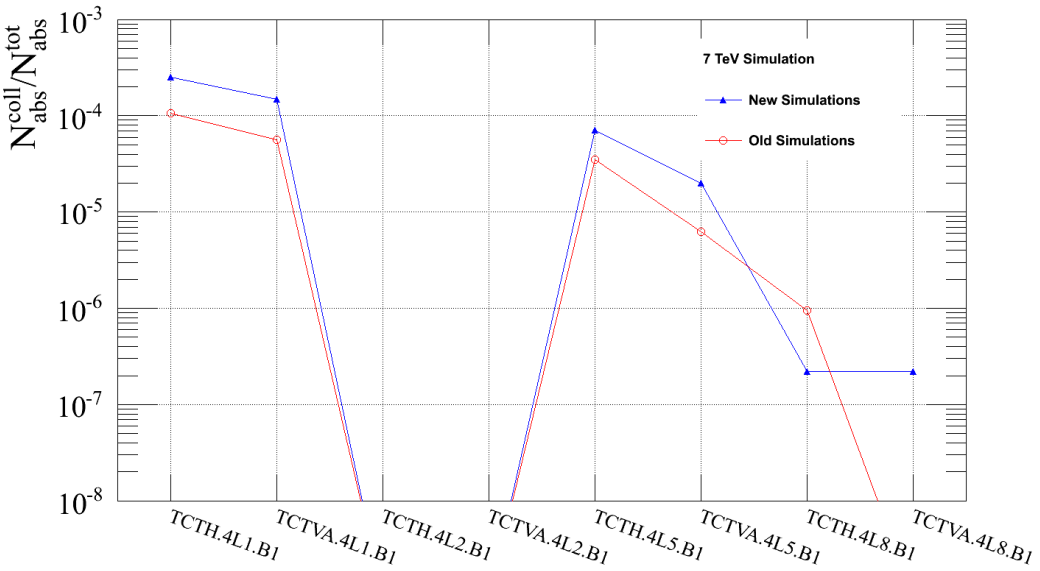

Figure 7.14. Number of particles absorbed in TCT collimators with new scattering routine (blue) and the previous one (red) normalized to the total particles absorbed in the collimation system.

7.6 Parametric study for 7TeV simulations

A parametric study varying the proton-proton single diffractive cross section and the proton-proton elastic cross section values was carried out by using the updated scattering routine for 7 TeV simulations. This study allows to understand how the uncertainty on the cross sections affects the cleaning performance and the impacts on the tertiary collimators. The proton-proton single diffractive cross section was modified by a fixed amount of ±20% and ±50%, the proton-proton elastic cross section was modified by a fixed amount of ±20%. The effects produced on the

cleaning inefficiency by the single diffractive cross section variation are presented in Table 7.6 and in Table 7.7 for Beam 1 horizontal halo case.

Table 7.6. Maximum cleaning inefficiency on the cold magnets in IR7 for ± 20% variation of single diffractive cross section.

	Cleaning Inefficiency$\times 10^{-5}$ [1/m]		
	σ^{SD} -20%	New simulation	σ^{SD} +20 %
Q8	1.151	1.104	1.481
Q9	2.796	3.532	5.595
Q10	0.164	0.221	0.329
Q11	1.480	2.428	3.291

Table 7.7. Maximum cleaning inefficiency on the cold magnets in IR7 for ± 50% variation of single diffractive cross section.

	Cleaning Inefficiency$\times 10^{-5}$ [1/m]		
	σ^{SD} -50%	New simulation	σ^{SD} +50 %
Q8	0.822	1.104	2.200
Q9	1.316	3.532	4.716
Q10	0.164	0.221	0.314
Q11	1.809	2.428	5.659

Table 7.8. Maximum cleaning inefficiency on the cold magnets in IR7 for ± 20% variation of proton-proton elastic cross section.

	Cleaning Inefficiency$\times 10^{-5}$ [1/m]		
	σ^{el} -20%	New simulation	σ^{el} +20%
Q8	1.151	1.104	0.986
Q9	5.589	3.532	3.945
Q10	0.329	0.221	0.329
Q11	4.767	2.428	2.794

In particular, the maximum cleaning inefficiency is given for the cold magnets in IR7: Q8, Q9, Q10 and Q11. In the case of Q8 magnet the variation of -20% does not produce relevant difference with respect to the case without variation,
The maximum variation of the cleaning inefficiency in the case of -20% of the proton-proton single diffractive cross section is about a factor of 0.6 for the Q11 magnet. In the case of +20% of the proton-proton single diffractive cross section the maximum variation of the cleaning inefficiency reaches a factor of 1.6 for the Q9 magnet. The variation of -50% of the single diffractive cross section produces a maximum cleaning inefficiency variation by a factor ~ 0.4 in the case of Q9 magnet, while in the case of a variation of +50% the maximum cleaning inefficiency reaches a factor of 2.3 for the Q11 magnet. Table 7.8 shows the effects on the cleaning inefficiency produced by the proton-proton elastic cross section variation. In this case a maximum cleaning inefficiency variation by a factor of 1.6 is reached in the case of Q9 magnet for a variation of the proton-proton elastic cross section of -20%. The variation of +20%

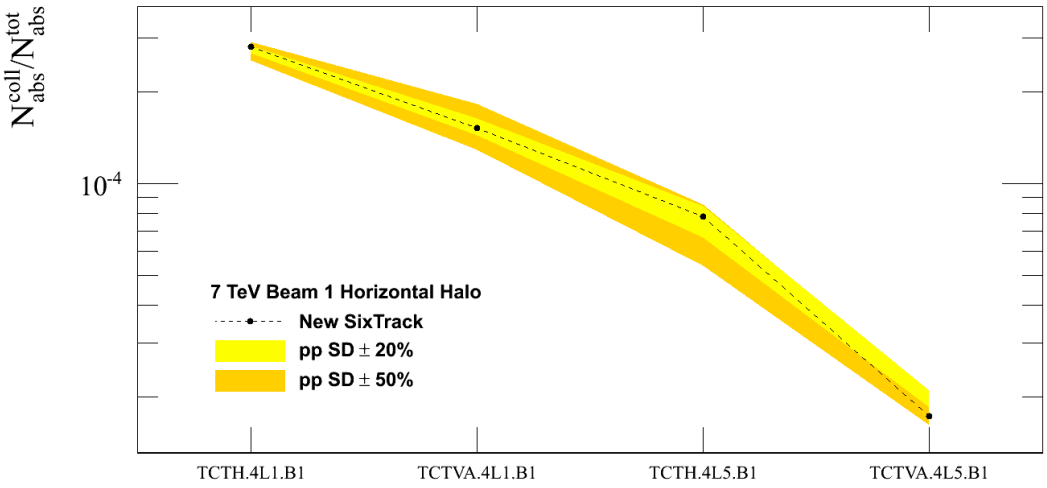

Figure 7.15. Effects on the impacts at TCT collimators in IR1 and IR5 for a $\sigma_{pp}^{SD} \pm 20\%$ variation and a $\sigma_{pp}^{SD} \pm 50\%$ variation, Beam 1 with a horizontal halo distribution.

of the same cross section produces a maximum cleaning inefficiency increase by a factor of ~ 1.5 in the case of Q10 and Q11 magnets.
The effects on the simulated impacts with the new SixTrack version at TCT collimators in IR1 and IR5 are presented in Fig.7.15. The yellow band represents the impacts at the TCTs with a ±20% variation of the single diffractive cross section, the orange band represents the impacts with a ±50% variation of the single diffractive cross section and the black points are the simulated impacts for the case without variation. The impacts are normalized to the total number of particles absorbed by the collimators. For the ±20% variation of the single diffractive cross section, the major impact difference can be appreciated on the tertiary collimators TCTH.4L5 and TCTVA.4L5 at IR5. In particular, for TCTH.4L5 collimator the +20% variation of the single diffractive cross section moves up the impacts level about 8% of relative difference, while the -20% variation results into a decrease about 14% of relative difference with respect to the case without variation. For the TCTVA.4L5 collimator the +20% variation of the single diffractive cross section moves up the impacts about 6% of relative difference with respect to the reference case without variation, while the -20% variation of the single diffractive cross section increases the impacts with a relative difference of $\sim$ 21%. For the ±50% variation of the single diffractive cross section, the major impact difference can be appreciated on the tertiary collimators TCTH.4L5 at IR5 and TCTVA.4L1 at IR1. In the case of the TCTH.4L5 collimator, the +50% variation produces an increase of the impacts with a relative difference about 9%, while the -50% variation results into a decrease about 31% of relative difference with respect to the case without variation. For the TCTVA.4L1 collimator, the +50% variation of the single diffractive cross section moves down the impacts level about 15% of relative difference, while the -50% variation results into an increase about 20% of relative difference with respect to the reference case.
The proton-proton elastic cross section was also varied by ±20%, however no significant changes in the number of impacts at the TCTs was found.

Chapter 8

Conclusions

The LHC machine is designed to accelerate two proton counterrotating beams, up to 7 TeV, that collides in the experimental detectors. Also ions (Pb) can be accelerated up to 574 TeV per nucleus. Due to the high beam intensity the energy deposition of the beam losses around the machine must be always monitored and kept under control. An energy deposition of about 5 mJ s^{-1} cm^{-3} is indeed enough to quench the LHC superconducting magnets cooled to a temperature between 1.8 K and 4.5 K. To prevent dangerous beam losses an efficient collimation system is of crucial importance. The collimator system provides beam cleaning, guarantees a smooth and safe operation of the machine and reduces the background for the experiments. Collimation studies aim to limit the number of particles that escape from the collimator insertions and keep under control the beam losses. The collimation studies are carried out also by means of simulations using the SixTrack software. This is a complex program able to track a large number of halo particles element-by-element using transfer matrices to describe the effect of each lattice element. The interaction of the protons with the collimator jaws is implemented in a dedicated scattering routine based on a Monte Carlo method. The scattering routine simulates the nuclear and the electromagnetic processes between protons and the collimator material nuclei. The scattering routine originates from the K2 code developed during the 1990's and afterwards integrated in the SixTrack source code. An update of this routine by using new recent experimental data was necessary to better describe the interaction processes at higher energy. In order to introduce effective modifications able to provide a better approximation of the experimental data a deep investigation on the physics model underlying the scattering routine has been carried out. As result of this study several changes have been considered and then implemented in the scattering routine regarding both the electromagnetic and nuclear processes:

- A different Carbon density that better fits the real collimator jaw material has been included in the routine.
- The logarithmic term in the in the rms angle equation of the multiple Coulomb scattering has been added. In the old scattering routine this term was missing. This logarithmic correction gave a larger spread of the protons outside of the collimator.
- To better estimate the ionization losses the Bethe-Bloch equation has been

implemented in the routine. In the previous routine version the energy loss by ionization was described by a constant term for any given energy.

- To better extrapolate the proton-proton elastic and total cross sections new fits were computed and included on the basis of recent measurements from the TOTEM collaboration.
- The proton-proton single diffractive cross section has been updated considering a recent parametrization based on the renormalized pomeron flux exchange.
- The proton-nucleus inelastic and total cross sections have been updated considering the new available data from the Particle Data Group.

The overall effect is an increase of the impacts downstream the collimator system. This trend is mainly due to the increase of the single diffractive cross section with respect to the previous parametrization. The validation of the updates made was presented in the Chapter 6, where the result of the comparison with data at 3.5 TeV is presented. The simulations performed with the updated version of the scattering routine show, as general trend, an outcome closer to the experimental data by a factor $\sim$3, for Beam 1 horizontal halo case and by a factor $\sim$2 for Beam 1 vertical halo case, with respect to the previous routine version simulations. On the basis of the presented comparisons with the previous routine version, validated by a clear reduction of the spread with experimental data, it is possible to state that the modifications applied to the scattering routine resulted into a significative improvement in the simulation of the nuclear and the electromagnetic processes between protons and the collimator jaw material.
The LHC design energy of 7 TeV for each beam has been not achieved yet, the maximum level achieved was reached in March 2013 with 4 TeV energy beams. Because of the quench limit decrease at higher energy, the requirements for the collimation system performance will be more demanding than to the ones addressed in previous run. Therefore, the prediction of the cleaning inefficiency at higher energies is under investigation. In Chapter 7 the simulations results at 7 TeV are presented, these simulations were performed with the improved scattering routine. The expected number of particles lost on the tertiary collimators, that protect the triplet magnets in the collision points, increases by a factor 2 with respect to the previous simulations results. Furthermore, the increase factor of the predicted leakage at the cold magnets in the Dispersion suppression in IR7 varies between a factor of 1.5 and a factor of 2.
At 7 TeV, the proton-proton single diffractive cross section was varied by $\pm$20% and $\pm$50% in order to determine the uncertainty on the cleaning inefficiency. This study indicates that the cleaning inefficiency in the Dispersion Suppressor region can vary in a range from 0.6 to a factor of 1.6 for a change of $\pm$20% of the single diffractive cross section, and in a range from 0.4 to a factor of 2.3 for a $\pm$50% variation of this cross section.
As a follow up of this work, further simulations using the new scattering routine will be performed in order to provide:

- a quantitative comparison between 3.5 TeV experimental data and imperfect machine simulations. The imperfect machine case applied to the old routine

simulations increases the simulated losses at the tertiary collimators in IP1 and IP5 by a factor of ∼5 (see Fig.6.13 from [46]). Similarly, a further agreement is expected between the losses predicted with the new routine and the experimental data;

- future comparisons between simulations and 7 TeV experimental data when the design beam energy will be reached to confirm the new routine simulation results at this energy level.

In order to provide a more detailed picture of the ionization losses at higher energy:

- the tail contribution of the ionization energy loss distribution may also be considered in the scattering routine;
- the radiation losses for high energy protons can be included in the calculation of the Bethe-Bloch equation.

Those research paths can result in further improvements in the scattering routine simulation capability.

Bibliography

[1] M. Martini. An introduction to transverse beam dynamics in accelerators. *CERN/PS 96-11*, 1996.

[2] H. Wiedermann. *Particle Accelerator Physics*. Springer, 3rd edition, 2007.

[3] K. Wille. *The Physics of Particle Accelerators, an introduction*. OXFORD University Press, first edition, 1996.

[4] G. Robert-Demolaize. *Design and Performance Optimization of the LHC Collimation System*. PhD thesis, Universite Joseph Fourier, Grenoble, 2006.

[5] C. Bracco. *Commissioning Scenarios and Tests for the LHC Collimation system Resistive transition and protection of LHC superconducting cables and magnets*. PhD thesis, EPFL Lausanne, 2008.

[6] A. Piwinski. The touschek effect in strong focussing rings. *DESY 98-179*, 1998.

[7] M. Sands. The physics of electron storage rings. *SLAC report 121*, 1970.

[8] `http://lhc-collimation-project.web.cern.ch/`.

[9] M.Tigner A.Wu Chao. *Accelerator physics and engineering*. World Scientific Publishing, 1st edition, 1999.

[10] Cern - the large hadron collider. `http://home.web.cern.ch/about/accelerators/large-hadron-collider`.

[11] M. Benedikt, P. Collier, V. Mertens, J. Poole, and K. Schindl (editors). LHC design report v.3 : The LHC injector chain. *CERN-2004-003-V3*, 2004.

[12] `https://espace.cern.ch/liu-project/LIU_images/Forms/DispForm.aspx?ID=11`.

[13] O. S. Brüning, P. Collier, P. Lebrun, S. Myers, R. Ostojic, J. Poole, and P. Proudlock (editors). LHC design report v.1 : The LHC main ring. *CERN-2004-003-V1*, 2004.

[14] ATLAS Collaboration. The ATLAS experiment at the CERN Large Hadron Collider. *JINST*, (3):S08003, 2008.

[15] CMS Collaboration. The CMS experiment at the CERN LHC. *JINST*, (3):S08004, 2008.

[16] LHCb technical proposal. *CERN/LHCC 98-4, LHCC/P4*, 1998.

[17] ALICE Collaboration: F. Carminati, P Foka, P Giubellino, A Morsch, G Paic, J-P Revol, K Safarik, Y Schutz, and U. A. Wiedemann (editors). Alice: Physics performance report, volume i. *Journal of Physics G: Nuclear and Particle Physics*, 30(11):1517–1763, 2004.

[18] `http://cerncourier.com/cws/article/cern/54384`.

[19] F. Schmidt. SixTrack. User's Reference Manual. *CERN/SL/94-56-AP*, 1994.

[20] G. Robert-Demolaize, R. Assmann, S. Redaelli, and F. Schmidt. A new version of sixtrack with collimation and aperture interface. *Proc. of the Particle Accelerator Conf. 2005, Knoxville*, page 4084, 2005.

[21] T. Trenkler and J.B. Jeanneret. K2, a software package evaluating collimation systems in circular colliders (manual). *CERN SL/94105 (AP)*, 1994.

[22] `http://mad.web.cern.ch/mad/`.

[23] S. Redaelli, R. Assmann, and G. Robert-Demolaize. Lhc aperture and commissioning of the collimation system. *Proceedings of the LHC Project Workshop Chamonix XIV*, 2005.

[24] A. Fasso et al. *CERN-2005-10*, 2005.

[25] A. Fasso and others. The physics models of FLUKA: status and recent developments. *Proc. of the Computing in High Energy and Nuclear Physics 2003 Conf., La Jolla*, 2003.

[26] G. Battistoni, S. Muraro, P. R. Sala, F. Cerutti, A. Ferrari, S. Roesler, A. Fasso, and J. Ranft. The fluka code: Description and benchmarking. *Hadronic Shower Simulation Workshop 2006, Fermilab 6–8 September 2006, AIP Conference Proceeding*, 896:31–49, 2007.

[27] Passage of particles through matter. The Review of Particle Physics: 2005 Reviews Tables and Plots, Particle Data Group web page "`http://www.test.org/doe/`".

[28] P.G.Rancoita C.Leroy. *Radiation interaction in matter and detection.* World Scietific, 2004.

[29] W.R.Leo. *Techniques for nuclear and particle physics experiments.* Springer-Verlag, 2nd edition, 1994.

[30] H.A.Bethe. Moliere's theory of multiple scattering. *Phys. Rev.*, 89(6):1256, Mar 1953.

[31] N.Catalan Lasheras. *Collimacion transversal y longitudinal de un haz the protones de alta energia an el Gran Colisionador de Hadrones (LHC).* PhD thesis, Universidad de Zaragoza, 1998.

[32] K.Greisen B.Rossi. Cosmic-ray theory. *Review of Modern Physics*, 13(4):240.

[33] G.bellettini et al. Proton-nuclei cross sections at 20 gev. *Nuclear Physics*, 79(3):609–624, May 1966.

[34] G. Antchev et al. Luminosity-independent measurement of the proton-proton total cross section at $\sqrt{s} = 8$ Tev. *Physical Review Letter*, 111(1):9, Jul 2013.

[35] The TOTEM Collaboration et al. Measurement of proton-proton elastic scattering and total cross-section at $\sqrt{s} = 7$Tev. *Europhysics Letters*, 101(2):21002, Jan 2013.

[36] K. Goulianos. *Diffractive interactions of hadrons at high energies.* Physics Reports vol. 101, pp. 171-219, 1983.

[37] D. Bernard and the UA4 Collaboration. *Physics Letters B*, 186:227, 1987.

[38] D.Bernard and the UA4 Collaboration. Measurament of small angle antiproton-proton elastic scattering at $\sqrt{s}$=546 and 1800 gev. *Physics Review D*, 50:5518, 1994.

[39] N.A. Amos, others, and E710 Collaboration. *Physics Letters B*, 301:313, 1993.

[40] K.Goulianos. Renormalization of hadronic diffraction and the structure of the pomeron. *Physics Letters B*, 358:379–388, 1995.

[41] A. Schiz et al. Hadron-nucleus elastic scattering at 70, 125 and 175 gev/c. *Physical Review D*, 21(11):3010–3022, 1980.

[42] Particle data group-atomic nuclear properties. `http://pdg.lbl.gov/2013/AtomicNuclearProperties/index.html`.

[43] W.Höfle, R.Assmann, S.Redaelli, R.Schmidt, D.Valuch, D.Wollmann, and M.Zerlauth. Controlled transverse blow-up of high- energy proton beams for aperture measurements and loss maps. *CERN-ATS*, 128.

[44] W.Höfle, F. Dubouchet, G. Kotzian, and D. Valuch. Performance of the lhc transverse damper with bunch trains. *CERN-ACC*, 0216.

[45] B. Salvachua et al. Cleaning performance of the lhc collimation system up to 4Tev. *CERN-ACC-2013-0070*, 2013.

[46] R.Bruce et al. Simulations and measurements of cleaning with 100 MJ beams in the LHC. *CERN-ACC-2013-0113*, 2013.

[47] E. Skordis and R. Bruce. FLUKA simulations of BLM response. *LHC Collimation working group (6/5/2013).*